Fundamental Studies of the Sterile Filtration of Large Plasmid DNA

A thesis submitted to

University College London

for the degree of

Doctor of Philosophy

by

Affaro Affandy

Department of Biochemical Engineering

University College London

Torrington Place

London WC1E 7JE

Declaration

"I, Affaro Affandy, confirm that the work presented in this thesis is my own. Where information has been derived from other sources, I confirm that this has been indicated in the thesis."

Signed 29th January 2013

Abstract

Sterile filtration is considered as a final step in processing pharmaceutical grade plasmid DNA. During the development of filtration process, fundamental understanding on the mechanism of fouling and the DNA degradation is critical to improve filtration performance. This study focuses on the fouling and degradation of large plasmid DNA (> 20 kb) in sterilising grade filters.

Scanning electron microscopy (SEM) was applied to investigate the mechanism of fouling of pGEc47 plasmid DNA (56 kb) in sterile filter. The investigation contributes to the fundamental understanding of the behaviour of large plasmid molecules during filtration through 0.22 µm membrane. The SEM images suggested that the fouling was due to entrapment of plasmids on the surface of membrane that created meshes of plasmids DNA. The severe form of the superposition of DNA meshes blocked the entrance of pores and restricted the passage of other incoming plasmid molecules. The observations of cross sections of the membrane showed that after filtration with 200 µg of plasmid, the blockage of internal pores was detected. Quantitative analysis of the progression of fouling using digital image processing technique suggested that the transition of fouling occurred. During filtration of 50 µg plasmid, the blockage was due to superposition of DNA molecules. However, after filtration of 200 µg plasmid, complete blockage of the pores was observed.

In order to understand the blockage of membrane by plasmid DNA, the mechanism of fouling of pQR150 (20 kb) and pGEc47 (56 kb) plasmids during constant pressure filtration inside 0.22 µm PVDF membrane is experimentally investigated. The decline of filtrate flux as function of time is analysed using the framework of classical and combined blocking models (Bolton et al., 2006). The results for both plasmids indicate a transition between fouling mechanisms. Initially, during early part of the filtration, the intermediate blocking model provided the best fit of the experimental results suggesting that fouling of the membrane was mainly caused by deposition of particles onto its surface. Afterwards, the result trends were best captured by the standard blocking model indicating that internal fouling of membrane was the dominant fouling mechanism. A study of the transmission (C_f/C_0) of both plasmids shows a significant reduction of plasmid transmission which coincides with the transition of the fouling mechanism from

intermediate to standard blocking. The study elucidates the applicability of filtration blocking model to explain the fouling behaviour of large plasmid DNA during sterile filtration.

The loss of plasmid is also related to the degradation of supercoiled (SC) plasmid to other topologies such as open circular and linear DNA. The degradation is correlated to fluid stresses in bioprocessing equipments that may contribute to the breakage of the phosphodiester bond between bases in the double-helical structure of DNA. The computational fluid dynamics (CFD) simulation was carried out to estimate the magnitude of elongational strain rate inside 0.22 µm polyvinylidene fluoride (PVDF) membrane which is a critical for plasmid DNA degradation. The results were compared with the critical elongational strain rate for DNA breakage and the experimental data that correlates with the loss of 20 kb plasmid DNA. Two approaches have been developed to determine the strain rates inside the membrane, which are the macro- and micro-scale models. During the filtration of plasmid at 5 and 8 psi transmembrane pressures, the macro-scale model estimated the average elongational strain rates up to $1x10^{3}$ s^{-1}. Furthermore, the micro-scale model detected wide range of local elongational strain rates up to $1x10^{5}$ s^{-1}. However, local elongational strain rates below ~$4x10^{3}$ s^{-1} were detected in most of regions of the membrane, which is below the critical elongational strain rate for DNA breakage.

Acknowledgement

I sincerely thank to my academic supervisor, *Prof. Eli Keshavarz-Moore*, for her support and guidance throughout my PhD work. It was a real pleasure to be under her supervision, which I have learned a lot on how to be a good scientist. I am grateful to my academic advisor *Henk K. Versteeg*, for his help and advice and in particular, for his expert opinion on fluid flow and computational fluid dynamics (CFD). I always admire his passion and his attention to detail.

I would like to offer my special thanks to *Dr. Spyros Gerontas, Dr. Darren Nesbeth, Dr. Simyee Kong, Dr. Arjun Dhanoya, Dr. Balasundaram Bangaru, Dr. Andrea Rayat and Amanatuzzakiah Halim* for sharing this valuable experience with me.

I am truly indebted and thankful to the Ministry of Higher Education Malaysia and International Islamic University Malaysia for financial support throughout my studies in UCL.

I owe a massive debt of gratitude to my parents for their love and support and finally to *Beby* and *Ainan*, for always being there for me. Their love and support is my strength and comfort.

Contents

List of figures

List of tables

Nomenclature

ΔP_{actual}	Transmembrane pressure during the actual experiment
ΔP_{HP}	Transmembrane pressure calculated using the Hagen-Poiseuille equation
ΔP	Transmembrane pressure
μ	Dynamic viscosity
A	Available membrane frontal area
a	Persistence length
A_0	Initial membrane frontal area
B	Constant of the standard blocking model
C	Constant of the cake filtration model
c	DNA concentration
D	Diffusion coefficient
d	Diameter of a pore
F_{max}	Maximum hydrodynamic force to break the polymer chain
F_ϑ	Initial angle factor
J	Filtrate flux
J_v	Volumetric flow rate
K	Temperature
k	Membrane permeability
K_A	The blocked membrane surface area per unit total volume of permeate
K_b	Complete blocking fitting parameter
K_{BM}	The decreased of pore's cross sectional area per unit total filtrate volume
K_B	Boltzmann constant
K_c	Cake filtration fitting parameter
K_{CM}	Area of the cake per unit permeate volume
K_i	Intermediate blocking fitting parameter
K_{ic}	Intermediate blocking fitting parameter in combined model
K_s	Standard blocking fitting parameter
L	Contour length
n	Filtration constant
n_p	Number of pores per unit area

η	Intrinsic viscosity
Q	Volumetric flow rate
R	Membrane resistance
R_0	Resistance of a clean membrane
R_c	Hydraulic resistance of cake
R_g	Radius of gyration
r_h	Hydrodynamic radius
R_r	Resistance of the cake filtration model
S	Safety factor
t	Time
u	Fluid velocity
u_0	Initial flux
V	Filtrate volume
V_0	Initial volumetric flow rate
V_{max}	Maximum volumetric capacity of membrane per unit area
V_{pore}	Average velocity inside a pore
y	Shear strain rate
y_w	Wall shear strain rate
α	Filtration law constant
β	Filtration law constant
ε	Elongational strain rate
ε_{max}	Maximum elongational strain rate
ρ	Density
τ	Tortuosity factor
Φ	Membrane porosity

1 Introduction

1.1 Overview and motivation of the project

Rapid development and current progress in gene therapy and DNA vaccination increase demand and interest for plasmid DNA. This thesis discusses the sterile filtration step which typically constitutes the last stage of the production of therapeutic grade DNA. While there is general consensus that the study of the finishing step in processing of this material is of paramount importance, there is relatively little systematic work done in the area. A particular concern is the issue relating to the fouling of the membrane that leads to product loss and the possibility of the degradation of supercoiled plasmid DNA due to fluid stresses.

Fundamental understanding of the interactions between filtration feed and membrane is critical for characterisation and development of a filtration process. One of the significant factors that determine filtration performance is the fouling of the membrane, which is considered as a major drawback in the application of membrane filtration in downstream processing. Fouling is blockage or retention of impurities or product of interest onto the surface or inside the membrane that affects the quality and transmission of the desirable product. This phenomenon entails the decline of filtrate flux, the increase of transmembrane pressure and the decrease of the capability of the membrane to retain impurities. In this thesis, fouling was observed and analysed quantitatively using various microscopy techniques. However, as microscopy techniques are unable to supply real time information of the fouling process besides being labour intensive and time consuming in term of sample preparation. Membrane blocking models were applied to complement direct visualisation techniques to predict the performance and to characterise the filtration process.

Classical membrane blocking models are regularly applied to investigate the fouling mechanism and to predict the capacity of the membrane for filter scale-up. However, the method has limitations since it assumes that the filter acts as series of cylinders which contrasts with the microporous polymeric membrane used in this work. Additionally, the classical blocking models

describe that the fouling occurs in a single mechanism with the foulant constricted, layered on the surface, completely blocking the pore or generating a cake layer on the surface of the membrane. However, the assumed phenomena are not observed during the filtration of proteins, where a combination and transition of fouling mechanisms was observed (Bolton et al., 2006, Ho and Zydney, 2000, Duclos-Orsello et al., 2006a). DNA has a unique physical nature compared with other particulates since it is a flexible chain-like molecule. This allows DNA to penetrate pores and elongate during its trajectory inside the membrane (Latulippe et al., 2008). This contrasts with the assumption of the blocking models that the feed contains rigid sphere-like particles. This thesis investigates the applicability of blocking models to explain fouling during filtration of large plasmids DNA.

As the transmission and breakage of plasmid DNA molecules is relates to the fluid flow regimes (Kong et al., 2006), computational fluid dynamics (CFD) was applied to characterise the flow inside the membrane. The characterisation of the velocity magnitude and strain rates were done through macroscopic and microscopic approaches which describe fluid flows in a simple control volume and actual membrane respectively.

The investigation of fouling and characterisation of fluid flows provides better understanding of the fundamental issues of plasmid DNA filtration and allows us to make informed decision for scaling-up of the filtration process.

1.1.1 ***Aims of the thesis***

- To characterise the fouling mechanism using direct visualisation technique
- To test the applicability of membrane blocking models to describe fouling of large plasmid DNA
- To investigate the transition of fouling mechanisms using filtration laws
- To analyse the correlation between plasmid transmission and the trend of fouling
- To develop methods for characterisation of fluid flow regimes inside sterile filtration membrane using computational fluid dynamics (CFD). As fluid stresses are critical for the breakage of the plasmid chain, the magnitude of this parameter is determined using CFD. The simulation data was then compared with the experimental and literature data relating to plasmid loss.

1.2 **Plasmid DNA as a raw material for DNA vaccination and gene therapy**

1.2.1 ***Plasmid as vector in gene therapy and DNA vaccination***

A plasmid is a covalently closed double stranded and extra-chromosomal DNA that is increasingly attractive as a non-viral gene delivery system. As the viral vector employs a disabled virus, the non viral vector utilises complexion of plasmid based genes with agents such as lipids or polypeptides. Plasmids have been an interesting alternative to viral delivery systems as it does not integrate into the genome and trigger unnecessary immunological response. The plasmid is then transiently expressed protein-encoded antigen in transfected cells. The process mimics the intracellular pathogenic response that triggers humoral and cellular immune responses.

Plasmid DNA exists in various topologies such as compact supercoiled (SC), nicked open circular (OC), linear and genomic DNA (Figure 1.1.) These topologies can be determined by gel electrophoresis where SC plasmid migrates faster than linear and OC DNA due to its tight conformation.

The supercoiled plasmid DNA degrades to open circular or linear form when it experience mechanical or enzymatic degradation (Schleef and Schmidt, 2004). The open circular plasmid is a form when one strand of the double stranded DNA is broken or nicked and the linear plasmid DNA where both strands of the DNA are cleaved at approximately the same positions (Figure 1.1). The degraded forms of DNA affect the efficiency of plasmids as a vector due to missing of the gene coding regions or promoters (Schleef and Schmidt, 2004). During the transfection of plasmid into a cell, the plasmid DNA must retain the covalently closed circular or supercoiled isoform to maintain maximum biological activity (Levy et al., 1999b).

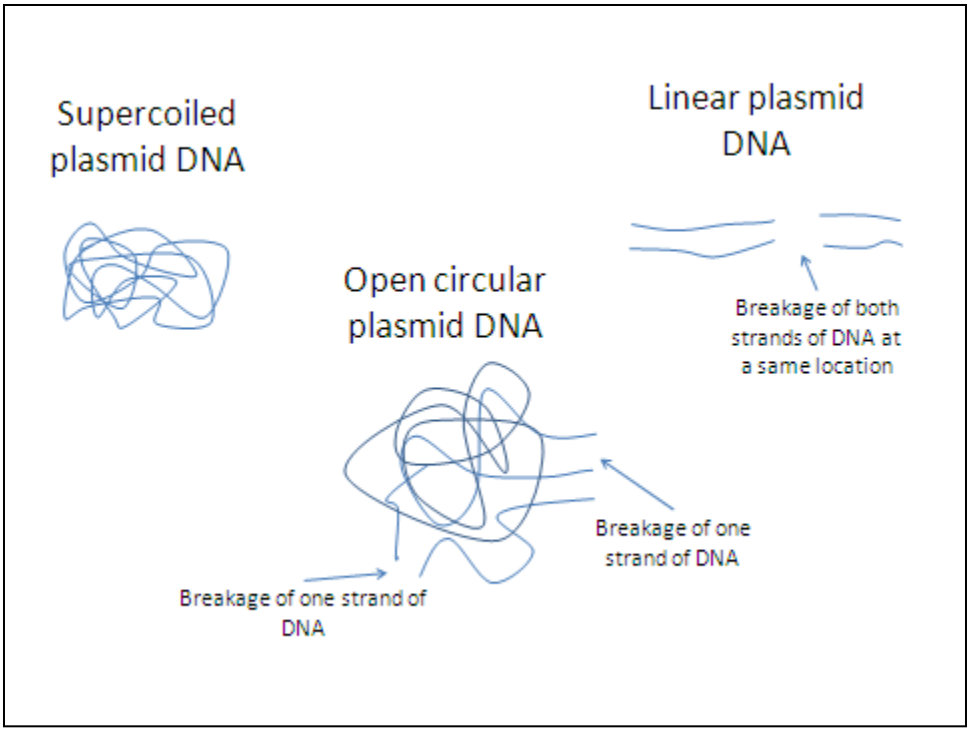

Figure 1.1- Schematic representation of plasmid DNA topologies.

1.2.2 ***Impact of fluid stress on plasmids***

De Gennes (1974) provides a theoretical explanation that the molecular coil extension of a polymer is due to elongational flow. The flow causes hydrodynamic friction across the molecule. The degree and magnitude of the friction cause deformation, unravelling and breakage of the polymer (De Gennes, 1974). Experimentally, the breakage of linear double stranded DNA in defined shear and normal stress fields has been reported (Davison, 1959, Levinthal and Davison, 1961, Adam and Zimm, 1977) .

The breakage of the plasmid DNA backbone is due to scission of the phosphodiester bond of phosphate-deoxyribose backbone (Figure 1.2).

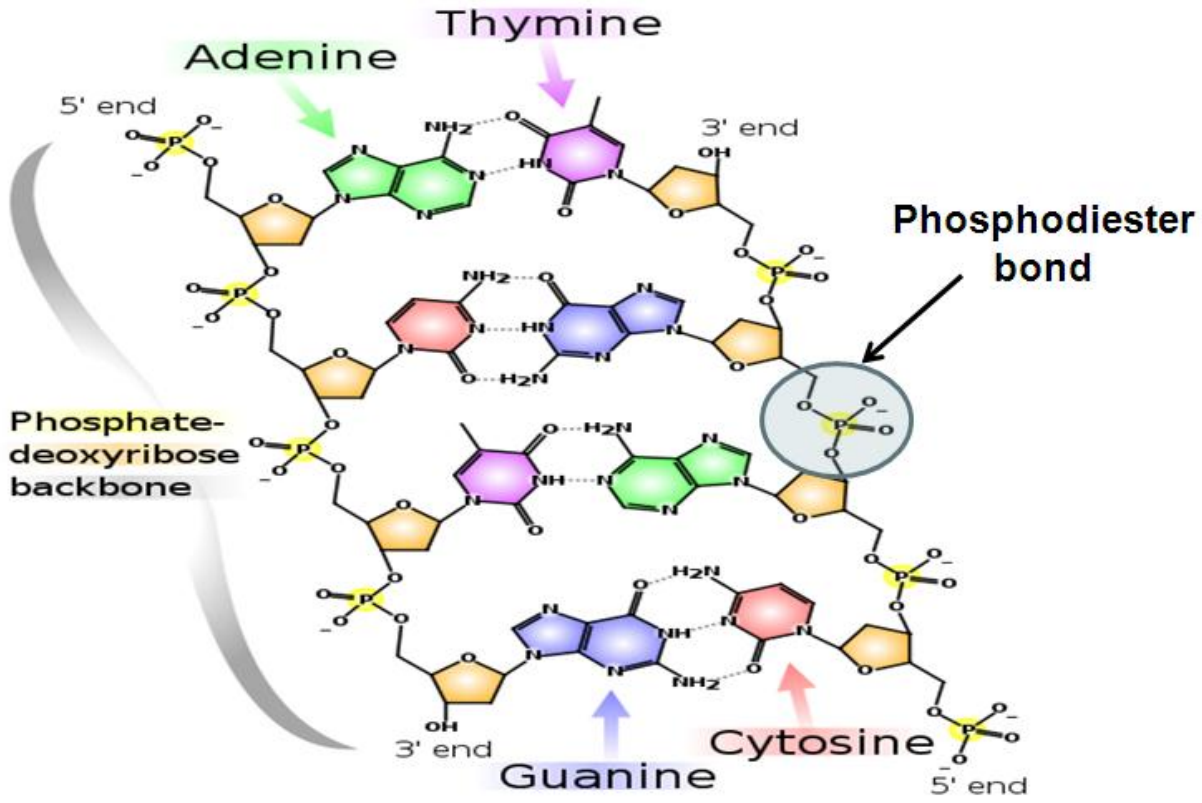

Figure 1.2- Schematic diagram of the structure of DNA molecule. The breakage of DNA molecule is due to scission of the phosphodiester bond caused by hydrodynamic friction.

The effect of fluid stresses on the breakage of SC plasmid in downstream processing equipments has been investigated by application of scale down approaches using capillary rheometer and rotating (Levy et al., 1999b) and capillary shear devices (Meacle et al., 2007). Breakage of plasmid DNA was also observed during sterilising filtration of plasmid DNA (Kong et al., 2006). This work suggested that the decrease of SC plasmid integrity is linearly correlated with the size of the plasmid.

However, the characterisation of the magnitude of strain rates in a complex polymeric membrane is still not well understood. The theoretical calculation of strain rates applies the Hagen-Poiseuille equation that assumes the membrane as arrays of cylinders. This assumption contrasts with the actual architecture of a complex membrane. This study attempts to develop methods to characterise the strain rates inside sterile filtration membranes using computational fluid dynamics (CFD).

1.2.3 ***The production of pharmaceutical grade plasmid DNA***

Several unit operations are involved in the production of pharmaceutical grade plasmid. Detailed discussions on the production of plasmid DNA can be found in Prather et al (2003), Levy et al (2000), Prazeres and Ferreira (2004), Shamlou (2003) and Carnes and Williams (2007).

The downstream processing of plasmid DNA can be categorized into three main components: primary recovery, intermediate recovery and final purification. In each category, the challenges are to separate the plasmid from host impurities and the SC DNA from other plasmid topologies such as open circular and linear (Prazeres and Ferreira, 2004). Figure 1.3 summarises the typical large scale plasmid purification steps.

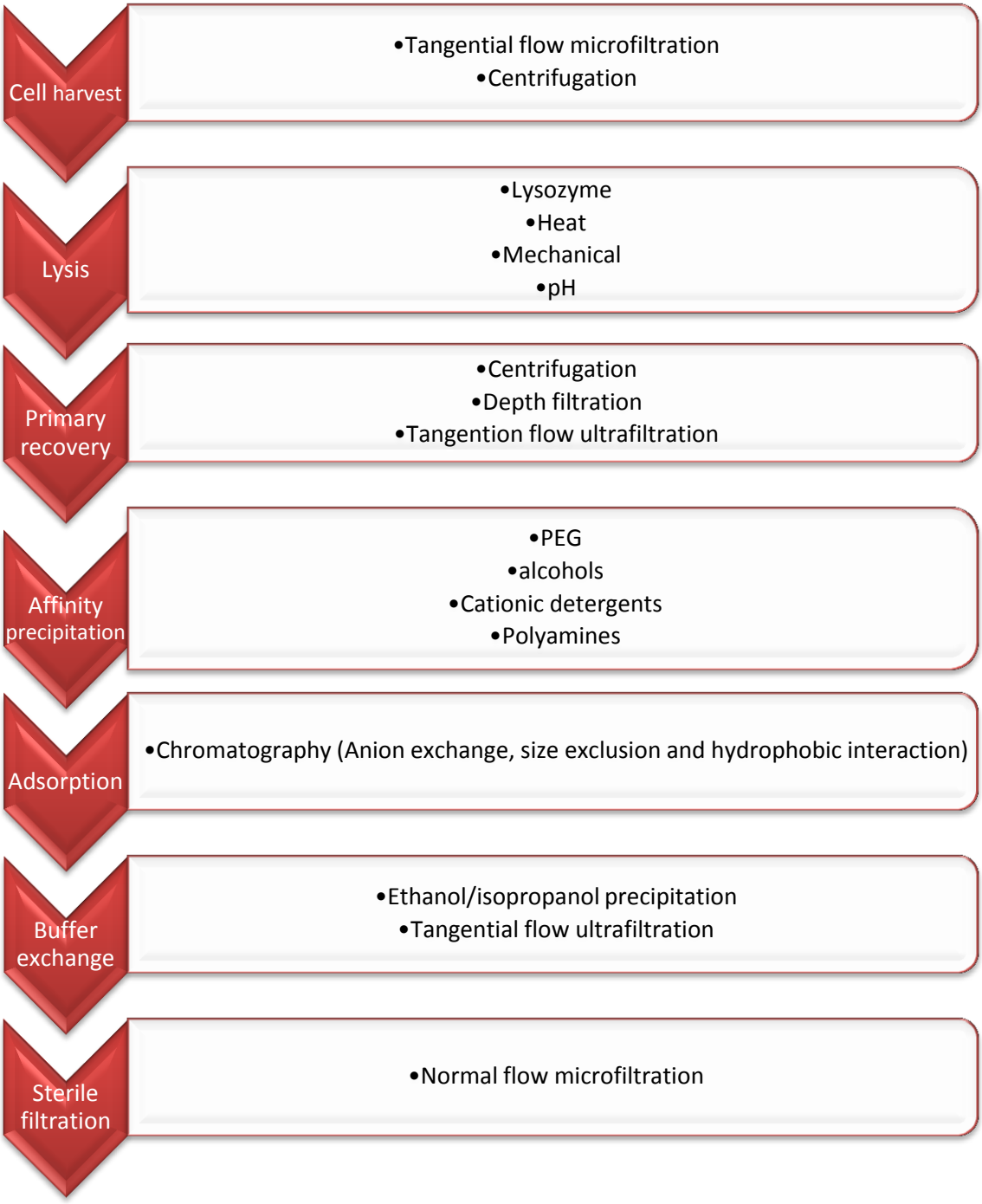

Figure 1.3- Typical downstream processes of pharmaceutical grade plasmid. (Adapted from Prather et al, 2003)

1.2.4 ***Issues and challenges in the production of pharmaceutical grade DNA***

The production of plasmid DNA for DNA vaccination and gene therapy is under compliance of Good Manufacturing Practices (cGMP) required by the Food and Drug Administration (USFDA) and European Medicines Agency (EMEA). It is crucial that during the manufacturing of plasmid DNA, the consistency is achieved in terms of purity, potency, efficacy, identity and safety (Prazeres and Ferreira, 2004). To meet these requirements, it is important for biochemical engineers to understand the fundamental problems in each unit operations. Table 1.1 shows the scale up issues relating to the processing of pharmaceutical grade plasmid.

Table 1.1- Challenges and issues during the large scale purification of pharmaceutical grade plasmid. (Adapted from Prather et al, 2003)

Purification steps	**Challenges/issues**
Tangential flow microfiltration	Fouling, membrane surface area
Centrifugation	Cleaning of equipment
Lysis- pH	Vessel design Mixing strategy Degradation of SC
Depth filtration	Filter aid disposal Flocculation Fouling
Tangential flow filtration	Fouling
PEG	Flocculation
Chromatography	Column design and high costs
Ethanol/isopropanol precipitation	Explosion hazard
Sterile filtration	Membrane area and fouling

This thesis will address issues regarding the final purification stage which is the sterile filtration step. As stated in Table 1.1, fouling and determination of membrane area for pilot and industrial scales manufacturing are the critical factors. Watson et al (2006) discussed these two parameters for 6 kb plasmid (Watson et al., 2006). However, the trend of fouling and the estimation of required membrane area for larger plasmids are still little understood.

1.2.5 ***Opportunities in bioprocessing of pharmaceutical grade DNA***

A recent study by Kong et al (2006) has shown that plasmid filtration through 0.22 μm filter resulted in losses of up to 80% for a 116 kb naked DNA, the loss being linearly correlated with the DNA molecular size (Kong et al., 2006). Formulation with a range of complexes, i.e. complexation of plasmids with polyethylenimine (PEI) and lipid-integrin binding peptide (LI), did not all improve transmission. However, the use of a filter with asymmetrical pores improved transmission and decreased DNA damage. This was speculated to be the result of less significant elongational effects in this type of filter. Therefore, it is a need to elucidate the mechanism of flow in sterile filters with a view to improving the recovery of plasmid. In this thesis, computational fluid dynamics is employed to investigate the fluid flow regime inside a sterile filtration membrane.

Currently, small plasmids (less than 20kb) have been employed in clinical trials. However, the potential of large plasmid DNA with size over 20 kb needs to be considered in the future (Levy et al, 2000). Some diseases also need larger plasmids (15 to 20 kb) to encode specific genes for the treatment. For example, in treating cystic fibrosis, there is a need for large plasmids with functional cystic fibrosis transmembrane-conductance regulator (CFTR) (Lee et al, 2005). Multi-gene vectors for extensive control regions may also require larger plasmids. Demand for large plasmids is expected to be high due to effort of incorporating specific gene carrying plasmids with signalling molecules (e.g. cytokines) (Prather et al, 2003). In this manuscript, the behaviour of fouling and degradation of considerably large plasmid DNA will be investigated.

1.2.6 ***The future of DNA-based therapeutics***

Three DNA vaccines and one gene therapy product have been licensed for veterinary use. Table 1.2 shows the commercially available DNA vaccines:

Table 1.2- Licensed DNA based products for veterinary use. Adapted from Liu (2011).

Name	**Company**	**Indication**	**Species**
Apex-IHN®	Novartis Animal Health	Infectious haematopoietic necrosis virus	Salmon
West Nile-Innovator®	Fort Dodge Animal Health, USA	West Nile virus	Horses
Oncept™	Merial	Melanoma	Dogs
LifeTide®SW5	VGX Animal Health Inc	Increase litter survival	Breeding sows

The safety of the application of DNA vaccines in both preclinical and clinical studies has been demonstrated in numerous works (Liu, 2011). The major issues in the development of DNA vaccines are the immunologic response and delivery of plasmid into the host cells. Due to low magnitude of response as a result of poor delivery of plasmid into the host cell, various strategies have been developed such as novel delivery techniques (i.e. electroporation), better formulation (i.e. Vaxfectin™, application of microparticle) and prime-boost strategies.

The use of naked DNA has successfully induced immune response in small animals, but it is less efficient in larger animals and humans. However, the successful commercialisation of licensed DNA vaccine products for animals provides insight that might be useful in promising application of this type of therapy for human use. Additionally, several clinical trials have shown potent immunological results. The results suggest the potential application of this technology in the near future (Liu, 2011).

1.3 **Sterile filtration of pharmaceutical grade plasmid DNA**

1.3.1 ***Filtration as an unit operation***

Filtration is applied at various stages during downstream processing of pharmaceutical products. It is applied in primary recovery to clarify the crude fermentation broth, in product concentration, in buffer exchange and in sterile filtration. In early development of pharmaceutical membranes, the application was limited to analytical scale processes. Current developments show new membranes, modules and systems have been developed to the meet demand of the biotechnology industries (Van Reis and Zydney, 2001).

Filtration is preferable as a separation technology because of the simplicity of the equipment and operation, the equipment is easy to clean and waste is conveniently disposable. It is readily scaled up at any stage of process development (Laska et al., 2005). Membrane separation processes also offer advantages in bioprocessing since they are highly selective operation, do not involve phase change, operate at ambient temperature and are economical and simple to integrate with unit operations of downstream processes (Bowen and Jenner, 1995).

In bioprocessing of pharmaceutical products, filtration is generally operated in three modes: 1) depth filtration, 2) normal/dead-end filtration and 3) tangential/cross-flow filtration. Depth filters trap particles as they pass through fibers or fibrous materials of the filter. The entrapment of particles is mainly due to the tortuous path between the fibers. Depth filters are typically applied as prefilters during downstream processing as they can handle high particle load. They are also applied to protect subsequent downstream elements from clogging and fouling. In normal flow/dead-end filtration, the applied pressure drives the feed stream normal to the surface of the membrane. As the filtration progresses, particles that are larger than the pore accumulate on the upstream surface of the membrane as it gradually fouls the filter. In contrast, tangential flow/cross flow filtration operates as the feed stream passes tangentially along the surface of membrane. The particles that are too large to pass the membrane are swept along by the tangential flow and particles smaller than the pores permeate through the membrane.

During the processing of pharmaceutical products, the greatest interest has been in three types of filtration, namely microfiltration, ultrafiltration and virus filtration. Microfiltration and ultrafiltration are the most widely used in purification of proteins and plasmids. Ultrafiltration membranes are employed to provide high retention of protein and other macromolecules (Van

Reis and Zydney, 2001). Besides its application for separating the molecule of interest from other impurities, this type of membrane has been used for fractionation (concentration) and buffer exchange. Ultrafiltration membranes have pore sizes ranging from 1-20 nm.

In contrast, a microfiltration membrane allows the molecule of interest (proteins and DNA) and other small solutes to pass through the filter while retaining cell and cell debris. Microfiltration is applied to separate particles ranging from 500 nm to 10 µm. Virus filtration has pore size ranging from 20-70 nm.

Fouling is the classic problem and major drawback of normal flow microfiltration. Since the sterilizing filtration of plasmid DNA is operated in this mode, this thesis studies the fouling behaviour of plasmid DNA in this type of filter.

1.3.2 ***Current trends and development of bioprocess membranes***

Filtration is used as an alternative to the conventional separation methods and has been applied extensively as an integral part of bioprocessing. In primary recovery of pharmaceutical products from yeast, bacteria and mammalian cells, cross flow microfiltration competes with centrifugation and expanded bed chromatography. Besides, depth filtration is applied during the clarification step to reduce bio-burden on the subsequent unit operations. Current trend inclines to the application of ultrafiltration membrane for protein concentration and buffer exchange replacing size exclusion chromatography (Van Reis and Zydney, 2001).

Effort is also devoted to the development of new membrane modules to improve mass-transfer and reduce fouling of microfiltration membranes. Rotating systems such as rotating disk filters, cylindrical Taylor vortex devices and helical coiled Dean vortex are integrated with membranes to provide better solution to reduce fouling. These devices improve protein transmission and increase the capacity of the membrane. In normal flow filtration, the application of composite filters is considered to increase particle removal whilst at the same time maintaining high throughput. This type of filter contains different layers of membranes with different size of pores and surface chemistry in which the unwanted particles are removed by combination of sieving, depth filtration and adsorption.

Since fouling is the major disadvantage of a filtration process, new materials for membrane filtration have been developed to improve chemical stability during cleaning and reduce the

adsorption of product of interest to the membrane. Polymers such as polysulfone, polyethersulfone and regenerated cellulose are applied due to low adsorption of protein and inherent thermal and chemical stability.

1.3.3 ***Sterilizing filtration of DNA***

Due to thermal instability of biotherapeutics (including DNA), sterile filtration is preferable to other sterilizing methods such as autoclaving and irradiation.

Sterile filtration is a process of removing microorganisms (excluding viruses) from fluid streams. The end result of this process should be a fluid that free of microorganisms without compromising product quality. A 'sterilizing grade filter' (normally 0.22 µm-rated) is a filter that effectively retains *Pseudomonas diminuta* (ATTC culture no. 19146). Size measurement using optical and scanning electron microscopy has confirmed that *P. diminuta* has a diameter of 0.3-0.4 µm and a length of 0.6-1.0 µm. Bacterial challenge testing is used to classify a filter as a sterilizing grade if the filtrate contains minimum 10^7 cells of this bacteria per cm^2 of effective filtration area. This test not only serves for grading a sterilizing grade filter but it is also required for validation of sterile filtration processes.

1.3.4 ***Development and optimization of filtration process***

Reports have shown that many FDA approved pharmaceuticals will be due for patent expiry starting from the year 2010. About $ 170 billion value of annual sales of blockbuster drugs will enter patent expiry by 2015. This puts pressure on bioprocess engineers to accelerate the development of new product candidates for clinical trials. The development of suitable purification processes will play an important part in the bringing of new active compounds to market. Specifically the development of filtration processes includes selection of appropriate membrane materials, optimising the operational conditions and improvement of scaling up strategy.

The critical factor to consider is the product compatibility with the membrane material, i.e. whether the product of interest binds to the membrane. Watson et al (2006) showed that types of membrane influenced its volumetric capacity. For example, polyvinylidene fluoride (PVDF), polysulfone (PS) and polyethersulfone (PES) resulted in increased membrane's volumetric capacity for filtration of plasmid DNA compared with polytetrafluoroethylene (PTFE), cellulose

ester (CE) and nylon (Watson et al., 2006). The compatibility of membrane materials may due to the chemical and electrostatic interactions and also the hydrophobicity of the membrane.

Interestingly, Watson and co-workers (2006) also found that the construction of membrane influenced the membrane capacity. Similar membrane material from different filter manufacturers yielded different membrane capacity. Membranes manufactured by different vendors have different filter attributes such as pore size distributions and tortuosity which impact the capacity of the membrane.

A method to identify optimum conditions of filtration is required. This can be achieved through the measurement of the capacity of the filter to process the feed. The filter capacity is expressed by *Vmax*; the maximum volume of liquid that can be filtered per unit area of membrane based on a set of operational conditions, feed and filter media (Laska et al., 2005). Conversely, the implementation of *Vmax* allows prediction and estimation of filter area requirement.

1.3.5 ***Scale-down techniques to predict the filtration performance***

Laboratory data that is collected using small filter units has been used as basis for designing filtration processes of pilot and manufacturing scale filtration (Laska et al., 2005). For example, the design and optimization of sterilization of pharmaceutical products using large filter area of a filter cartridge can be determined using 47-mm laboratory disc filter. The application of scale-down techniques is advantageous for the development of biological products since it minimises the cost of development and reduces the usage of manpower and time (Titchener-Hooker et al., 2008).

During early development of pharmaceutical products, active pharmaceutical ingredients (API), such as protein, peptide or plasmid DNA, are produced in very small quantity. Since the product still in the development process, it is usually very expensive to produce. Furthermore, investigation of critical parameters for optimization requires significant quantities of material. Thus it is critical for a scientist or process engineer to obtain tools that can accurately predict the required membrane area at pilot and manufacturing scale. It is important that the information of the required larger scale filter area can be deducted based on information from small scale laboratory data.

In this thesis, the behaviour of plasmid DNA through 13-mm diameter sterilizing grade membranes is investigated in term of its fouling mechanism and its sensitivity to the strain rate. The trends of a plasmid's transmission and degradation can be used as a platform to understand important engineering and biological parameters such as the effect of strain rates and fouling on filtration scale up.

1.4 **Direct visualization methods of membrane fouling**

1.4.1 ***Overview and current development in imaging techniques of membranes***

Microscopy techniques have been applied to investigate the structure of membranes and to analyse the morphology of fouling. Transmission (TEM) and scanning electron microscopy (SEM) are popular tools used by researchers to investigate morphological parameters such as porosity, mean pore radius and pore size distribution. Zeman and Denault, (1992) used SEM coupled with computerized quantitative image analysis to characterise microfiltration membrane (Zeman and Denault, 1992). The authors provide details of basic procedures and image processing techniques to investigate the morphology of membranes. Ziel et al. (2008), provide quantitative analyses of surface and cross sectional area of microfiltration membranes using SEM and TEM by means of computer image analysis. The authors used parameters such as 'porous area fraction' and 'mean free path length' to create porosity profile from the TEM images (Ziel et al., 2008).

Atomic force microscopy (AFM) has also been used to characterise the fouling and morphology of a wide range of membrane; from microfiltration to reverse osmosis. It gives access to the measurement of pore size, pore density, pore size distribution and surface roughness (Wyart et al., 2008).

Confocal scanning electron microscopy has also gained considerable interest for the characterisation of fouling. The 3D reconstruction of fouled membrane using this technique was applied to obtain information of the deposition and adsorption of proteins as well as membrane morphology (Ferrando et al., 2005). This method is also employed to study virus capture phenomena during virus filtration (Bakhshayeshi et al., 2011). It provides information on location and penetration profile of foulant that can be correlated with the effect of membrane morphology to fouling.

However, the application of microscopy techniques typically required physical and chemical treatments of the membrane. In recent development, the application of nano- and micro-computed tomography (nano- and micro-CT) has gained considerable interest since it does not need an invasive protocol prior to imaging. Most importantly, the nano/micro-CT produces 3D images of samples. These characteristics can be manipulated to provide better characterisation of fouled membranes.

1.5 The blocking models: tools to understand the mechanism of fouling and for filtration scale up

A predictive model is needed to understand the underlying mechanism of fouling and for determination of the required membrane area for filter scale-up. As direct visualisation methods used invasive and non-real time approaches, the results may not represent the actual and step-wise phenomena of fouling. Moreover, as was noted before, the estimation of the required membrane area of larger scale filtration is important since during early drug development, raw material for experimentation is always limited.

The understanding of how plasmid DNA fouls the filter is important for better design of the membrane and filtration operation and also as a basis for choosing the appropriate filter for a specific biological feed.

1.5.1 *The blocking models and filtration laws*

The development of prediction models is important for successful implementation of membrane separation processes in industrial scale pharmaceutical production. A number of predictive models have been developed and were discussed by Bowen and Jenner (1995). Such models are osmotic pressure model, gel-polarisation model, resistance model and membrane blocking model. In this thesis, the application of membrane blocking models to describe fouling of plasmid DNA in sterile filters is discussed.

Before we can apply the blocking models to make prediction of required filter area at manufacturing scale, it is important to make an accurate assessment of the fouling mechanism that dominates the filtration. The robust design of a filtration process is highly dependent on the correct model that is employed to characterise the fouling.

The blocking models are derived from the Darcy's law;

$$Q = \frac{PA}{R\mu} \qquad \text{Equation 1.1}$$

Where P is the transmembrane pressure and μ is the viscosity of the solution.

Four classics blocking models are derived from Equation 1.1. These models are the standard (pore constriction), intermediate, complete and cake filtration models. The representation of the first three of these models is described in Figure 1.4. All above models describe the fouling of membranes as a single mechanism. On the basis of their observations of the filtration of BSA, Ho and Zydney (2000) suggest that fouling mechanisms occurred in a transition process which led these authors to propose the combined blocking mechanisms (Ho and Zydney, 2000).

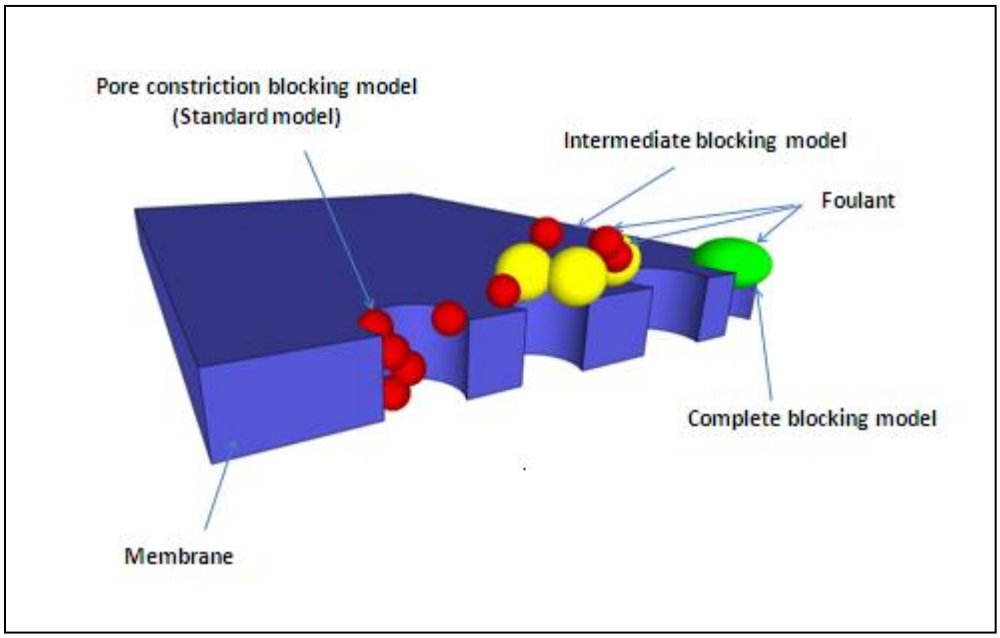

Figure 1.4- The blocking models. The figure describes fouling of membrane due to standard, intermediate and complete blocking models. The cake blocking model is not shown in the figure.

However, some of the underlying assumptions of these models contradict with the actual filtration process. For example, these models treat membrane as array of cylindrical pores, which contrasts with the complex structure of polymeric membrane that consists of tortuous paths through the microfiltration membrane. Also, these models do not account for the asymmetry of the membrane; which is the gradual change of the pore size through the depth of the membrane, that increasingly used in sterile filtration of biotechnology products. These models are macroscopic models, since they ignore the spatial and microscopic details of membrane plugging (Bondy and Santeufemio, 2010). The subsequent chapters will discuss the applicability of these models to the filtration of chain molecule i.e. plasmid DNA through the polymeric microfiltration membrane.

1.5.1.1 Standard blocking model

The standard blocking model (standard model) suggests that the particles are deposited onto the inner wall of the pore thus decreasing the pore volume (Figure 1.4). The time dependency of the volumetric flow rate, *J(t)* is given by an empirical equation:

$$J_V(t) = \frac{V_0}{(1+Bt)^2} \qquad \text{Equation 1.2}$$

Where *B* is the constant of the standard blocking model (s^{-1}) and is given by:

$$B = K_{BM} u_0 \qquad \text{Equation 1.3}$$

K_{BM} is the decreased of pore's cross sectional area per unit of total filtrates volume (m^2/m^3) and u_o is the initial flux (m/s);

$$u_0 = \frac{V_0}{A_0} \qquad \text{Equation 1.4}$$

The predicted time evolution of total filtrate volume is given by;

$$V(t) = \frac{V_0 t}{(1+Bt)} \qquad \text{Equation 1.5}$$

Taking the derivative with respect to the volume of the reciprocal of the derivative of this equation yields the characteristic equation of the standard blocking model:

$$\frac{d^2t}{dV^2} = \frac{2B}{\sqrt{J_0}}\left(\frac{dt}{dV}\right)^{3/2} \qquad \text{Equation 1.6}$$

1.5.1.2 Complete model

The complete model assumes that the entrance of pores is sealed off completely by the particles (Figure 1.4). This assumption leads to an exponential decay of volumetric flow rate which is described by the following time law for the volume flow:

$$J_V(t) = V_0 \exp^{-At} \qquad \text{Equation 1.7}$$

Where A is a constant of complete blocking law (s^{-1}):

$$A = K_A u_0 \qquad \text{Equation 1.8}$$

K_A is the blocked membrane surface area per unit total volume permeated through the membrane (m^{-1}). The predicted time evolution of the total filtrate volume is:

$$V(t) = \frac{V_0}{A}(1 - \exp^{-At}) \qquad \text{Equation 1.9}$$

The characteristic equation of the blocking process is given by:

$$\frac{d^2t}{dV^2} = A\left(\frac{dt}{dV}\right)^2 \qquad \text{Equation 1.10}$$

1.5.1.3 Intermediate blocking model

The intermediate model assumes that the fouling is caused by the combination of complete pore plugging and accumulation of the particles on the top of the deposited particles. The volume flow versus time law is given by;

$$J_V(t) = \frac{V_0}{(1 + At)} \qquad \text{Equation 1.11}$$

The constant *A,* in Equation 1.11 is similar to the constant in the complete blocking model. The time evolution of total permeate volume is:

$$V(t) = \frac{V_0}{A}\ln(1 + At) \qquad \text{Equation 1.12}$$

Taking the reciprocal of the derivatives of equation, the characteristic equation of the intermediate blocking model is:

$$\frac{d^2t}{dV^2} = \frac{A}{V_0}\left(\frac{dt}{dV}\right) \qquad \text{Equation 1.13}$$

1.5.1.4 Cake filtration model

The model assumes that the particles are trapped on the surface of membrane in a permeable cake. The existence of cake increases the resistance to flow. The time law for the volume flow is;

$$J_V(t) = \frac{V_0}{\sqrt{1 + Ct}} \qquad \text{Equation 1.14}$$

C is the constant of the cake filtration law (s^{-1}) and is given by;

$$C = (2R_r)K_{CM}u_0 \qquad \text{Equation 1.15}$$

Where R_r (m^{-1}) is given by:

$$R_r = \frac{R_c}{R_0} \qquad \text{Equation 1.16}$$

R_c (m^{-1}) is the hydraulic resistance of the cake and R_0 (m^{-1}) is the resistance of a clean membrane. K_{CM} (m^{-1}) is the area of the cake per unit permeate volume. The time evolution of total permeate volume is;

$$V(t) = \frac{2V_0}{C}\left(\sqrt{1+Ct} - 1\right)$$ Equation 1.17

Hence, the characteristic equation for the blocking process is given by;

$$\frac{d^2t}{dV^2} = \frac{C}{2V_0{}^2}\left(\frac{dt}{dV}\right)^0$$ Equation 1.18

1.5.1.5 Filtration laws

In all blocking models presented in the preceding paragraph, comparisons between Equation 1.6, Equation 1.10,Equation 1.13 and Equation 1.18 show a common shape for the characteristic equation;

$$\frac{d^2t}{dV^2} = \alpha\left(\frac{dt}{dV}\right)^{\beta}$$ Equation 1.19

Equation 1.19 is called the filtration law and α and β are the constants.

1.5.2 ***Application of blocking models to describe fouling in membranes***

Bowen and Gan (1991) applied blocking models to investigate the fouling of BSA in microporous aluminium oxide, PVDF and polycarbonate membranes. They found that the standard blocking mechanism provides the best fit with the experimental data (Bowen and Gan, 1991). However, Hlavacek and Bouchet (1993) found that the intermediate model fit with the flux decline data of the filtration of BSA through microporous track-etch polycarbonate, cellulose and PVDF membrane (Hlavacek and Bouchet, 1993). In contrast, Tracey and Davis (1994) and Bowen et al (1995) found that the combination of blocking mechanisms is observed during the filtration of BSA through a track-etch microporous membrane (Bowen et al., 1995, Tracey and Davis, 1994). The results suggest that the behaviour of fouling in microporous membrane differs in different filtration operations and types of membrane.

Watson et al (2006) found that the standard model (gradual pore plugging model) was able to describe the fouling mechanism of 6.4 kb plasmid DNA in 0.22 µm PVDF membrane. The small scale data of plasmid filtration was then used to predict the required area for filter scale-up (Watson et al., 2006).

1.5.3 ***Filtration scale-up***

The membrane maximum volumetric capacity can be defined as maximum amount of fluid that can be filtered through a given filter area until the filtrate flux declines to a threshold level of acceptance. The capacity of a membrane is limited by the fouling of the membrane (Belfort et al., 1994). The capacity is also defined as the throughput of a filtration process before the reduction of the quality of filtrate or the process fails to remove specific impurities (Laska et al., 2005). The objective of filtration scale up is to predict the required filtration area of a larger scale filtration on the basis of a mathematical model correctly applied in a small scale filtration set up.

During the development of pharmaceutical grade plasmid DNA, the raw material is normally produced in a small quantity. Additionally, the investigation of critical filtration parameters requires significant quantities of material, which needs considerable amount of upstream processing. Thus it is critical for a scientist or process engineer to obtain tools that can accurately predict the required membrane area at pilot and manufacturing scale from small

scale laboratory data as suggested by the equation below (Laska et al., 2005, Rajniak et al., 2008):

$$A = \frac{V}{V_{\max}} S \qquad \text{Equation 1.20}$$

Where A is the filtration area (m^2); representing large scale filter area requirement, V is the volume of liquid (m^3); representing volume of liquid to be filtered, V_{max} is the maximum volumetric capacity of membrane per unit area (m^3/m^2) and S is the additional safety factor considering variations in performance at large scale. The V_{max} can be derived from the mechanistic filter blocking models (Rajniak et al., 2008). In order to apply the blocking model to predict the required membrane area for filter scale-up, it is important to determine which model describes the fouling mechanism of plasmid DNA in a sterile filter.

1.6 **Computational fluid dynamics (CFD)**

CFD is a tool to carry out numerical simulation experiments. It provides numerical approximation of the equations (a set of partial differential equations, PDE) that govern the flow of fluid. In the bioprocessing context, it is always applied to elucidate the flow field that is not achievable via real laboratory experiments as some fluid flow problems cannot be solved analytically. These flows and the related phenomena can be described numerically through simulation using partial differential/integral differential equations.

1.6.1 ***Application of CFD in bioprocessing***

Currently, CFD has gained considerable interest as one of the tools to characterise the behaviour of fluid flow in processing equipment. It improves the design of bioprocess equipments through better understanding of its physics and fluid flow regime. This helps a rapid and cost effective design of bioprocess equipments.

CFD has been applied in multichamber-bowl centrifuge (Boychyn et al., 2004), high pressure homogenizer (Miller et al., 2002), capillary device (Meacle et al., 2007), normal and cross flow filtration (Kim and Zydney, 2004 and 2006).

1.6.2 ***Theory and methods***

Three main steps; pre-processor, solver and post-processor are typically used for solving a CFD simulation. During the pre-processing step, the input of the flow problem and the computational domains are defined. Such inputs are the boundary conditions and determination of fluid domains. A discretization method is then applied to obtain an approximate solution of the flow. The method approximates partial differential equations (PDEs) and is done through grid generation (meshing); by subdivision of domains to numbers of smaller non-overlapping sub domain-grids of cells.

The solver step applied CFD codes to solve the governing equation of the flow that is subject to the conditions provided. There are many commercial CFD codes available in the market such as Comsol Multiphysics, ANSYS, Fluent, Phoenics and Star-CD. The codes use numerical solutions such as finite difference, finite element, finite volume and spectral methods. The

numerical simulation experiments in this thesis applied the Comsol Multiphysics software which employs the finite element method to solve the PDEs.

The post processing step allows the visualisation and manipulation of the simulation results. These results can be analysed using numerous plotting tools such as surface plots, contour plots, arrow plots, streamline plots and animations.

1.6.2.1 Boundary conditions

Fluid enters and leaves the fluid domain through inlet and outlet boundaries respectively. At the inlet, the pressure or inlet velocity is specified. For an imposed pressure and velocity, it can be described as the velocity vector or pressure normal to the boundary. In this situation, the flow distributions will be extrapolated based on known boundary value of inlet pressure and velocity. At the outlet boundary, a pressure can be imposed.

The no slip boundary conditions eliminates all components of the velocity vector which is described by, u=0. This is an appropriate condition for the wall boundary as the velocities perpendicular and normal to the wall is zero. The no slip condition typically applies to the fluid-solid boundaries of the model geometry.

2 Materials and methods

2.1 Restriction enzyme

The nicking of the supercoiled plasmid DNA was done by hydrolysis of one strand of the duplex at a certain recognition sequence by a nicking endonuclease enzyme. Supercoiled plasmid DNA was nicked to the become open circular isoform by adding 10-20 units of NtBstNBI (New England Biolabs, MA, USA) enzyme (where the enzyme concentration is 10 000 unit / ml) to 1 µg of DNA with NEB (New England Biolabs, MA, USA) buffer 3. The reaction was performed at 4^0C. The mixture was then incubated in a thermocycler at 55^0C for 3 hours. The reaction was stopped by heat deactivation at 80^0C for 20 minutes.

For linearization of SC plasmids, 1 µg of plasmid was mixed with 10-20 units of HindIII (New England Biolabs, MA, USA) and 2µl 10x Buffer R. The reaction was incubated at 37^0C for 3 hours and stopped by heat activation at 80^0C for 20 minutes.

2.2 Plasmids and bacterial cultures

Plasmids pQR150 (Kanamycin resistance, 20 kb) and pGEc47 (Tetracycline resistance, 56 kb) were used in this experiment and grown in *E.coli* DH5α and DH1 respectively. The bacteria were grown on plates containing Nutrient Broth (Oxoids, Basingstoke, Hertfordshire, UK) with appropriate antibiotic. A single colony of bacteria was selected and inoculated to seed cultures of 10, 50, 100 and 500 ml.

Media based on Wubbolts et al (Wubbolts et al., 1996) was used as fermentation medium of *E.coli* DH1.The media contains Na_2HPO_4, 2.8 g/L; K_2HPO_4, 12.1 g/L; KH_2PO_4, 4 g/L; $(NH_4)2SO_4$, 1.2 g/L; NH_4Cl, 0.2 g/L, yeast extract, 5 g/L;L-leusine, 0.6 g/L; L-proline; 0.6 g/L and thiamine 5 mg/L. The pH of the media was adjusted to 6.3 by addition of phosphoric acid and NaOH. The Nutrient Broth was used to grow the *E.coli* DH5α. The cultures were grown at 37^0C for 8 hours with vigorous shaking (200 rpm) for subsequent fermentation.

5 and 10 litres working volume fed-batch fermentations was grown in the BioFlow 310 fermenter (New Brunswick, Cambridge, U.K) and Applikon 20 litres bioreactor (Applikon Biotechnology, Gloucestershire, U.K) with addition of 0.2 % w/v dextran and trace elements (see Appendix 1). The pH of 6.3 ± 0.2 was maintained by automatic pumping of 1 M sodium hydroxide (NaOH) and 1 M phosphoric acid (H_3PO_4). Dissolved Oxygen was maintained at 30% by automatic stirrer speed adjustment. To avoid foaming during fermentation, polypropylene glycol (50% v/v) was added as an antifoaming agent.

The optical density of each fermentation sample was measured at wavelength 660 nm using UV spectrophotometer. The typical optical density of the fermentation can be found in Appendix 2.

2.3 **Purification of plasmid DNA**

E.coli cells were harvested from fermentation media by Beckman J2-M1 centrifuge (Beckman-Coulter, High Wycombe, U.K) for 30 minutes at 4000 rpm. The cell paste was then stored at -20ºC for further use. For purification of plasmid DNA, the cells were dissolved with resuspension buffer (Buffer P1) containing 50 mM Tris-Cl (pH 8), 10 mM EDTA and 100 µg/ml RNase A. The cells were then treated with lysis buffer containing 200 mM NaOH and 1% SDS (Buffer P2) for 2-5 minutes. The mixture was mixed gently to degrade the bacterial cell wall and to avoid degradation of SC plasmid DNA. Neutralizing buffer containing 3.0 M potassium acetate pH 5.0 (Buffer P3) was then added to precipitate proteins and other contaminants. The alkaline lysis buffers P1, P2 and P3 were supplied by Qiagen (Qiagen, West Sussex, U.K). The mixture was centrifuged for 5 minutes at 4000 rpm and subsequently filtered using 47 mm grade 4 (20-25 µm) cellulose filters (Whatman, Kent, U.K). The plasmid was later purified by Hispeed Tip™ anion exchange column chromatography and Qiaprecipitator™ of Qiagen Hispeed plasmids purification kits (Qiagen, West Sussex, U.K). The plasmid was then eluted with 10 mM Tris-EDTA buffer.

2.4 **Agarose gel electrophoresis**

The supercoiled plasmid DNA content after purification was confirmed by agarose gel electrophoresis. 0.6 % agarose gel was pre-stained with 0.5 µg/ml final concentration of ethidium bromide. The gel was run in 1X Tris-Borate EDTA (Sigma Aldrich, Dorset, UK) buffer at 4.5 volts/cm for 4 hours. A supercoiled DNA ladder (Invitrogen, Paisley, U.K.) and a BAC

DNA ladder (Epicentre Biotechnologies, Cambridge, UK) were used to determine the size of plasmids. The image of the DNA bands was acquired and processed with Gel Doc™ EQ gel documentation system and Quantity One™ gel analysis software (BioRad, CA, USA).

The loss and degradation of plasmid DNA were analysed by comparing plasmid content in filtration feed and filtrate using AGE. In order to make comparison between samples of feed and filtrate, the loading of plasmids should be comparatively equal between lanes in term of its mass. One of the common problems of loading the DNA sample is that a portion of the mixture of DNA and gel loading buffer failed to sink into the well. This was handled by mixing the DNA with glycerol. Glycerol is a high density liquid and it helps DNA loads into the well. However, the composition of glycerol-DNA influenced the electrophoretic mobility of the DNA. High concentration of glycerol in the mixture causes the DNA to migrate slower than the mixture that contained a low concentration of glycerol.

2.5 **Spectrophotometry analysis of DNA**

The concentration of DNA was measured using NanoDrop™ 2000 spectrophotometer (Thermo Scientific, DE, U.S). The purity of the DNA after purification was confirmed by analysis of absorbance ratio at 260/280. The 260/280 ratio was used for determination of DNA purity against protein contamination; the standard ratio for plasmid purity is 1.8-2.0.

2.6 **Filtration experiment- Investigation of fouling by scanning electron microscopy**

The 13 mm Durapore® 0.22 µm polyvinylidene fluoride (PVDF) membrane (Millipore, MA, USA) was used in this experiment. The 13 mm Swinny stainless steel filter holder (Millipore, MA, USA) was used as the filter housing during the filtration. The housing was affixed with the Amicon Stirred Cell 8300 (Millipore, M.A., U.S) that connected with the N_2 source. The pressure drop during the filtration was measured using Millipore Integrity Test kits (Millipore, MA, US). The plasmid DNA samples that were used in this experiment were pre-filtered with 0.22 µm membrane before the constant pressure filtration at 1 bar transmembrane pressure.

2.7 Filtration experiment- Investigation of fouling using membrane blocking models

Normal flow filtrations were performed using a syringe filter unit equipped with sterilizing grade 13 mm Millex^{TM}/ Durapore$^{®}$ 0.22 µm polyvinylidene fluoride (PVDF) membrane (Millipore, MA, USA). The filter unit was affixed to an Amicon Stirred Cell 8300 (Millipore, M.A., U.S) connected to N_2 source. The pressure drop during the filtration was measured using Millipore Integrity Test kits (Millipore, MA, US). The plasmid DNA samples used in these experiments were pre-filtered with 0.22 µm membrane before the constant pressure filtration at 5 and 8 psi transmembrane pressures. All the experiments were performed at room temperature. The experimental data was acquired by collecting filtrate volumes in a specific time interval.

The filtrates were collected with collection tubes and an electronic balance was used to measure the filtrate weight. The results shown in each plots in this thesis are the average of two or three sets of data.

2.8 Scanning electron microscopy (SEM) and digital image analysis

The JEOL 7401 high resolution field emission scanning electron microscopy (JEOL, Herts, UK) was used to acquire the cross section and surface of the membrane. Images were then analysed with the digital image processing toolbox that is available in Matlab (MathWorks, U.K).

2.9 Transmission scanning electron microscopy

The JEOL 1010 transmission electron microscope (JEOL, Herts, UK) was used to acquire the cross section of the membrane. Images were then processed with Matlab-Comsol Multiphysics functions for application in CFD simulation.

2.10 Measurement of the thickness of membrane

The depth of the membranes was measured using the Talysurf CLI 200 instrument (Taylor Hobson, Leicester, UK) by employing chromatic length aberration gauges.

2.11 **Particle size distribution analysis**

2.11.1 ***Dynamic light scattering (DLS)***

Dynamic light scattering (DLS) measures the Brownian motion for determination of the size of particles. The Zetasizer Nano (Malvern Instruments, Worcestershire, UK) was used to obtain the hydrodynamic radius, diffusion coefficient and polymer relaxation times of plasmid DNA. The Dispersion Technology Software (DTS) (Malvern Instruments, Worcestershire, UK) nano was used to analyze the results obtained from DLS measurement.

2.11.2 ***Nanoparticle tracking analysis (NTA)***

The NTA works by tracking a group of individual particle that undergo Brownian motion in liquid suspension. The technique uses video to capture a population of nanoparticles and analyse its Brownian motion under illumination of a 80 µm wide laser beam. The rapid movement of these nanoparticles was then tracked by CCD camera in 30-frames per second which enables the system to track the trajectory and movement of the particles. The images taken by the camera are not the actual image of the particle but instead the scattered dimension of the image under the Rayleigh and Abbe limit from which structural and shape information can be derived.

This technique has similarity with the dynamic light scattering where both employ the Stokes-Einstein equation to determine the particle's hydrodynamic size and counts. The diffusion coefficient, *D* is determined by;

$$\frac{(x,y)^2}{4} = Dt$$

The difference is the NTA using video to track the particle's diffusion coefficient whereas DLS using time dependent scattering fluctuations caused by the interference effect of Brownian movement. The NanoSight LM10 (NanoSight, Amesbury, UK) was used to measure the size distribution of plasmid DNA.

2.12 **Non-linear regression analysis**

To analyse the fouling mechanism of plasmids pQR150 (20 kb) and pGEc47 (56 kb), the flux decline data was initially fitted with the classical blocking models (standard, intermediate,

complete and cake filtration blocking models) using the non-linear regression tool of the SigmaPlot statistical and graphing package (Systat Software, London, U.K). The experimental data was subsequently fitted with the combined filtration blocking models developed by Bolton et al. (2006) to determine whether the combination of classical models can provide a better fit with the experimental data. The non-linear regression works by minimizing the sum of square residuals of the data points from the curve of the models.

2.13 **Computational fluid dynamic simulation**

Comsol Multiphysics 4.2 (Comsol Ltd, Hertfordshire, UK) software was employed to solve the fluid flows inside the membrane.

3 Investigation of fouling mechanism of large plasmid DNA in sterile filtration by scanning electron microscopy

3.1 Introduction

The filtration blocking models have been developed based on the assumption that fouling is dominated by the mechanism of pore constriction; complete blocking (pore plugging); intermediate blocking; cake filtration or a combination of these models (Hermia, 1982, Duclos-Orsello et al., 2006b, Ho and Zydney, 2000). However, these conjectural blocking mechanisms can lead to error since the models assume the membrane as an array of cylindrical pores. This assumption is in contrast with complex interconnected pore structure in the symmetric polymeric membrane (Zydney and Ho, 2002). In addition, the models assume that the feed consists of suspended hard spherical particulates, whereas in the present study the molecules of DNA are flexible and of coiled shape structure.

As an alternative approach, the fouling of membranes can be visually identified by microscopy techniques with advanced image processing. Methods such as confocal scanning laser microscopy, scanning and transmission electron microscopy have been commonly employed to obtain fouling profiles of biological materials during filtration (Ferrando et al., 2005, Bakhshayeshi et al., 2011). Confocal scanning electron microscopy was successfully employed to investigate the retention of bovine serum albumin (BSA) and bacteriophages in membranes. The retention of particles was observed to be localized at the entrance of the pores. Investigations using transmission electron microscopy of λ phage DNA showed that the DNA was trapped inside the pores as a hair like structure (Hirasaki et al., 1995).

However, the behaviour of large supercoiled plasmid DNA during filtration is not well described. DNA is observed as a random coil chain conformation in static fluid. During the unraveling of the molecules in flows with high strain rates, the random coil chain conformation tend to

transform to other conformations such as ‘’dumbbell’, ‘half dumbbell’, ‘folded’ and ‘kinked’ (Perkins et al., 1994). These conformational rearrangements are likely to affect the mode of membrane fouling.

The purpose of this chapter was to investigate the progression of membrane fouling using scanning electron microscopy (SEM) and to quantify fouling using digital image processing techniques. Scanning electron microscopy provided a simple, fast and reliable technique to gain insight into the mechanism of fouling. Based on the microscopy image, conceptual models on the mechanism of plasmid retention were developed. The structure of this chapter is summarized in the figure below (Figure 3.1).

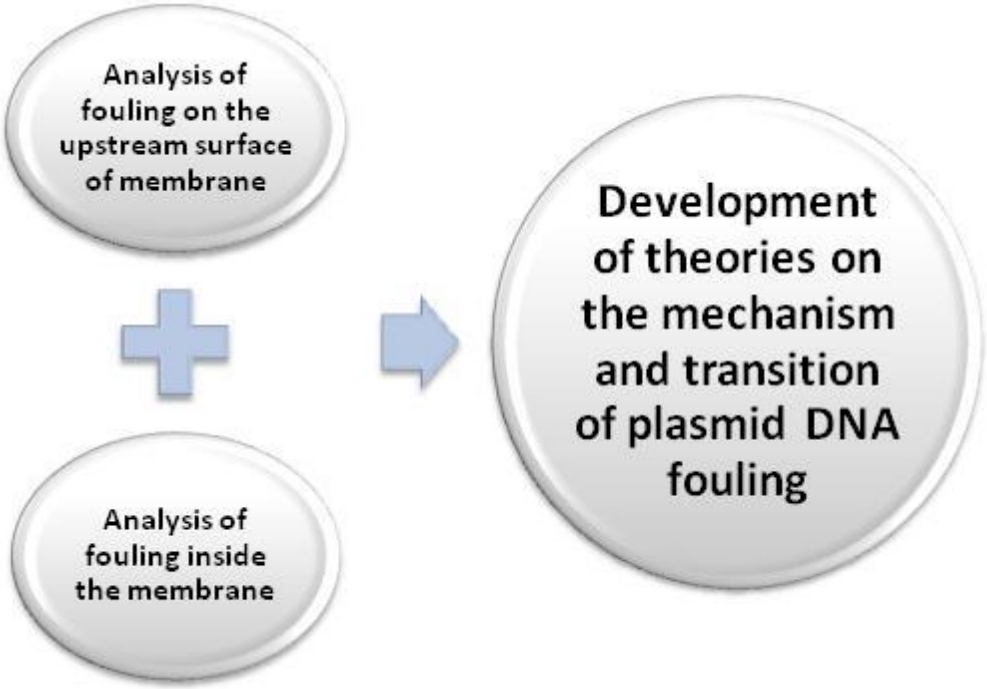

Figure 3.1 - The summary of the workflow for investigation of fouling mechanism of filtration of pGEc47 plasmid using scanning electron microscopy.

3.2 **Experimental approaches**

The plasmid DNA pGEc47 (56 kb) was prepared by fermentation and purification processes as described in the subsections 2.2 and 2.3.

The supercoiled plasmid DNA used in this experiment contained >~ 90 % supercoiled plasmid DNA as confirmed with agarose gel electrophoresis. The purity of plasmid DNA against proteins and organic molecules was confirmed with spectrophotometry analysis. All experiments were conducted using the same concentration of plasmid DNA which is ~ 50 µg/ml.

For the operation of the filtration, please refer to sub chapter 2.6.

After filtration with plasmid DNA, the membrane was immediately frozen with liquid nitrogen for 30 seconds. The sample was then freeze dried for 30 minutes with freeze dryer (ThermoFisher Scientific, Herts, U.K) and treated again with liquid nitrogen in order to freeze fracture the sample. Both the cross section and the surface of specimens were mounted using SEM-specimen holders and sputter coated with ultra-thin layer of gold. The cross section and surface of the membranes were acquired using JEOL 7401 high resolution field emission scanning electron microscopy (JEOL, Herts, UK). The 50º tilting angle was acquired by using the automatic panel in the SEM equipment that controls the plane of the mounted sample.

The images taken from SEM were also used in the quantitative assessment of the effective filtration area and the thickness of the membrane matrix. Each set of measurement was chosen randomly from a selection of images acquired using SEM. In every set of measurement, five images were considered as the templates for quantitative analysis of the progression of fouling.

Images acquired by SEM were analyzed using the digital image processing toolbox that available in Matlab (MathWorks, U.K) to determine the impact of fouling on the blockage of the pores and the reduction in the effective filtration area.

The accumulation of plasmid DNA inside the membrane was assessed by comparing the width of membrane matrix of the intact membrane and the membrane after filtration with 50 and 200 µg plasmid DNA. This accumulation relates to the build-up of the fouling during filtration. The rate of the build-up of fouling may refer to the rate which plasmid and other impurities accumulate around the membrane's matrix.

The width of the membrane matrix was measured using the measurement tool available in Matlab that can measure the distance with a click and drag approach between two endpoints of a line. The distance tool displayed the Euclidean distance in pixels. The length of the pixels was then converted to the actual distance by comparing with the length of pixels of the scale bar available in the SEM images.

The quantitative analysis of the progression of fouling inside the membrane was analyzed using digital image processing. The fouling was determined by comparing the thickness of the membrane matrix between the control and the membrane filtered with 50 and 200 µg of plasmid DNA. The thickness of the membrane matrix is measured as the length of the individual thickness of the matrix (that contained the skeleton of the polymer that made up the matrix with the accumulated DNA around it) at certain location of pore (Figure 3.2). The comparison also was made between the thicknesses of the membrane matrix at the upstream, middle and downstream parts of a severely fouled filter (with 200 µg DNA) (Figure 3.3).

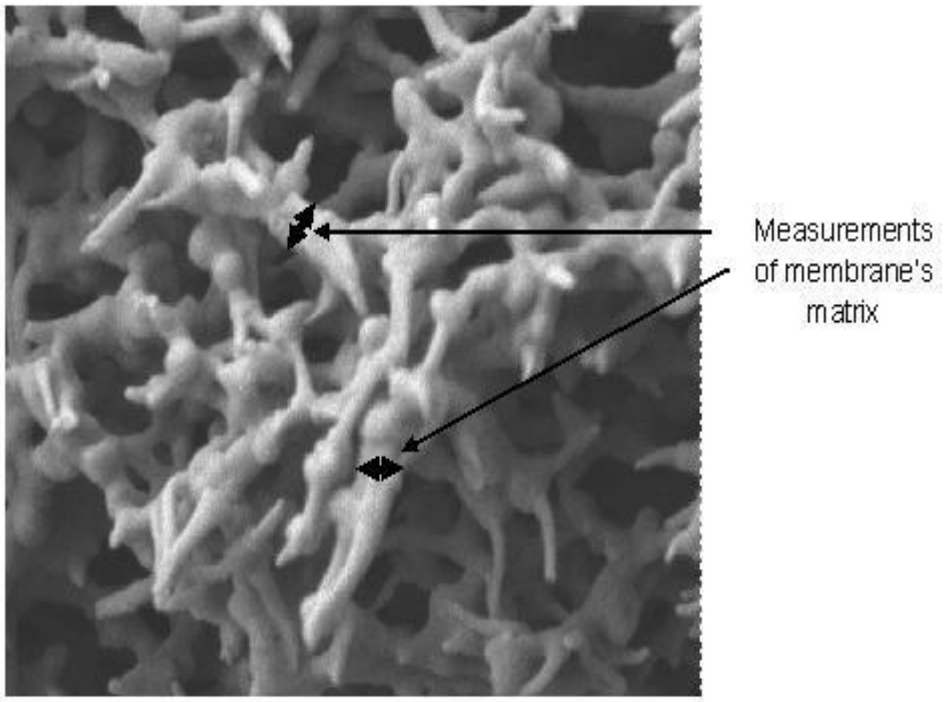

Figure 3.2 - Method for the measurement of the thickness of membrane's matrix using measurement tool available in Matlab.

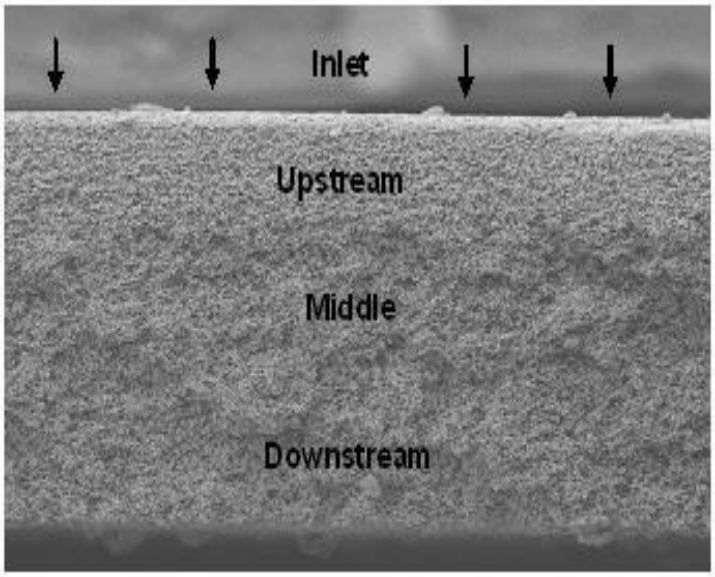

Figure 3.3- Classification of different parts of membrane. The cross section of membrane can be classified in three parts; the upstream, middle and downstream.

The effective filtration area at the surface of the membrane was measured by comparing the open area (pore space) with the area occupied by the membrane matrix and the areas that were blocked by the plasmid. The images of the surface area of the intact membrane and the membrane after filtration with 50 and 200 µg plasmids DNA were analyzed to obtain the effective filtration area during the progression of the fouling.

The surface analysis of the membrane was done by applying digital image processing using Matlab. The images of the membrane acquired by scanning electron microscopy were exported to Matlab and converted to binary images. The images were then segmented using intensity threshold and smoothed by the eroding algorithm that is available in the software. By segmenting the images, the ratio between open and fouled area can be calculated. In addition, the segmentation of the images eliminated the non-surface layers of membrane matrix (the layers underneath the upstream surface of membrane) and thus increased the accuracy of the measurement of membrane surface area. To simplified the analysis, the pore was categorized into two types; first is the pore that is formed at the surface of the membrane and second is those form between layers of the pores (void)(Zeman and Denault, 1992). The characterization between void and pore was made by Zeman and Denault (1992) who characterized a membrane as agglomerate of overlapping voids (cell) and planar orifices pores. To assess the progression of fouling from the surface of the membrane, the latter type of pore (void) was ignored (Figure 3.4). Figure 3.5 represents the chain of image segmentation analysis of the surface of a severely fouled membrane.

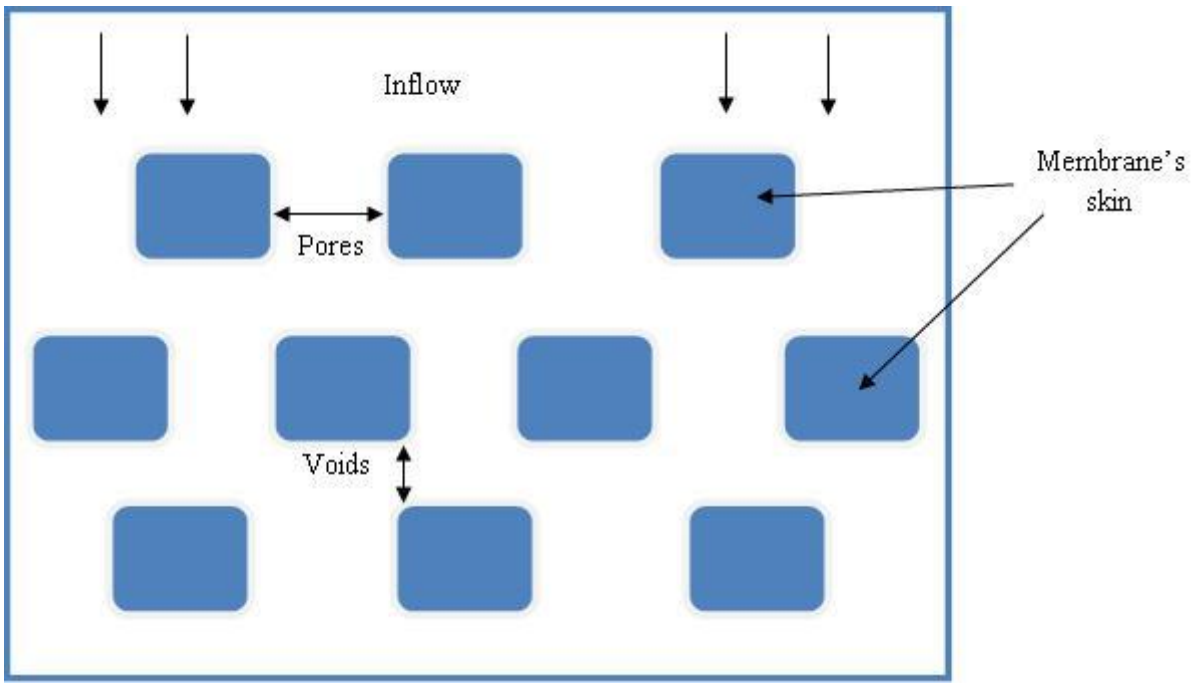

Figure 3.4- The difference between pore and void. The membrane's skin is the skeleton of matrix of membrane and the arrows represents that inflow of feed stream.

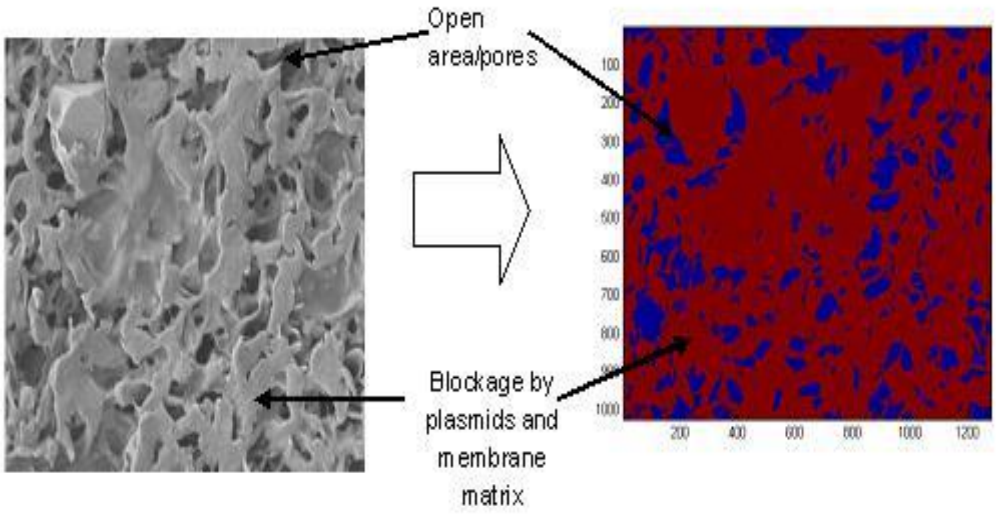

Figure 3.5- The example of image segmentation of the upstream surface of a membrane using the image processing toolbox available in Matlab.

The segmentation of the images involved assignment of zero pixel matrix value to the open areas of the membrane as opposed to unity pixel matrix values for the blocked surface areas. The ratio between zero to non zero matrix elements represents the percentage of the effective filtration area of membrane.

3.3 **Results and discussion**

3.3.1 ***Control and methodology development***

In order to study the retention of pGEc47 (56 kb) plasmids inside a 0.22 µm filter, first the impact of DNA elution buffer (10 mM Tris EDTA) on the method used for preparing samples for scanning electron microscopy was investigated. The membrane after filtration with sterile water is compared with the membrane after filtration with 10 mM TE buffer (Figure 3.6 and Figure 3.7). Crystallization of salt in buffer was detected at the surface of the membrane (Figure 3.7). The appearance of the crystals in the SEM image severely complicates the quantification of the degree of fouling, so the DNA was dissolved in sterile water instead of TE buffer during plasmid preparation.

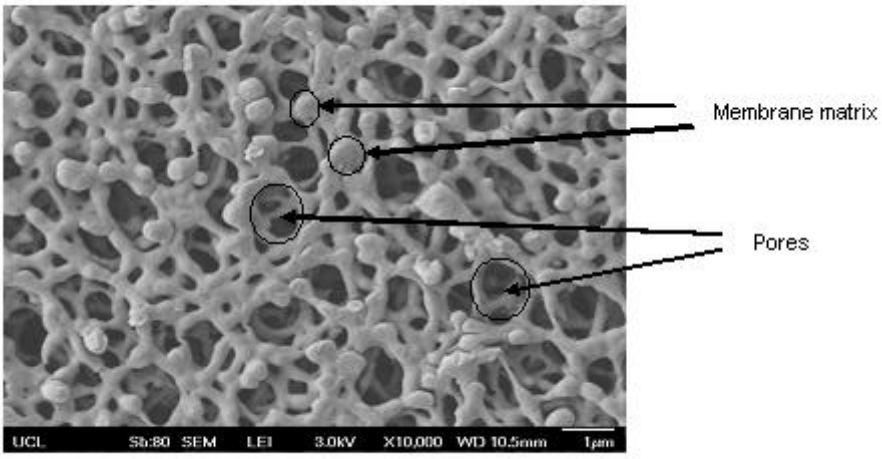

Figure 3.6- The image of PVDF membrane after filtration with sterile water at 10,000 times magnification. The filtration was operated at 1 bar transmembrane pressure.

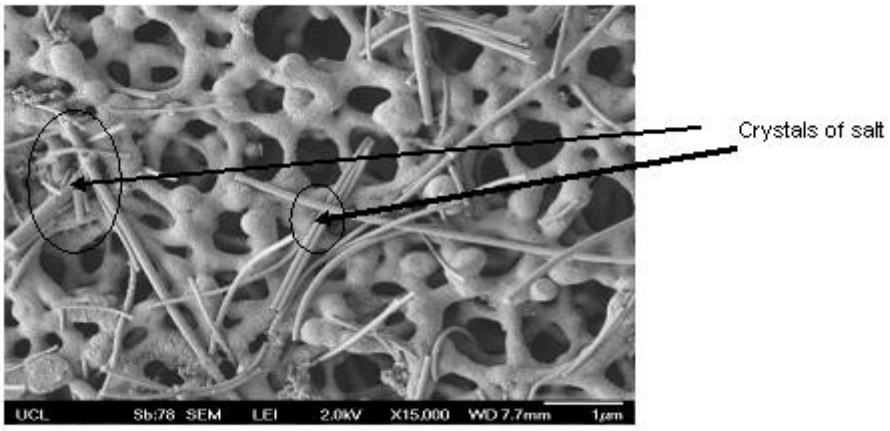

Figure 3.7- The image of PVDF membrane after filtration with 10 mM TE buffer at 15,000 times magnification. The filtration was operated at 1 bar transmembrane pressure.

3.3.2 ***The observation of fouling from the cross section of membrane***

The mechanism of supercoiled plasmid DNA fouling during constant pressure filtration at 1 bar in 0.22 μm PVDF membranes was investigated by filtering two different quantities of plasmid DNA (50 and 200 μg). The feed solution used in this experiment contained > 90% supercoiled content and was confirmed by densitometry analysis using agarose gel electrophoresis. The purity of the DNA against proteins and organic molecules was confirmed by spectrophotometry analysis.

The appearance of the membrane matrix and DNA is similar after the gold coating technique used to prepare the SEM samples. The degree of fouling is judged by comparing images of a fouled membrane with those of a control membrane after the filtration with sterile water.

The comparison between control (membrane filtered with water) and fouled membrane indicated significant build-up of DNA around the matrix of the interconnected pores (Figure 3.8, Figure 3.9 and Figure 3.10).The cross section of the fouled membrane showed an increase of the thickness of the membrane matrix suggesting that plasmid DNA was layered on the surface of the matrix and consequently blocked the pores.

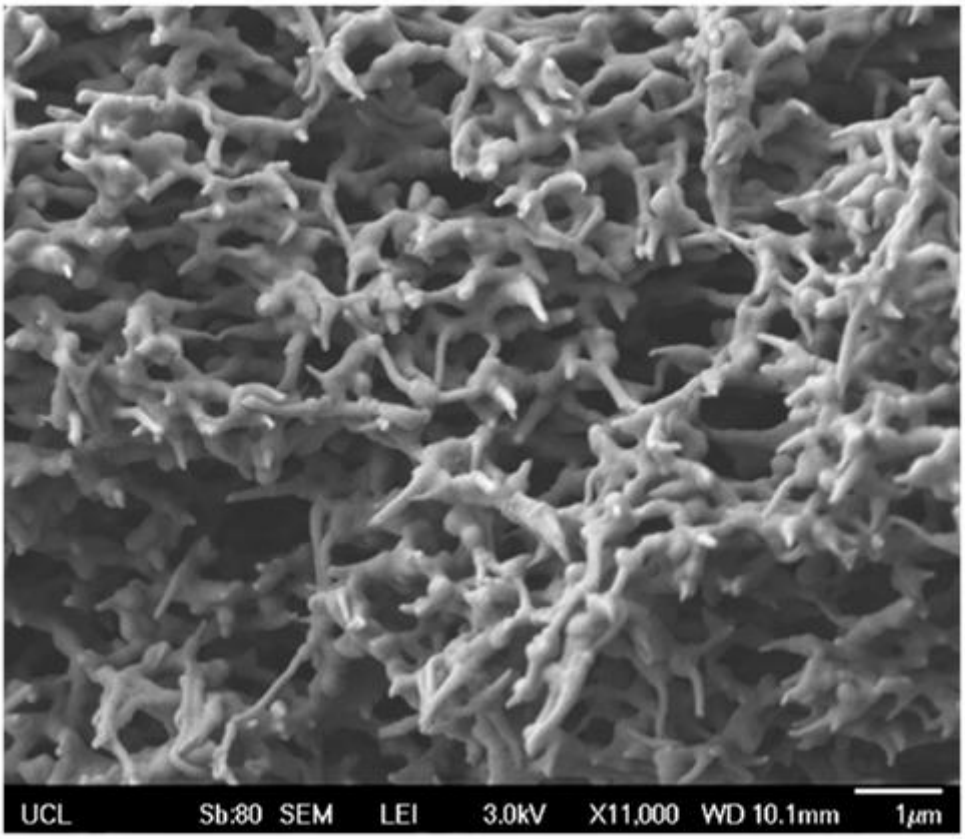

Figure 3.8- The SEM image (x 11 000 magnifications) of cross section of PVDF membrane after filtration with sterile water. The filtration was operated with 13-mm Durapore® 0.22 µm PVDF membrane at 1 bar.

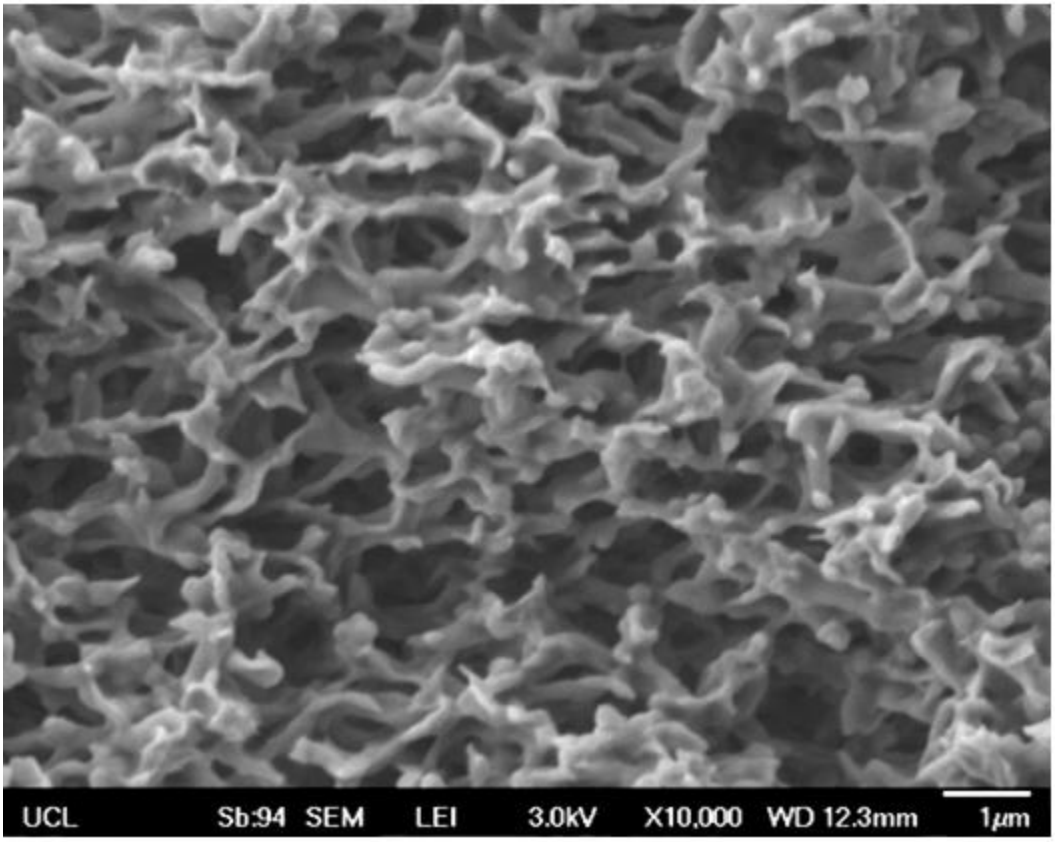

Figure 3.9**-** The SEM image (x10 000 magnifications) of cross section of PVDF membrane after filtration with 50 µg pGEC47 (56 kb) plasmid DNA. The filtration was operated with 13-mm Durapore® 0.22 µm PVDF membrane at 1 bar.

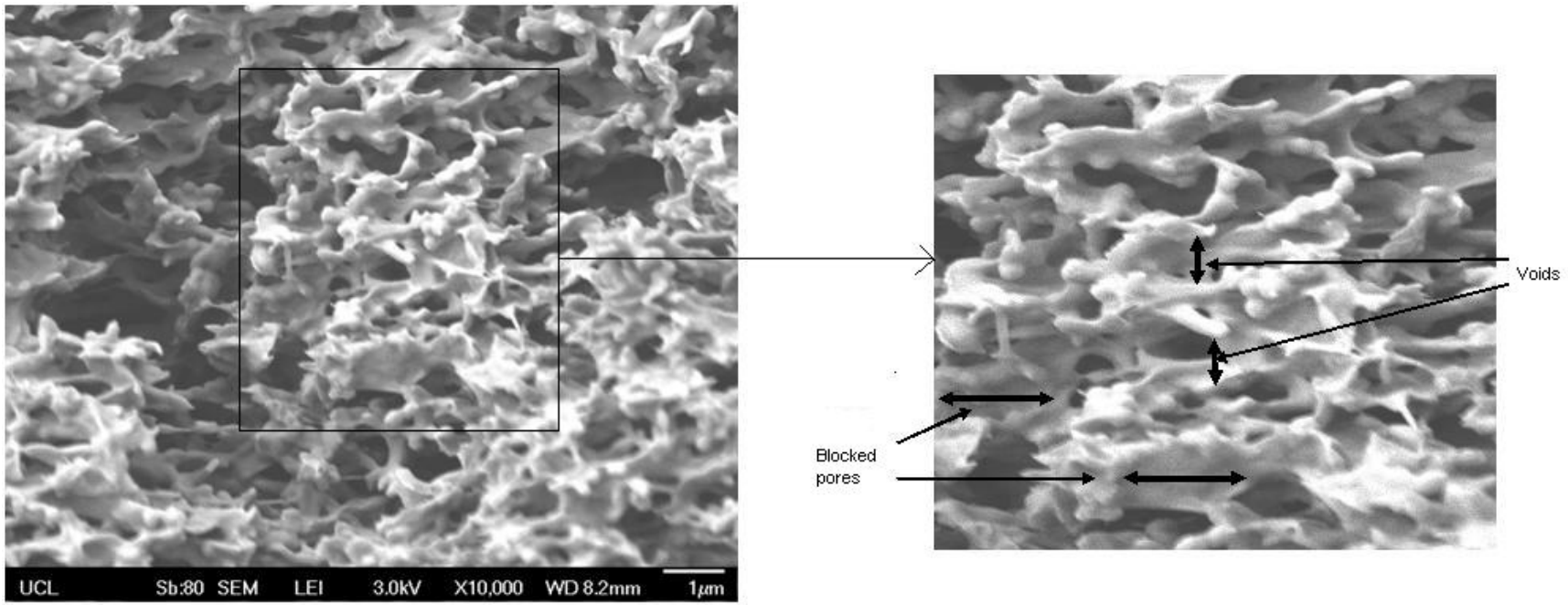

Figure 3.10- The SEM image (x10 000 magnifications) of cross section of PVDF membrane after filtration with 200 µg of pGEc47 (56 kb) plasmid DNA. The filtration was operated with 13-mm Durapore® 0.22 µm PVDF membrane at 1 bar.

The analysis of images after filtration with 200 µg plasmids showed that the blockage was due to the entrapment of plasmid DNA that blocked the entrance of the pores. Whilst the entrance of some of the pores becomes blocked, others remain open. Furthermore the void spaces between the layers of pores remain open and available for transport of other plasmid molecules (Figure 3.10).

In describing the fouling of the membrane, the constriction and blockage of pores by plasmid DNA were correlated with the worm-like chain (WLC) model of DNA. The model explains that DNA can be represented as freely-jointed segments of an elastic and flexible rod that curve smoothly along its structure (Bustamante et al., 2000). The study on a single molecule inside a microfluidic funnel suggested the accumulated elongational fluid strains influenced the elongation of the DNA structure (Larson et al., 2006). However, inside a membrane, the plasmids experience a combination of fluctuating shear and elongation strain rates. Consequently, these phenomena influenced the trajectory and conformation of plasmids by elongating and deforming the molecules and being the potential factor for the entrapment of these molecules (Hirasaki et al., 1995, Latulippe et al., 2008).

In the case of pGEc47 plasmid (56.5 kb), the contour length of linear DNA can be calculated by multiplying the number of base pairs with the axial rise between the base pair (approximately 0.34 nm). Since the plasmid used contained mostly supercoiled plasmid DNA, the number should be multiplied by 0.4 to account for the fact that the supercoiled topology of the plasmid DNA reduces its contour length to 40 % of that of linear DNA (Strick et al., 1998). For the pGEc47 plasmid that contains approximately 56 000 base pairs, the calculated contour length was approximately 7.6 µm. A fully stretched plasmid molecule can elongate to span across several layers of pores. Besides the elongation of plasmid molecules, the strain rates also cause rotational motion of plasmids (Arulmuthu et al., 2007) and consequently during its trajectory, the plasmids will experience ranges of conformations such as dumbbell, half-dumbbell and random coil-shape (Perkins et al., 1994).

The long chain of the flexible elongated plasmid DNA can become trapped inside the membrane since different parts of the molecule experienced different elongational profiles. The schematic diagram on the mechanism of plasmid entrapment is described in Figure 3.11 and Figure 3.12.

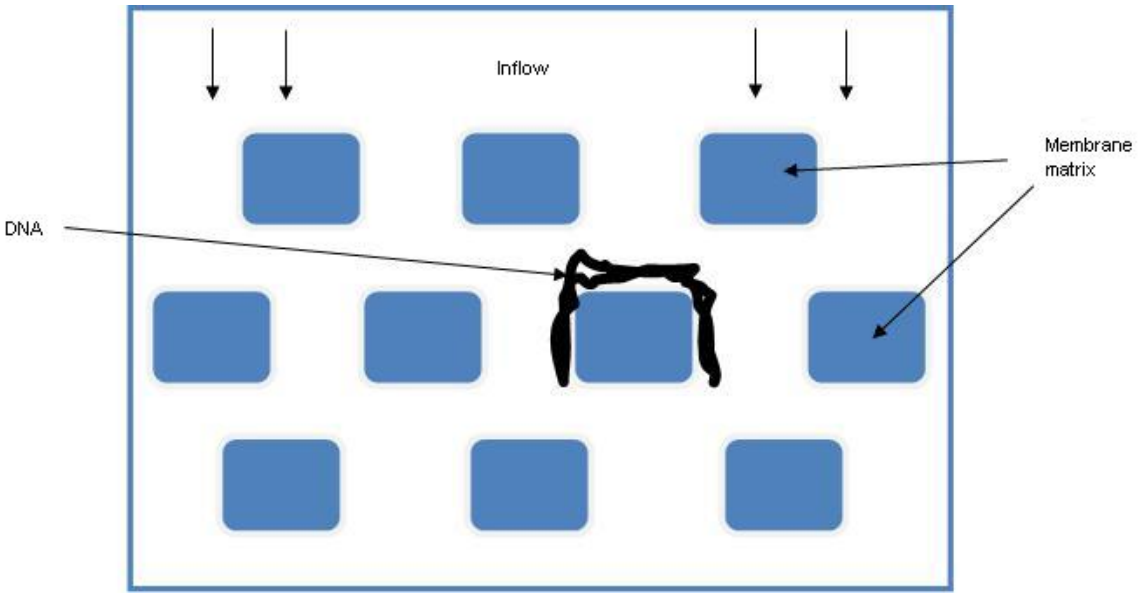

Figure 3.11- Schematic representation of possible entrapment of a single plasmid DNA during filtration.

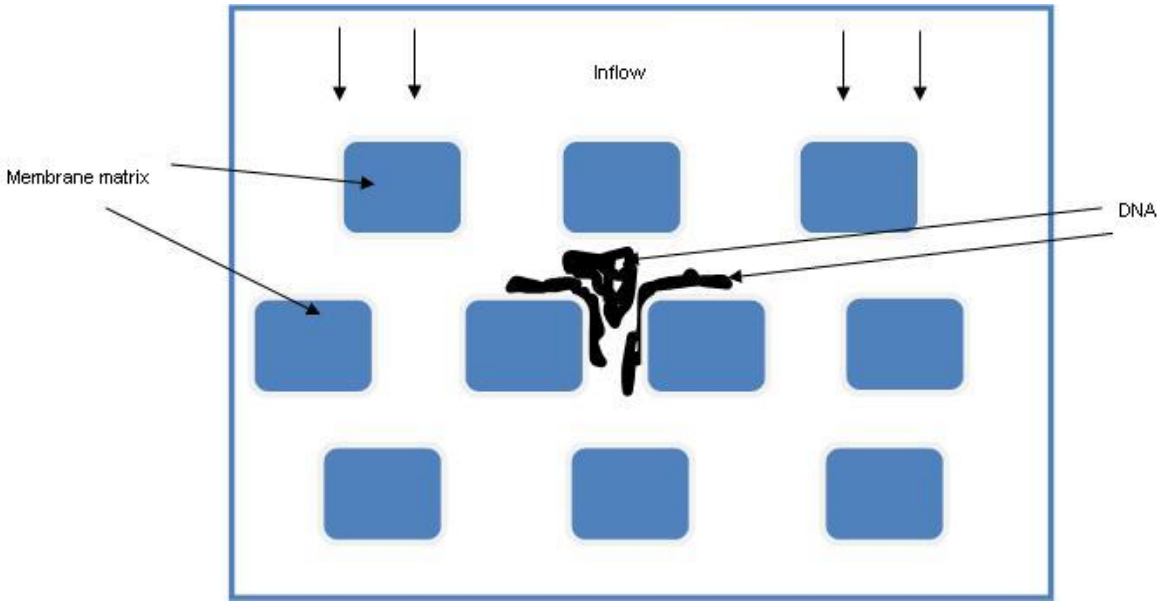

Figure 3.12- Schematic representation of plasmids that entrapped inside the membrane.

The plasmids can also become entangled with other plasmid molecules and intertwined with the interconnected pore structure inside the membrane. Sketches of this type of accumulation of the plasmids in Figure 3.11 and Figure 3.12 contribute to the blocking of membrane pores. It should be noted that the plugging of pores inside the membrane also contributes to the reduction of the opening of void spaces inside the membrane. As described in the pore constriction blocking model, the increase of membrane resistance is due to the constriction of pore throat by particles that accumulate inside the wall of the pore. However, during filtration of pGEc47 (56 kb) plasmid, the increase of membrane resistance was suspected due to the constriction of void spaces by meshes of accumulated plasmids.

The theory of plasmid entrapment that is presented is in agreement with the observation of DNA permeation using transmission electron microscopy. Hirasaki et al (1995) observed that the filtration flow effects influenced the deformation and elongation of plasmid molecules where the random coil DNA was observed in a hairpin conformation during its trajectory through the pore (Hirasaki et al., 1995). When filtering a high concentration of DNA, the trajectory of high concentration of plasmids converging towards a single pore contributed to the plugging of the pore.

The observation of several electron microscopy images of a membrane after filtration with 200 µg plasmids also suggested localized blockage of the pores since only certain parts inside the membrane experienced severe fouling. The severely blocked pores totally obstructed the passage of plasmid molecules and are thought to be influenced by the topological network of the intact membrane (Figure 3.13). The SEM image in Figure 3.13 illustrates the cross section of a membrane that contains distributions of high and low density of interconnected pores.

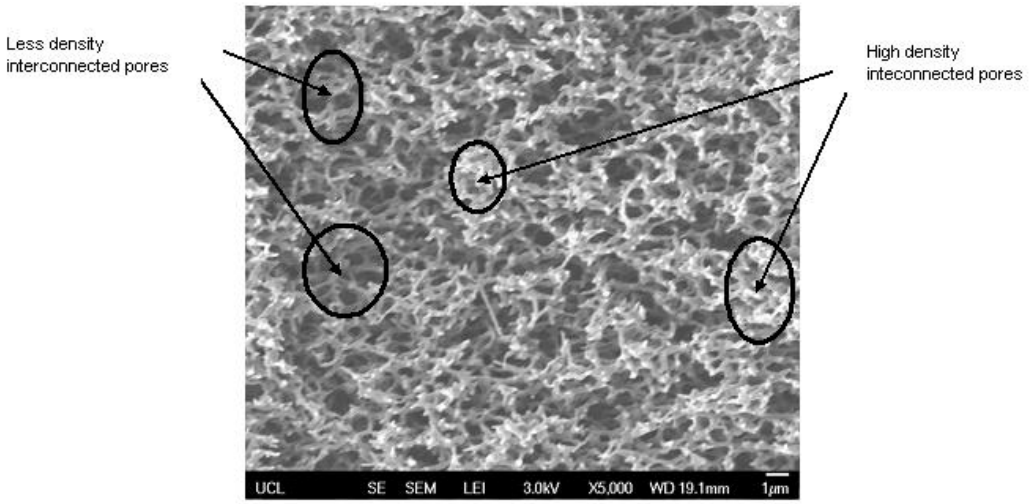

Figure 3.13 shows the heterogeneous surface of the cross section of PVDF membrane. The arrows indicate the high and less density pore structures. The SEM image was acquired at x5000 magnifications.

Different membrane composition and topological network is proved to influence the capacity of membrane for filtration of plasmids as described by Watson et al (2006). Additionally, the knowledge that the clogging of plasmid DNA is severe in a high density network of pores suggests that the selection of filter that contains a homogenous topological network is preferable in the filtration of a long chain polymer.

The comparison between membranes after filtration with 50 and 200 µg of plasmids indicated that the increase of processed volume has increased the retention of plasmids inside the membrane (Figure 3.14). However, the build-up of the foulant around the membrane matrix after filtration of 50 µg plasmid DNA was higher compared with the increase during the filtration of

>50 µg up to 200 µg of plasmid DNA. Approximately an average of 300 nm increase of foulant around the membrane matrix was observed during filtration of the first 50 µg plasmid DNA compared with only 150 nm increase of build-up during filtration of further 150 µg plamid DNA. The smaller build-up of fouling during filtration of >50 µg to 200 µg of plasmids might due to the fact that during this stage, the retention of plasmid was primarily at the surface of the membrane.

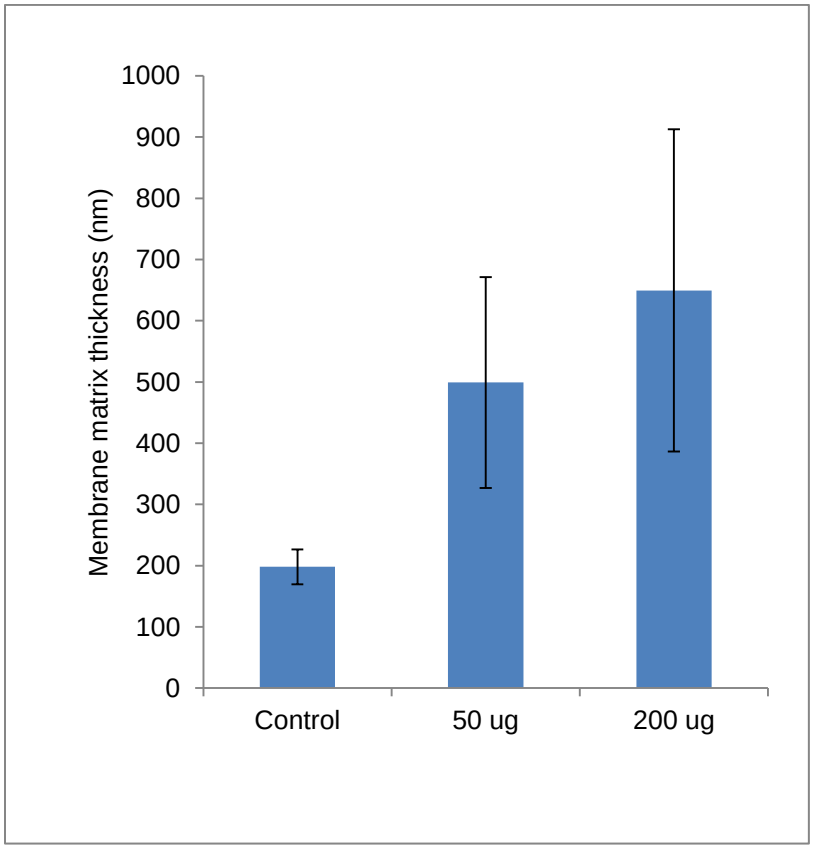

Figure 3.14- Comparison of the cross section of SEM images of the thickness of membrane matrix in control membrane with the thickness of foulant around the matrix of membrane after filtration with 50 and 200 µg pGEc47 (56.5 kb) plasmid. The measurement of the thickness of foulant around the membrane matrix was done by digital image processing tool available in Matlab. The measurements of the thickness of foulant were the average of 10 measurements at upstream of membrane from five sets of SEM images. The error bars represent the standard deviation above the mean (n=5).

The distribution of plasmids that were trapped inside the membrane was homogenous at the upstream, middle and downstream parts of the membrane with a slightly increased level of fouling of pores towards the downstream side (Figure 3.15). Figure 3.15 gives an insight on the penetration profile of plasmid molecules confirming that the flexibility of the DNA structure

allows it to penetrate the pore by experiencing structural deformation. The penetration profile of plasmid DNA is different from the virus and protein filtration. Confocal scanning electron microscopy study of the filtration of bacteriophage MS2 and ppp7 (rigid shape virus) inside a homogenous filter showed that the virus was only retained at the entrance side of the membrane (Bakhshayeshi et al., 2011). The comparison between the transmission of DNA and protein showed that DNA with a molecular size 100 times larger than a protein had the same mass balance profile in a 35 nm filter(Hirasaki et al., 1995). The results suggested that plasmids DNA can perform structural deformation to penetrate the pores.

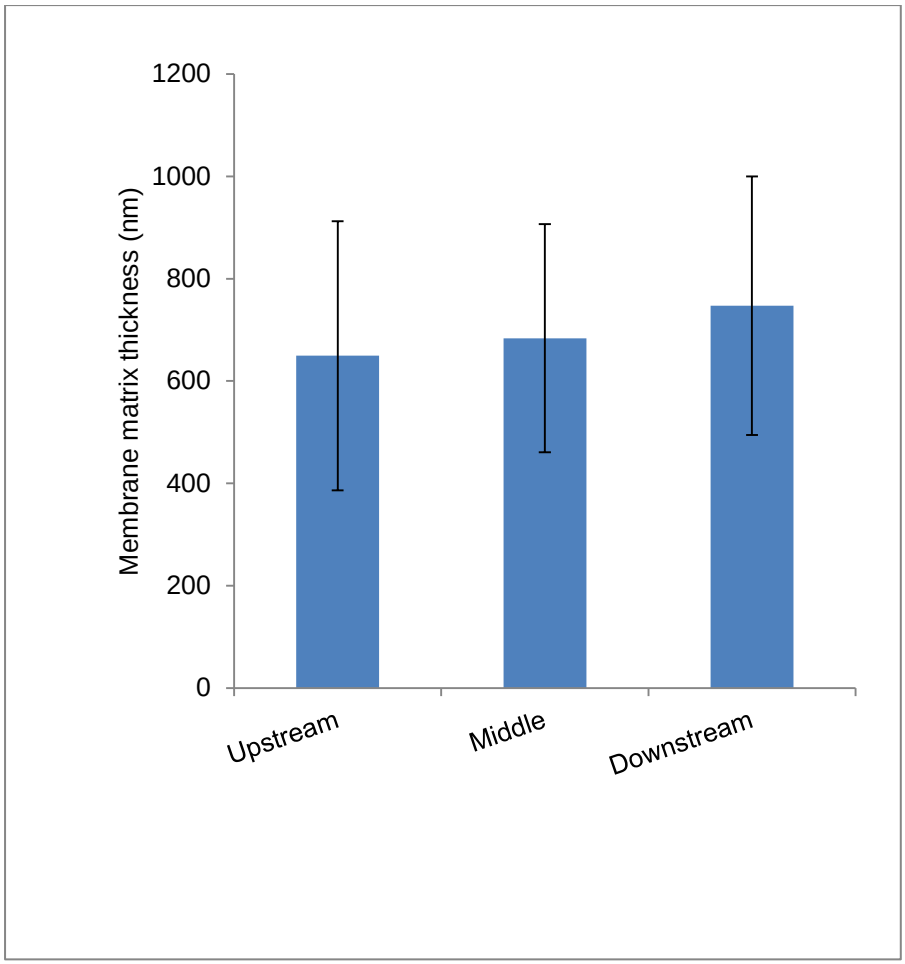

Figure 3.15- The comparison of the thickness of foulant that accumulated around membrane matrix from analysis of SEM images after filtration with 200 µg plasmid DNA. The measurement of the thickness of foulant around the membrane matrix was done by digital image processing tool available in Matlab. The measurements of the thickness of foulant were the average of 10 measurements from five sets of SEM images. The error bars represent the standard deviation above the mean (n=5).

3.3.3 ***The observation of fouling from the surface of membrane***

Figure 3.6 indicates the image of the surface of PVDF membrane after filtration with sterile water. The pore size diameter measured in the electron micrograph was approximately 1 µm compared with the manufacturer data that stated the average pore diameter of the membrane is 0.22 µm.

Figure 3.16 shows the upstream side of the surface of PVDF membrane after filtration of 200 µg of plasmid DNA at 1 bar transmembrane pressure. Comparison of this image with Figure 3.6- taking into account the differences in the magnification of the two- highlights the reduction of the effective filtration area (the total filtration area that is exposed to flow) compared with the intact membrane.

Analysis of the fouled membrane at higher magnification indicated that both surface and entrance of the pores were totally blocked by plasmid DNA (Figure 3.17 and Figure 3.18). The plugging of the pores is thought to occur as a consequence of the cumulative effects of entrapment of multiple plasmid molecules.

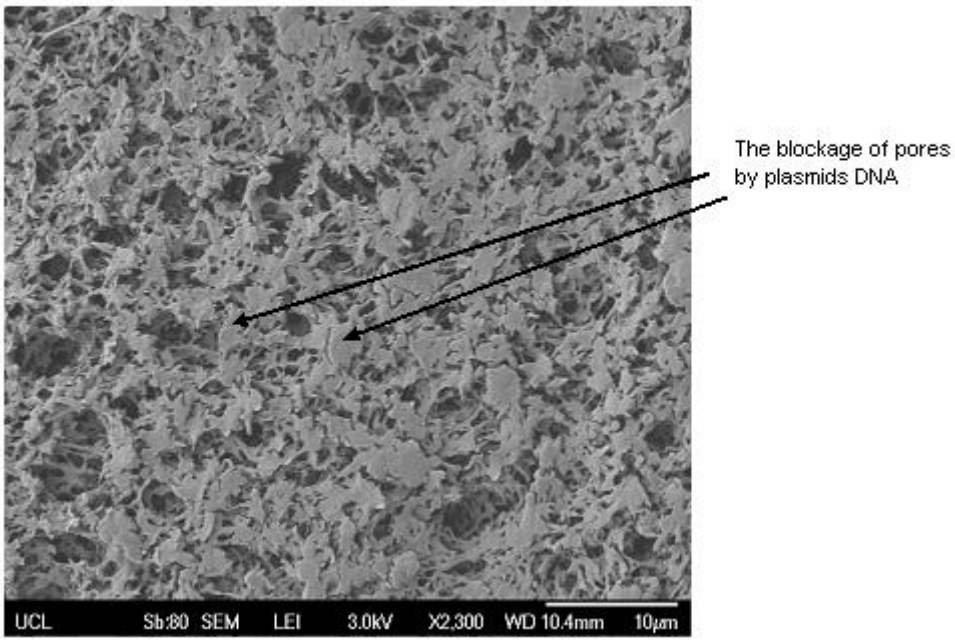

Figure 3.16- The SEM image (x 2,300 magnification) of the upstream surface of membrane after filtration with 200 µg of pGEc47 (56 kb) plasmid DNA with 13-mm Durapore® 0.22 µm PVDF membrane at 1 bar.

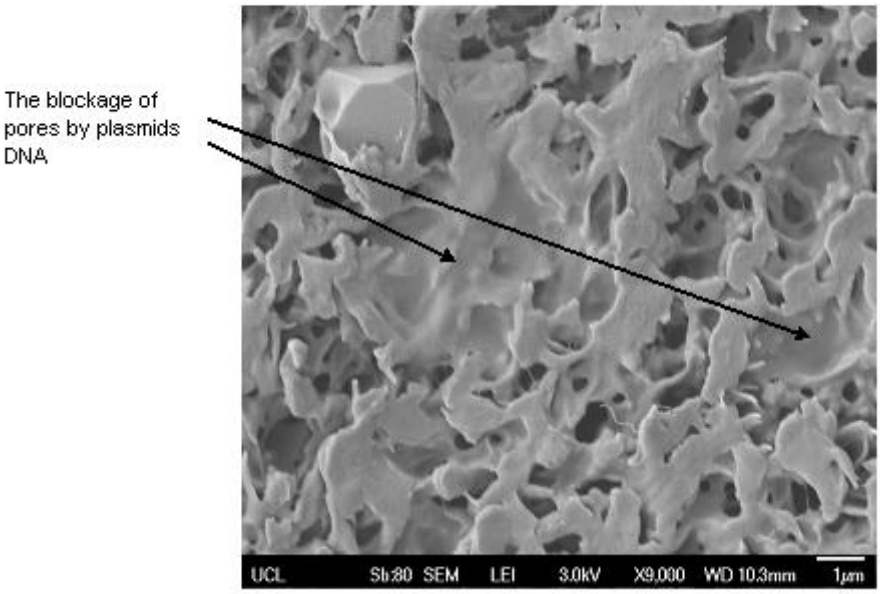

Figure 3.17- The SEM image (x 9 000 magnification) of the upstream surface of membrane after filtration with 200 µg of pGEc47 (56 kb) plasmid DNA with 13-mm Durapore® 0.22 µm PVDF membrane at 1 bar.

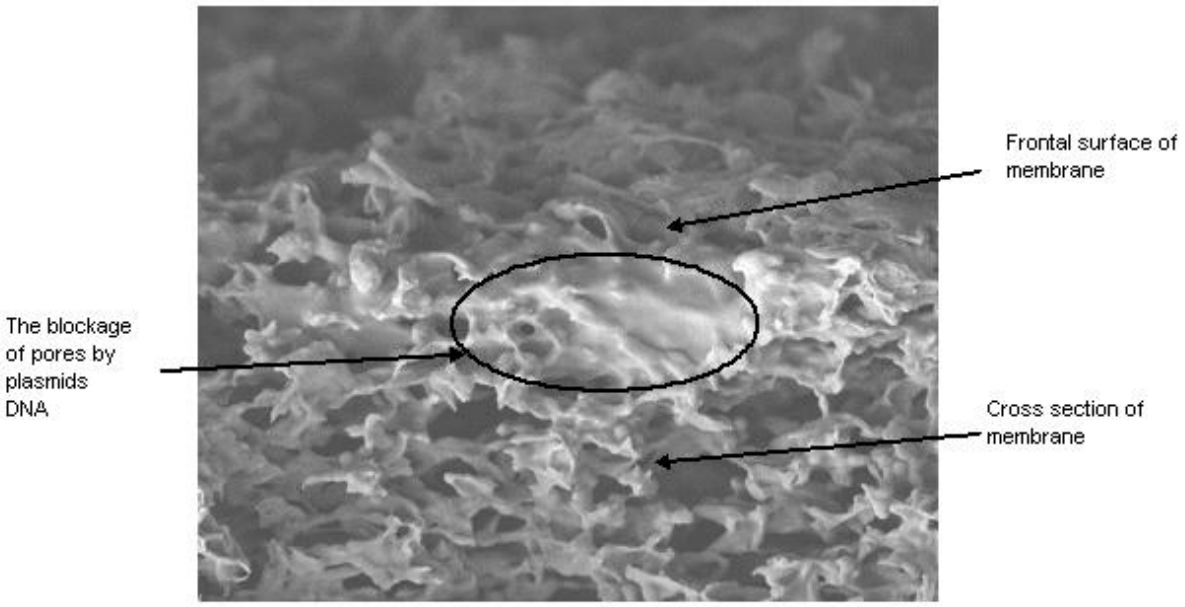

Figure 3.18 - The SEM image of the edges between the surface and the cross section of a membrane after filtration with 200 µg of plasmid DNA using13-mm Durapore® 0.22 µm PVDF membrane at 1 bar.

To investigate the progression of the fouling on the surface of membrane, images were captured at 50º degree angle from the planar stage of the SEM holder, which can provide a good impression of the distribution of entrapped plasmids with depth within the upstream surface layer of the membrane. The image of the fouled membrane after filtration with 50 µg of plasmid provided an insight that the plasmids created meshes of DNA (Figure 3.19 and Figure 3.20) at the surface of the membrane before the complete blocking of pores occurred (Figure 3.21). Figure 3.19 and Figure 3.20 indicated that after the passing of 50 µg DNA, the build-up of the meshes of DNA was observed. However, the meshes did not severely block the membrane and it still allowing the passage of incoming DNA molecules. After filtration of 200 µg DNA, the build-up of DNA meshes creates layers that blocked the pores and restricted the passage of other molecules.

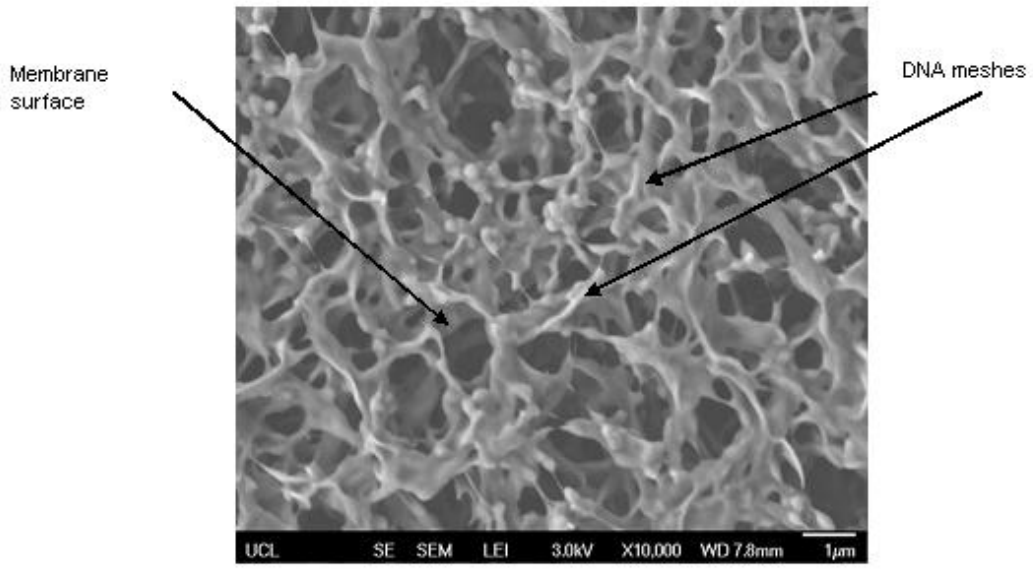

Figure 3.19- The SEM image of the surface of 13-mm Durapore® 0.22 μm PVDF membrane after filtration with 50 μg of pGEc57 (56 kb) plasmid DNA at 10,000 times magnification.

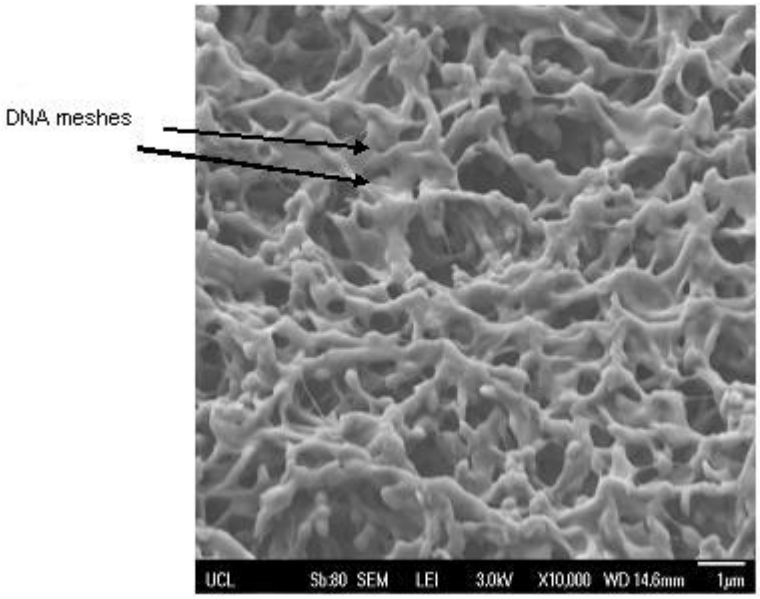

Figure 3.20- The build-up of DNA mesh at the surface of membrane after filtration with 50 µg of pGEc47 (56 kb) plasmid DNA. The scanning electron micrograph was acquired at 10,000 times magnification at 50º angle from the planar stage of SEM holder.

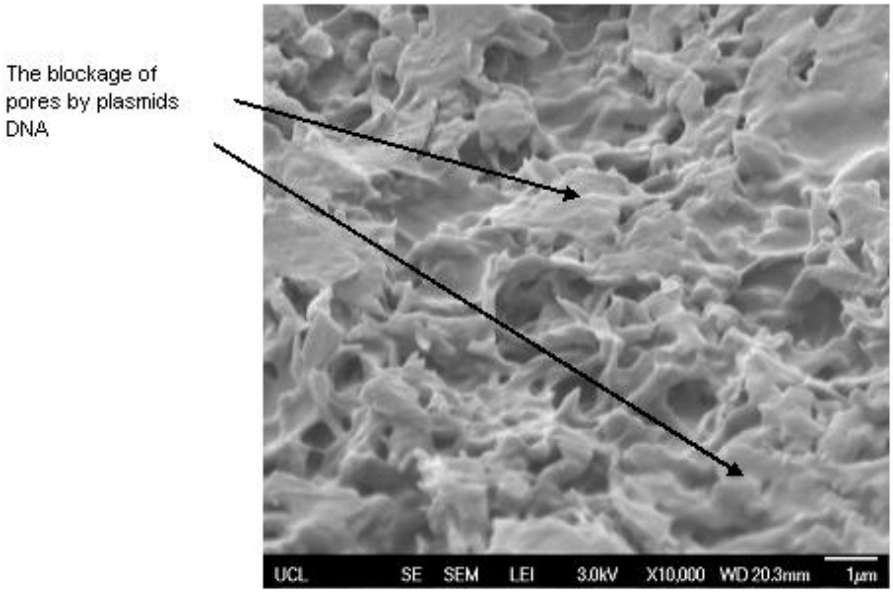

Figure 3.21- The build-up of DNA mesh at the surface of the membrane after filtration with 200 µg of pGEc47 (56 kb) plasmid DNA. The scanning electron micrograph was acquired at 10,000 times magnification at 50º angle from the planar stage of SEM holder.

The meshes of DNA on the surface of the membrane were created by plasmids that are trapped due to its structural orientation before the molecules approach the surface of the membrane. The orientation of plasmid molecules was influenced by the fluid streamlines and the molecule-molecule interactions between plasmids. The blocking of pores by pGEc47 plasmids was caused by superposition of meshes of these molecules at the surface of the membrane.

A wide range of mathematical models are used to describe the fouling of membranes. The filtration blocking models describe that the fouling mechanism can be illustrated using pore constriction (standard model), intermediate, complete, cake filtration and a combination of these models. The models describe the fouling of a membrane that contains arrays of cylindrical pores using extensions of Darcy's Law. The standard model describes that particulates constricted the inner wall of the pores. In the complete blocking model, the particulates completely seal off the entrance of the pores. The intermediate model was introduced empirically as a compromise between standard and complete blocking mechanisms (Hlavacek and Bouchet, 1993). The model is similar to the standard model but it allows the superposition of particles at the surface of the filter (Laska et al., 2005). The cake filtration model describes the presence of a cake layer on the surface of the membrane. Based on the analysis of images during the progression of fouling, the intermediate blocking model was found to dominate the fouling after filtration of 50 µg of plasmid DNA. The existence of meshes of DNA after filtration of 50 µg of plasmids illustrated the superposition of plasmid molecules that contributed to the decline of available filtration area. The continuous trend of the superposition of these molecules later sealed the pores after filtration of 200 µg plasmids. It was also found that the blockage of plasmids was not homogenous since the fouling was localized at certain parts on the surface of the membrane (Figure 3.22).

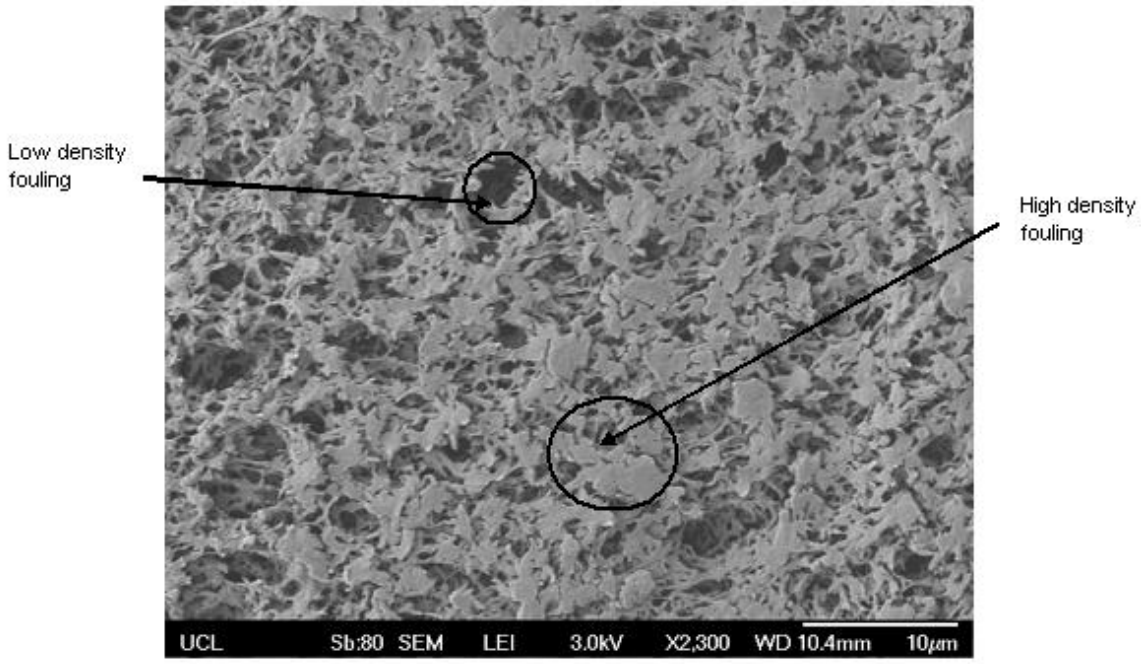

Figure 3.22- Localized fouling at the surface of 0.22 µm PVDF membrane. The SEM image was taken after filtration with 200 µg plasmids at 1 bar transmembrane pressure.

Figure 3.23 indicates that the effective filtration area of fouled membranes decreased with the increase of processed fluid. It also indicated that the build-up of meshes by filtration of 50 µg of plasmids significantly reduced the effective filtration area by approximately 37.5 %. The effective filtration area was reduced by 50 % after filtration of 200 µg plasmids.

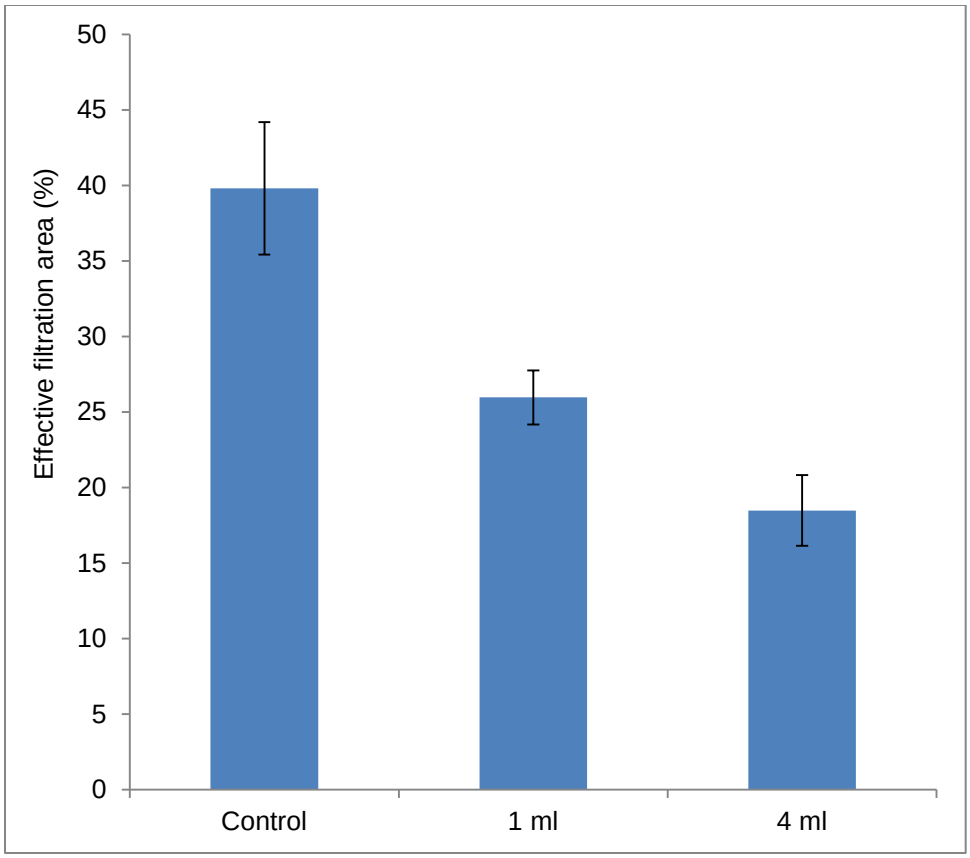

Figure 3.23- Effective filtration area of the control and the membrane after filtration with 1 ml and 4 ml of plasmid DNA. The analysis was done by digital image analysis of the membrane surface. The error bars represent the standard deviation.

The trajectory and orientation of DNA chains were suspected to be the primary factor for the creation of DNA meshes that lead to the blocking of pores after filtration with high concentration of feed. The plasmids that arrive with an orientation that is parallel to the membrane surface consequently create meshes of DNA on the surface of the membrane. When the meshes of plasmid DNA approached a critical level; i.e. where the meshes sealed the entrance of pores, the blockage of the membrane surface occurred as indicated in Figure 3.21. When the plasmid molecules orientated along the streamline of flow, the trajectory of plasmid will align with flow axis and consequently assisting transmission of the plasmid. A schematic diagram of plasmid DNA blocking the membrane is shown in Figure 3.24.

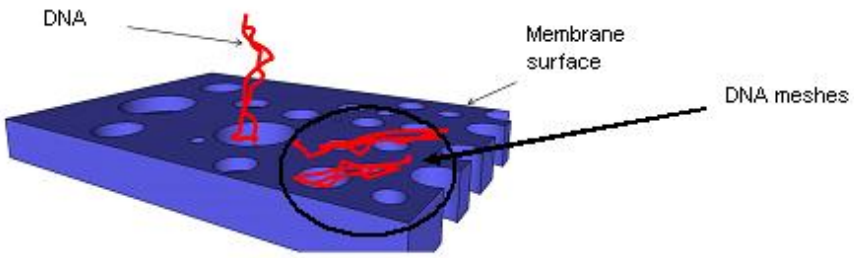

Figure 3.24- Schematic diagram of trajectory and orientation of plasmids when approaching the surface of membrane. In dynamic fluid flow regime, some of the plasmid DNA aligned with fluid streamline and penetrated the pore. Others might fall parallel to the pore entrance and created meshes of DNA on the surface of membrane.

The combination of the reduction of pore area and blockage of pores was suspected to be the primary contribution to the flux decline in pGEc47 plasmid filtration using 0.22 µm PVDF membranes. We suggested that the combination of fouling occurred in a transition process; after filtration of 50 µg plasmids, the mechanism of fouling can be correlated to a reduction of pore area and later the fouling was dominated by the blockage of the pores after the passing of 200 µg of plasmids. However, the build-up of DNA layers that contributed to the pore blockage was developed at early time of filtration. In addition, as suggested in Figure 3.14, the accumulation of plasmids inside the membrane continuously occurred even after the entrance of the pore was severely blocked by DNA.

The investigation on the fluid flow regime at the surface and inside the membrane is useful to predict and design the appropriate pore structure for increasing plasmid penetration and subsequently enhance the membrane volumetric capacity.

3.4 **Conclusion**

The entrapment of plasmid DNA is different from the entrapment mechanism of other biological materials such as in virus and protein filtrations. Plasmids DNA blocked the surface of membrane by accumulation of DNA meshes in contrast with blocking mechanism of several proteins that completely plug the pore. The meshes of plasmids were also accumulated at the entrance of pores inside the membrane. These meshes totally blocked the pores and constricted the voids between the layers of the pores. The mechanism is in contrast to the blocking mechanism of proteins where the retention is caused by the constriction of the pores.

Based on the entrapment behaviour of plasmids at the surface and inside the membrane, the trajectory of the plasmid is one of the important parameter that determined the retention of this molecule during filtration. It is important to understand the behaviour of plasmid DNA during membrane filtration in order to optimize the transmission of plasmids and to increase membrane capacity.

The architecture of the membrane is thought to be the key element in the entrapment of plasmid DNA inside PVDF filter and lead to the fouling of the membrane. The retention of plasmid at the surface and inside the membrane is primarily due to the orientation and trajectory of this flexible molecule. Since the trajectory of this molecule highly depends on the local flow field, it is thought that the improvement and selection of appropriate filter might reduce the fouling.

4 Application of filtration blocking models to describe fouling and transmission of large plasmids DNA in sterile filtration

4.1 Introduction

In this chapter, the progress of fouling during constant pressure filtration can also be characterised by mathematical analysis of flux decline during filtration. By employing filtration blocking models, firstly the mechanism of fouling and secondly the transition of the progress of fouling in the filter can be determined. Conventional filtration blocking models are regularly applied to investigate fouling mechanism and to predict the capacity of the membrane which is critical for filter scale-up. Four classical filtration models describe the mechanism of fouling during particle filtration through the following mechanistic models: (i) standard blocking (gradual pore constriction), (ii) complete blocking (sealing of pore entrances), (iii) intermediate blocking (sealing and accumulation on membrane surface) and (iv) cake filtration models (Hermia, 1982). Combinations of these models were later developed to account for more complex fouling mechanisms during filtration (Bolton et al., 2006, Ho and Zydney, 2000, Zydney and Ho, 2002). The equations governing the filtrate volume collected as a function of time for each model are summarized in Table 4.1. In the equations, V is the filtrate volume (m^3), V_0 is the initial volumetric flow rate (m^3/s), A_0 is the initial membrane frontal area (m^2), t is time (s) and k_s, k_i, k_b, k_c, and k_{ic} are filtration constants.

Table 4.1- Summary of classical and combined constant transmembrane pressure filtration blocking models

Models	Equations	Fouling parameter
Standard blocking	$V = (V_0 t)\left(1 + \frac{k_s V_0}{A_0} t\right)^{-1}$	k_s (m^{-1})
Intermediate blocking	$V = \frac{1}{k_i} \ln(1 + k_i V_0 t)$	k_i (m^{-3})
Complete blocking	$V = \frac{V_0}{k_b}\left[1 - \exp(-k_b t)\right]$	k_b (s^{-1})
Cake filtration	$V = \frac{1}{V_0 k_c}(\sqrt{1 + (2k_c V_0^2 t)} - 1)$	k_c ($s.m^{-6}$)
Intermediate-standard	$V = \frac{A_0}{k_{ic}} \ln\left(1 + \frac{2k_{ic}(V_0/A_0)t}{2 + k_s(V_0/A_0)t}\right)$	k_{ic} (m^{-1}) and k_s (m^{-1})
Complete-standard	$V = \frac{V_0}{k_b}\left(1 - \exp\left(\frac{-2k_b t}{2 + k_s(V_0/A_0)t}\right)\right)$	k_b (s^{-1}) and k_s (m^{-1})

The filtration blocking models were developed based on the assumption that the process fluid contains spherical particles. However, whether these models can explain the filtration behaviour of plasmid DNA, especially large plasmids has not been reported. DNA is a flexible and a long chain-like molecule in contrast with rigid shaped proteins or other biological materials. Furthermore, the conformation and orientation of plasmids in liquid solution are dynamic and influenced by fluid flow (Haber et al., 2004, Larson et al., 2006). In this work, an investigation of the validity of filtration blocking models to describe the fouling of large plasmids DNA was carried out. Analysis using filtration blocking models provides information on specific fouling mechanisms that dominate the fouling during the entire course of filtration.

In cases where transition of fouling and the operative particle retention mechanisms take place during filtration, this can be estimated by analysing the relationship between the rate of variation of the instantaneous resistance to filtration and the instantaneous resistance using the following mathematical form (Ho and Zydney, 2000, Iritani et al., 1995, Bowen et al., 1995):

$$\frac{d^2t}{dV^2} = k\left(\frac{dt}{dV}\right)^n \qquad \text{Equation 4.1}$$

Equation 4.1 expresses the rate of variation of the instantaneous resistance to filtration in term of a power law function of the instantaneous resistance. The parameter *k* in Equation 4.1 is the filtration constant. The exponent *n* characterises the fouling mechanism, where *n*=0 for cake filtration, *n*=1 for intermediate blocking, *n*=1.5 for standard blocking and *n*=2 for complete blocking. Changes to the value of *n* during filtration indicate more complex fouling mechanisms that are more accurately captured by one of the combined models.

The investigation of the mechanism of fouling is important in defining optimum filtration condition; in terms of process parameters, product-membrane interactions and optimization of numerous membrane attributes such as pore architecture. The filtration blocking model is also applied to predict the maximum volumetric capacity (V_{max}) of a membrane (Rajniak et al., 2008, Zydney and Ho, 2002). Therefore, an accurate determination of specific model that describes the fouling mechanism leads to better sizing prediction during scaling up of filtration.

Before we can apply the filtration blocking models, it is important to select an accurate dominating fouling mechanism as described by the filtration blocking model. The reliability of the design of filtration process is highly dependent on an accurate model that characterises the fouling. However, the above models have their limitations due to inherently simple assumptions relating to the filter and particulate characteristics. The filter is assumed to consist of cylindrical pores whereas actual membranes exhibit highly interconnected, tortuous flow passages (Zydney and Ho, 2002). The feed is assumed to contain a suspension of hard spherical particles, but plasmid DNA molecules considered in this study are flexible and have a coiled shape structure. Furthermore, the conformation and orientation of plasmids in liquid solution are dynamic and influenced by fluid flow (Haber et al., 2004, Larson et al., 2006). Therefore the ability of these models to explain the filtration behaviour of plasmid DNA, especially large plasmids needs to be studied.

This chapter reports the findings of an investigation of a membrane during the sterile filtration of two large plasmids DNA- pQR150 (20 kb) and pGEc47 (56 kb) during constant pressure filtration with a 0.22 µm PVDF membrane. Analysis of the flux decline using filtration blocking models provides information on specific fouling mechanism that dominates the fouling during the entire course of filtration. The transmission (C_f/C_0) of the plasmids was studied in an attempt to understand the connection between transmission characteristics and with filtrate flux decline. The results enable us to comment on the applicability of a filtration blocking model to explain the fouling behaviour of large plasmid DNA during sterile filtration.

4.2 **Experimental approach**

In this work, plasmids pQR150 (20 kb) and pGEc47 (56 kb) were filtered through 0.22 µm polyvinylidene fluoride (PVDF), 13 mm membrane at 5 and 8 psi under constant transmembrane pressure filtration. The set up of filtration is described in materials and methods (Section 2.7).

The effect of plasmid size on the filtration performance was analyzed by measuring the size distribution of plasmids in terms of hydrodynamic size and radii of gyration. The hydrodynamic size of plasmids was measured using dynamic light scattering (DLS) and nanoparticle tracking analysis (NTA). The estimation of the radii of gyration was calculated using equations summarized by Latulippe and Zydney (2010) . In this work, the development of simplified equations based on Latulippe and Zydney (2010) is presented.

The mechanism of membrane fouling was determined by fitting the pore constriction, intermediate, complete, cake filtration and a combination of these models with experimental data using non-linear regression analysis. Based on the standard error of estimates of the classical filtration models, only two combined fouling models developed by Bolton et al (2006) were considered in this work which are the intermediate-standard and complete-standard blocking models. The transition of fouling mechanisms during filtration was analyzed using the power law equation as described in Equation 4.1. The effects of fouling on the transmission of plasmid DNA during filtration were also investigated in this study. The transmission of plasmid during filtration is expressed by the ratio of the concentration of DNA in filtrate over the initial DNA concentration. The concentration of plasmid was detected using UV spectrophotometry at 260 nm (A_{260}).

4.2.1 ***Power law fouling transition analysis***

To investigate the transition of fouling mechanism during filtration, the filtrate flux data was analyzed in term of d^2t/dV^2 versus dt/dV as suggested in Equation 4.1. The derivatives dt/dV and d^2t/dV^2 were computed by taking the analytical derivatives of the best fit functions (Table 4.1). The values of dt/dV were obtained by the reciprocal of the derivatives of filtrate volume vs. time plot (dV/dt);

$$\frac{dt}{dV} = \frac{1}{dV/dt} \qquad \text{Equation 4.2}$$

And the derivative of d^2t/dV^2 was obtained by:

$$\frac{d^2t}{dV^2} = \frac{d}{dV}\left(\frac{dt}{dV}\right) = \frac{dt}{dV} \times \frac{d}{dt}\left(\frac{dt}{dV}\right) \qquad \text{Equation 4.3}$$

The power law coefficient, n was then obtained from a linear regression of Equation 4.1:

$$Log\left(d^2t/dV^2\right) = n * Log\left(dt/dV\right) + C \qquad \text{Equation 4.4}$$

The average values of n during early, mid and late time of filtration of pQR150 (20 kb) and pGEc47 (56 kb) plasmids at 5 and 8 psi transmembrane pressures was estimated using Equation 4.4.

The transformation of the values of n was then estimated by differentiating the logarithm of d^2t/dV^2 with respect to the logarithm dt/dV ;

$$n = \frac{d\left[\log\left(d^2t/dV^2\right)\right]}{d\left[\log\left(dt/dV\right)\right]} \qquad \text{Equation 4.5}$$

The values of *n* were used to evaluate the trend of fouling that dominated the filtration of pQR150 (20 kb) and pGEc47 (56 kb) plasmids. The values of *n* for all types of filtration blocking models are listed in Table 4.2.

Table 4.2 - The constant pressure blocking filtration laws (Hermia, 1982)

Filtration blocking models	*N*
Standard	1.5
Intermediate	1
Complete	2
Cake filtration	0

4.2.2 ***Transmission analysis of filtrate***

The transmission of plasmid during filtration is expressed by the ratio of concentration of filtrate over initial DNA concentration (C_f/C_0). The concentration of plasmid DNA was detected using the method explained in subsection 2.5 . To obtain the concentration of filtrate at a specific time during the filtration, the filtrates were collected in batches. During the early stages of filtration (1-3 minutes) samples were collected every 10 seconds. Afterwards and towards the end of filtration samples were taken at 2 minute intervals. This compensates for the low filtrate flux towards at the end of the filtration which requires sample duration to increase.

4.3 **Results and Discussion**

4.3.1 ***Analysis of size distribution of pQR150 (20 kb) and pGEC47 (56 kb) plasmids: Experimental results and development of simplified theoretical calculations for the radii of gyration of plasmid DNA***

The information of size of plasmid is important to provide insight into the effect of size on the retention of plasmids during filtration. The size of plasmid was measured and calculated in terms of hydrodynamic size and radii of gyration.

The hydrodynamic size of a particle is measured based on the diffusion coefficient, D (m^2/s) of the particle in Brownian motion. The size of the particle is measured based on the Stokes-Einstein equation:

$$r_h = \frac{K_B T}{6\pi\mu D} \qquad \text{Equation 4.6}$$

Where r_h is the hydrodynamic radius of the particle (m), K_B is the Boltzmann constant ($m^2 kg\ s^{-2}\ K^{-1}$) and T is temperature (K). The methods for determining the diffusion coefficient of plasmids DNA were based on two technologies in particle size measurement. In this work, the dynamic light scattering (DLS) and nanoparticle tracking analysis (NTA) were applied for estimating the size of plasmid. When interpreting the results of these techniques, it should be noted that the radius of plasmid measured by the DLS and NTA is not an actual radius but a hypothetical radius that has a similar diffusion coefficient with a hard sphere particle.

Comparatively, the radius of gyration of plasmid is the average square distance from the centre of the mass of plasmid to its chain segments. In this manuscript, the radius of gyration of plasmid was estimated by simplified theoretical calculations summarized and recommended by Latulippe and Zydney (2010). The development of the simplified theoretical equations is also presented for approximating the size of plasmid. The estimation of the radius of gyration of a linear DNA was based on Benoit and Doty's worm-like chain (WLC) model (Benoit and Doty, 1953);

$$\frac{R_{g,linear}}{a} = \sqrt{\frac{L}{3a} - 1 + \frac{2a}{L} + \frac{2}{(L/a)^2}\left(1 - \exp\left(-\frac{L}{a}\right)\right)} \qquad \text{Equation 4.7}$$

Where $R_{g,\ linear}$ is he radius of gyration of linear DNA, L is the contour length of plasmid (m) and a, is the DNA persistence length (m). The contour length is obtained by multiplying the number of base pairs by the axial rise per base pair which is approximately 0.34 nm. The persistence length; the measurement of the stiffness of DNA was estimated at approximately 50 nm (Reese and Zimm, 1990).

For example, the contour length, L of pGEc47 plasmid (56 kb) is 56 000 x 0.34 nm= 19 040 nm= ~ 19 µm. Thus, the ratio of contour length/persistence length, L/a is equal to 380.8. Using Equation 4.7, the radius of gyration of a linearized pGEc47 plasmid, $R_{g,\ linear}$ is equal to 561 nm. However, Equation 4.7 can be simplified since the first term of the equation (L/3a) dominates the value of $R_{g,\ linear}$ compare with other contributions. The equation can be simplified to:

$$\frac{R_{g,linear}}{a} \approx \sqrt{\frac{L}{3a} - 1} \qquad \text{Equation 4.8}$$

Equation 4.8 yields $R_{g,\ linear}$= 561 nm which has similar value as provided by Equation 4.7.

The radius of gyration of an open circular plasmids DNA can be estimated using Equation 4.9 provided by Fujii and Yamakawa (1975) and Fishman and Patterson (1996);

$$\frac{R_{g,OC}}{a} = \sqrt{\left(2 + \frac{22}{3}\frac{a}{L}\right)\left(\frac{1}{12}\frac{L}{a} - \alpha^2\frac{2a}{L} + \alpha^3\frac{8}{3}\left(\frac{a}{L}\right)^2\right) - 1 + 4\alpha\frac{a}{L} + 8\alpha^3\frac{a}{L}\left(\frac{1}{3} - \frac{\alpha}{6} + k_2\frac{\alpha^2}{5} + k_3\frac{\alpha^3}{6}\right)} \qquad \text{Equation 4.9}$$

$R_{g,\ OC}$ is the radius of gyration of open circular DNA. Latulippe and Zydney (2010) note that in Equation 4.9 , α, k_2 and k_3 are the model parameters that are weak functions of the plasmid's contour length, L. The value of the weak functions can be obtained from best-fit of experimental data with Equation 4.9.

However, it is possible to estimate the $R_{g,OC}$ without α, k_2 and k_3 parameters by applying the same level of approximation as above by neglecting small terms in Equation 4.9 that are below the order of 1 (those proportional to a/L and powers of this factor). Thus;

$$\frac{R_{g,OC}}{a} \approx \sqrt{\frac{1}{6}\frac{L}{a} - 1}$$ Equation 4.10

The $R_{g,\,OC}$ predicted by Equation 4.10 is in good agreement with the experimental data of 3-15 kb plasmids that was investigated by Latulippe and Zydney (2010). By applying Equation 4.10, the $R_{G,\,OC}$ of pGEc47 (56 kb) is ~395 nm.

As recommended by Latulippe and Zydney (2010) , the prediction of radius of gyration of supercoiled plasmid DNA can be calculated using Equation 4.8 but the value of contour length, L should be multiplied by 0.4 as the contour length of supercoiled plasmids DNA is ~40 % of the contour length of a linear DNA (Strick et al., 1998):

$$\frac{R_{g,SC}}{a} = \sqrt{\frac{0.4L}{3a} - 1 + \frac{2a}{0.4L} + \frac{2}{(0.4L/a)^2}\left(1 - \exp\left(-\frac{0.4L}{a}\right)\right)}$$ Equation 4.11

Table 4.3 shows the radius of gyration of linear, open circular and supercoiled of pQR150 and pGEc47 plasmids DNA. Comparison between the radius of gyration of plasmids with the average size of membrane pore; ~ 220 nm (based on manufacturer's specification) indicated that based on the calculated size estimates, all plasmid topologies of pQR150 and pGEc47 plasmids could block the membrane pores during filtration.

Table 4.3 - The radius of gyration of pQR150 and pGEc47 plasmids calculated using Equation 4.8, Equation 4.10 and Equation 4.11.

Plasmid topologies	pQR150 (20 kb) (nm)	pGEc47 (56 kb) (nm)
Linear	333	561
Open circular	232	395
Supercoiled	207	352

Comparatively, Table 4.4 indicates the hydrodynamic size of pQR150 and pGEc47 that was measured using DLS and NTA.

Table 4.4- Comparison of the size distributions of plasmids pQR150 (20 kb) and pGEc47 (56 kb) with nanoparticle tracking analysis (NTA) and dynamic light scattering (DLS).

	Hydrodynamic diameter of pQR150 (20 kb) (nm)		Hydrodynamic diameter of pGEc47 (56 kb) (nm)	
	SC	OC	SC	OC
Nanoparticle tracking analysis	150-250	460-670	240-335	NA
Dynamic light Scattering	275-286	303-360	313-342	NA

Note that different metrics were used to measure the size of plasmids. The theoretical size was the radius of gyration in contrast with NTA and DLS which measures the hydrodynamic size. The radius of gyration provides insight into the root mean square distance between centre of mass of a molecule and its chain segments. In contrast, the hydrodynamic size is a sphere equivalent size of a molecule based on its translational diffusion coefficient in solution.

Table 4.3 and Table 4.4 indicate that the radius of gyration of plasmids is larger than the hydrodynamic size. For example, the diameter (calculated in term of the radius of gyration) of SC plasmids of pQR150 is ~ 414 nm ($R_{g,\ SC}$, 207 nm x 2) compared with the hydrodynamic diameter measured using NTA and DLS that ranged from 150-286 nm. It is thought that irregularity of the shape of the plasmid may impact the sizing of particles as NTA and DLS applied the equivalent sphere concept to determine the size of particle.

For pQR150 and pGEc47, the size distribution of SC plasmids measured using NTA is in good agreement with the size measured using DLS (Table 4.4). However, the detection using DLS provides a systemically smaller range of hydrodynamic size distributions. For example, the measurements of SC plasmids of pQR150 were 150-250 nm and 275-286 nm for NTA and DLS respectively, which suggested wider distribution of hydrodynamic size measured using the NTA. The detection of the size of SC plasmid for pGEc47 also indicated a similar observation where a larger distribution of plasmid size was observed using NTA.

The wider hydrodynamic size distribution detected by NTA is contributed by the technique employed in the detection of the particle. The NTA applies a counting technique that produces the number weighted distribution of each particle compared with DLS that is based on the intensity weighted distributions. In NTA, the number weighted distribution is produced by tracking individual particles and the images that are captured can be adjusted to obtain better image for analysis. Modifications such as image smoothing, background subtraction, threshold settings and blur removal might include noises that may result in a large range of hydrodynamic size distributions.

Radius of gyration of both pQR150 (20 kb) and pGEc47 (56 kb) (Table 4.3) indicated that the mean size of the plasmid molecules is larger than the nominal size of the pore (by assuming the average size of pore approximately ~ 200-220 nm; based on membrane that is validated for absolute removal of *B. diminuta*) suggesting the possibility of plasmid retention on the frontal surface of membrane. However, this metric does not fully describe the size of plasmid since it only describes the molecule if it is spherical.

The hydrodynamic size distributions of plasmids detected by NTA and DLS (Table 4.4) suggest potential retention of pQR150 and pGEc47 plasmids based on a sieving effect. However, in order to analyze the behaviour of plasmids in convective flow environment, the transformation of plasmid conformation needs to be considered. For example, a DNA molecule can change its shape from a tight conformation (random coil) to coil-stretch structure depending on the magnitude of shear and elongational stress (Smith et al., 1999). Therefore, the size of plasmid predicted in terms of hydrodynamic radius and radius of gyration should not be the only parameters to consider in predicting the fouling of the membrane. The shape and conformation of plasmids during its trajectory need to be examined in analyzing the mechanism of fouling.

The complexity of polymer orientation and its impact on fouling can be assessed indirectly using filtration blocking models. The models have been developed on the basis of the profile of resistance and available effective filtration area given by experimental results during the course of filtration. The overview and analysis of filtration blocking models has been reviewed in chapter 1.

4.3.2 ***Analysis of fouling using classical filtration blocking models***

The objectives of this study are to determine whether the classical filtration models can explain the fouling phenomena of large plasmids DNA and to find out the operative retention mechanism of the fouling; i.e. whether a single or combination of fouling mechanisms exists.

In performing the non-linear regression, the initial volumetric flow rate, V_0 (m^3/s), initial membrane frontal area; A_0 (m^2), and filtration constants; k_s, k_i, k_b, k_c, *and* k_{ic} are the required constant parameters. The filtration constant was determined numerically while V_0 was obtained from experiments and A_0 is based on specification supplied by the manufacturer. Therefore, only one parameter was determined numerically by the software and this is important to narrow the confidence interval of the plots.

The experimental data were fitted with the classical filtration models (standard, intermediate, complete and cake filtration blocking models) to investigate the ability of these models to describe the flux decline phenomena during the filtration of pQR150 (20 kb) and pGEc47 (56 kb) at 5 and 8 psi transmembrane pressures. Figure 4.1 shows the experimental data and model predictions for two of the samples (pQR150 and pGEc47 at 8 psi). The behaviours and trends of two other experiments were similar (pQR150 and pGec47 at 5 psi).

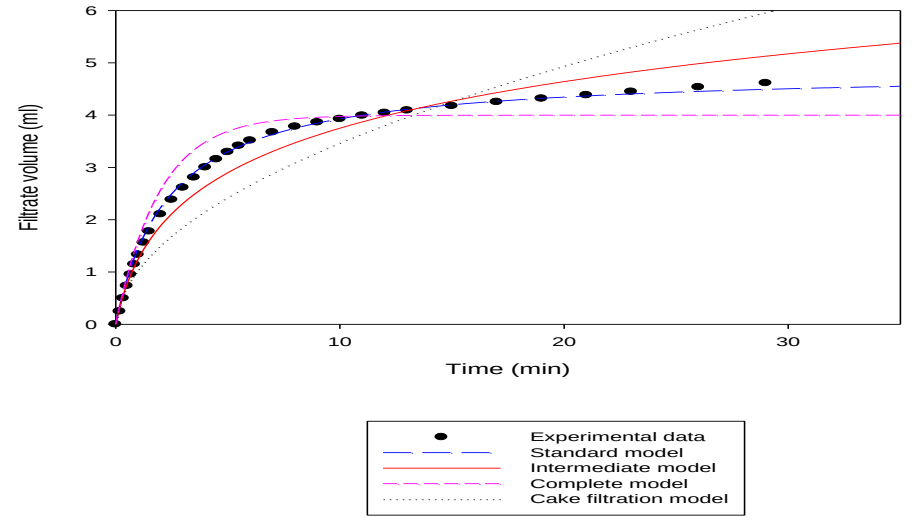

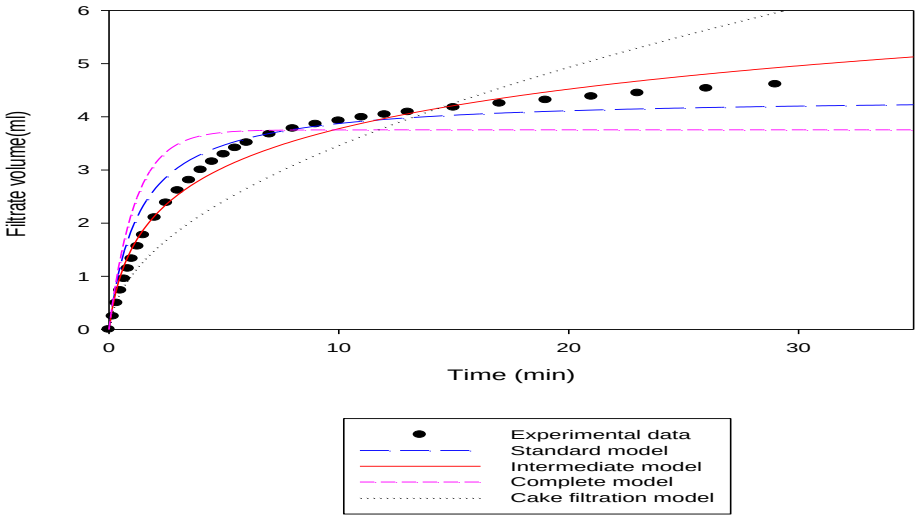

Figure 4.1- Experimental data of filtrate volume vs. time fitted with the standard, intermediate, complete and cake filtration blocking models. Plasmid solutions containing 50 µg/ml of pQR150 (20 kb) (top) and pGEc47 (56 kb) (bottom) were filtered at 8 psi transmembrane pressure through 0.22 µm PVDF membrane.

Imperfect agreement between the predictions of the classical blocking models and experimental data can be observed in Figure 4.1. The closeness of the model curves to the experimental data can also be quantified by means of the standard error of estimates (Table 4.5). The standard error of estimate describes the accuracy of the model prediction where the lowest value suggests proximity of model with experimental data.

Table 4.5 - Standard error of estimates of the filtration of pQR150 (20 kb) and pGEc47 (56 kb) at 5 and 8 psi.

Plasmid	Model	Standard error of estimates 5psi transmembrane pressure	Standard error of estimates 8psi transmembrane pressure
pOQ150	Standard	0.325	0.078
	Intermediate	0.120	0.272
	Complete	0.528	0.343
	Cake filtration	0.157	0.634
pGEc47	Standard	0.191	0.342
	Intermediate	0.221	0.198
	Complete	0.580	0.625
	Cake filtration	0.663	0.634

The results suggested that the classical blocking models were unable to describe the flux decline during filtration of pQR150 (20 kb) and pGEc47 (56 kb) plasmids. Interestingly, the experimental data showed a good fit with all models only during the first minute of filtration. The filtration of pQR150 (20 kb) at 8 psi transmembrane pressure showed that the best fit occurred with the standard model during the first 20 minutes of filtration. Large discrepancies between the experimental data and the model trends were observed towards the end of the filtration. Comparatively, the best fit of the experimental data of pGEc47 (56 kb) occurred with intermediate model but only for the first 5 minutes of filtration. The results suggest that classical models struggle to capture the filtration behaviour of larger plasmids.

The results contrast with the filtration of a small plasmid (6 kb) which followed the standard blocking model with a very good fit of R^2>0.9999 (Watson et al., 2006). The mechanism of fouling of large plasmid DNA is different from the behaviour shown in smaller size plasmid. The latter tend to behave like a small hard sphere particulates - whereas large plasmid DNA

molecules are chain-like polymers, which influences the way plasmids interact with the membrane. This lends support to the finding by Kong et al (2006) that the transmission of plasmid DNA depends on its molecular weight (Kong et al., 2010).

Based on the standard error of estimate of the non-linear regression, the comparison between all classical models indicated that the standard and intermediate models provided better fit of the data points (Table 4.5). It is observed that the blocking mechanism of plasmids in sterile filtration fall within these two models. Based on the standard error of estimates of the classical filtration models, only two combined fouling models that developed by Bolton et al.(2006) were considered in this work which are the intermediate-standard and complete-standard blocking models.

Mathematical analyses of the classical models were carried out as these models are only capable to explain the fouling behaviour during the early time of filtration. Based on the proximity of the models that fit with experimental data of the filtration of pQR150 (20 kb) and pGEc47 (56 kb) at 5 and 8 psi transmembrane pressures, only the standard, intermediate and complete blocking models are considered in this analysis. The behaviour of these models during early time filtration is determined by studying the mathematical behaviour of the expression of each model when $t \rightarrow 0$.

The Taylor series expansion is applied to the expression of standard, intermediate and complete models during early time filtration about t=0.

The equation of the standard blocking model is given by:

$$V = (V_0 t)\left(1 + \frac{k_S V_0}{A_0} t\right)^{-1} \qquad \text{Equation 4.12}$$

The first and second derivatives of the standard blocking model can be written as:

$$V' = V_0\left(1+\frac{k_S V_0}{A_0}t\right)^{-1} + (V_0 t)\left(-\frac{k_S V_0}{A_0}\right)\left(1+\frac{k_S V_0}{A_0}t\right)^{-2} =$$

$$V_0\left(1+\frac{k_S V_0}{A_0}t\right)\left(1+\frac{k_S V_0}{A_0}t\right)^{-2} + (V_0 t)\left(-\frac{k_S V_0}{A_0}\right)\left(1+\frac{k_S V_0}{A_0}t\right)^{-2} = V_0\left(1+\frac{k_S V_0}{A_0}t\right)^{-2}$$

$$V'' = -2V_0\left(\frac{k_S V_0}{A_0}\right)\left(1+\frac{k_S V_0}{A_0}t\right)^{-3}$$

Based on the Taylor series expansion, the expression of filtrate volume when t→0 for the standard blocking model, V_s is given by;

$$V_S \cong V_0 t - 2V_0\left(\frac{k_S V_0}{A_0}\right)\frac{t^2}{2!} = V_0 t - V_0\left(\frac{k_S V_0}{A_0}\right)t^2 \qquad \text{Equation 4.13}$$

Given the membrane maximum volumetric capacity for standard blocking model as $V_{max,s}$;

$$V_{\max,s} = \frac{A_0}{k_s} \qquad \text{Equation 4.14}$$

By introducing Equation 4.4 into Equation 4.3, the expression of V_s can be written as;

$$V_S \cong V_0 t\left(1-\left(\frac{k_S V_0}{A_0}\right)t\right) = V_0 t\left(1-\frac{V_0}{V_{\max,S}}t\right) \qquad \text{Equation 4.15}$$

For the intermediate blocking model, the expression is:

$$V = \frac{1}{k_i}\ln\left(1+k_i V_0 t\right) \qquad \text{Equation 4.16}$$

The first and second derivatives of the intermediate blocking model can be written as:

$$V' = \frac{1}{k_i}\left(k_i V_0\right)\left(1+k_i V_0 t\right)^{-1} = V_0\left(1+k_i V_0 t\right)^{-1}$$

$$V'' = -V_0(k_i V_0)(1 + k_i V_0 t)^{-2}$$

Based on the Taylor series expansion, the expression of filtrate volume when t→0, V_I is given by;

$$V(0) = 0; V'(0) = V_0; V''(0) = -k_i V_0^2$$

$$V_i \cong V_0 t - k_i V_0^2 t^2 / 2 \qquad \text{Equation 4.17}$$

The equation of the complete blocking model is given by:

$$V = \frac{V_0}{k_b}\left[1 - \exp(-k_b t)\right] \qquad \text{Equation 4.18}$$

The first and second derivatives of the complete blocking model can be written as:

$$V' = V_0 \exp(-k_b t)$$
$$V'' = -k_b V_0 \exp(-k_b t)$$

Based on the Taylor series expansion, the expression of filtrate volume when t→0, V_b is given by;

$$V(0) = 0; V'(0) = V_0; V''(0) = -k_b V_0$$

$$V_b \cong V_0 t - k_b V_0 t^2 / 2 \qquad \text{Equation 4.19}$$

Given the membrane maximum volumetric capacity for the complete blocking model as $V_{max,B}$;

$$V_{max,b} = \frac{V_0}{k_b} \qquad \text{Equation 4.20}$$

By introducing Equation 4.20 into Equation 4.19, the expression of V_B can be written as;

$$V_B \cong V_0 t(1 - k_b t/2) = V_0 t\left(1 - \frac{1}{2}\frac{V_0}{V_{\max b}} t\right) \qquad \text{Equation 4.21}$$

The comparison of Equation 4.15, Equation 4.17 and Equation 4.21 shows that the short time behaviour of standard, intermediate and complete models when time, t very close to zero is identical where;

$$\lim_{t \to 0} V \cong V_0 t \qquad \text{Equation 4.22}$$

The mathematical analyses of the filtration blocking models can be related to observations in the filtration of pQR150 (20 kb) and pGEc47 (56 kb) at 5 and 8 transmembrane pressures, which is during early time of filtration, all models behaved in an identical way and its start to deviate when the values of time, t increase.

4.3.3 ***Analysis of fouling using combined fouling models***

The test results suggested that the fouling mechanism of large plasmid DNA was not governed by a single fouling mechanism as described by the classical blocking models. Therefore, we tested the filtration data with the combined blocking models as described by Bolton et al. (2006): These authors discovered that the application of combination of these classical models in sterile filtration of Immunoglobin G (IgG) and virus filtration of bovine serum albumin (BSA) lead to a better fit of the experimental data (Bolton et al., 2006). The idea is to combine the classical blocking models (i.e. combination of standard and intermediate models) and determine if a transition of fouling mechanisms exists during filtration. Originally, five combined blocking models were proposed: complete-standard, intermediate-standard, cake-standard, cake-intermediate and cake-complete models. The selection of candidate of combined blocking models was based on the goodness of fit of the classical models. Moreover, the last three models were ignored because of the rarity of cake build-up during sterile filtration. Thus two combined blocking models, the intermediate-standard and complete-standard models were considered to determine whether these models can explain the fouling mechanism of the filtration of pQR150 (20 kb) and pGEc47 (56 kb) plasmids DNA. Figure 4.2 shows the experimental results of the filtration test of pQR150 (20 kb) and pGEc47 (56 kb) at 8 psi

transmembrane pressure and the corresponding best-fit lines for the two combined models. A similar trend is observed with the other filtration tests. The best fit of data occurred with the combined intermediate-standard model for filtration of pGEc47 (56 kb) at 8 psi. This is confirmed by the lower values of standard error of estimate obtained for the intermediate-standard model compared with the complete-standard model (see Table 4.6).

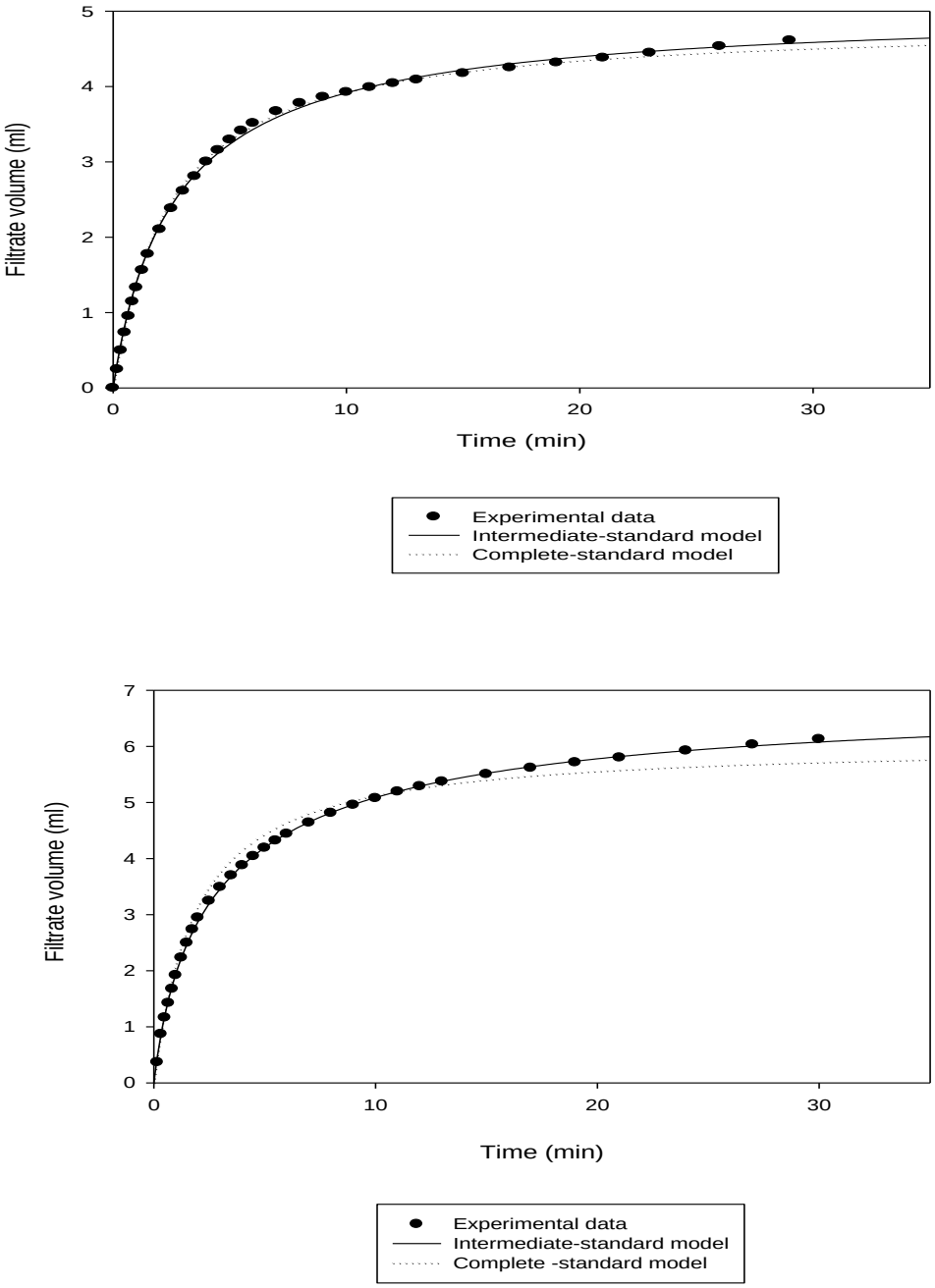

Figure 4.2 - Experimental data of filtrate volume vs. time fitted with the intermediate-standard and complete-standard filtration blocking models. Plasmid solution containing 50 µg/ml of pQR150 (20 kb) (top) and pGEc47 (56 kb) (bottom) were filtered at 8 psi transmembrane pressure through 0.22 µm PVDF membrane.

Table 4.6 - The model fit errors of the filtration of pQR150 and pGEc47 at 5 and 8 psi transmembrane pressure.

Plasmid	Model	Standard error of estimates 5 psi transmembrane pressure	Standard error of estimates 8 psi transmembrane pressure
pQR150	Intermediate-standard	0.077	0.061
	Complete-standard	0.331	0.080
pGEc47	Intermediate-standard	0.035	0.165
	Complete-standard	0.194	0.348

As shown in Table 4.6, the intermediate-standard model is the best model that described the fouling phenomena during filtration of pQR150 (20 kb) and pGEc47 (56 kb) plasmids. These results suggest that the fouling process cannot be described as a single mechanism but as a combination of multiple fouling mechanisms. However, analysis of the goodness of fit using standard error of estimate only represents a basic indicator of the fouling phenomena during filtration. In order to obtain a better understanding of the process of fouling, mathematical analysis has been performed to investigate the transition of fouling mechanisms. In the subsequent analysis, the mechanism of the transition of these models during the filtration was analyzed.

4.3.4 ***Analysis of fouling transition during filtration of plasmid DNA***

Figure 4.3 illustrates the transition of fouling mechanism during 8 psi transmembrane pressure filtration of pQR150 (20 kb) and pGEc47 (56 kb). A similar trend was observed during the filtration of both plasmids at 5 psi. The transition of the average value of *n* that describes the fouling behaviour during early, mid and late time of filtration is extracted from these plots. Figure 4.4 is the simpler form of Figure 4.3, which contains information on the dominant fouling mechanism at a specific time during filtration.

The common features of all the results suggest that at early time of filtration, the exponent *n* originated from a value that is close to 1. These results imply that during this stage, the intermediate blocking model dominated the fouling which describes that the plasmids were retained on the surface of the membrane. Later on, the values of n seem to approach *n* ~1.5 asymptotically. This value suggests that the fouling dominated by the standard blocking model where the internal fouling occurred within the depth of the filter.

Figure 4.4 shows that during the filtration at 8 psi, the transition of the value of *n* (from low to high *n* values) occurred earlier (at low *dt/dV*) for pQR150 (20 kb) than pGEc47 (56 kb). This is expected since the smaller size of pQR150 (20 kb) allows the plasmid to penetrate the membrane more efficiently.

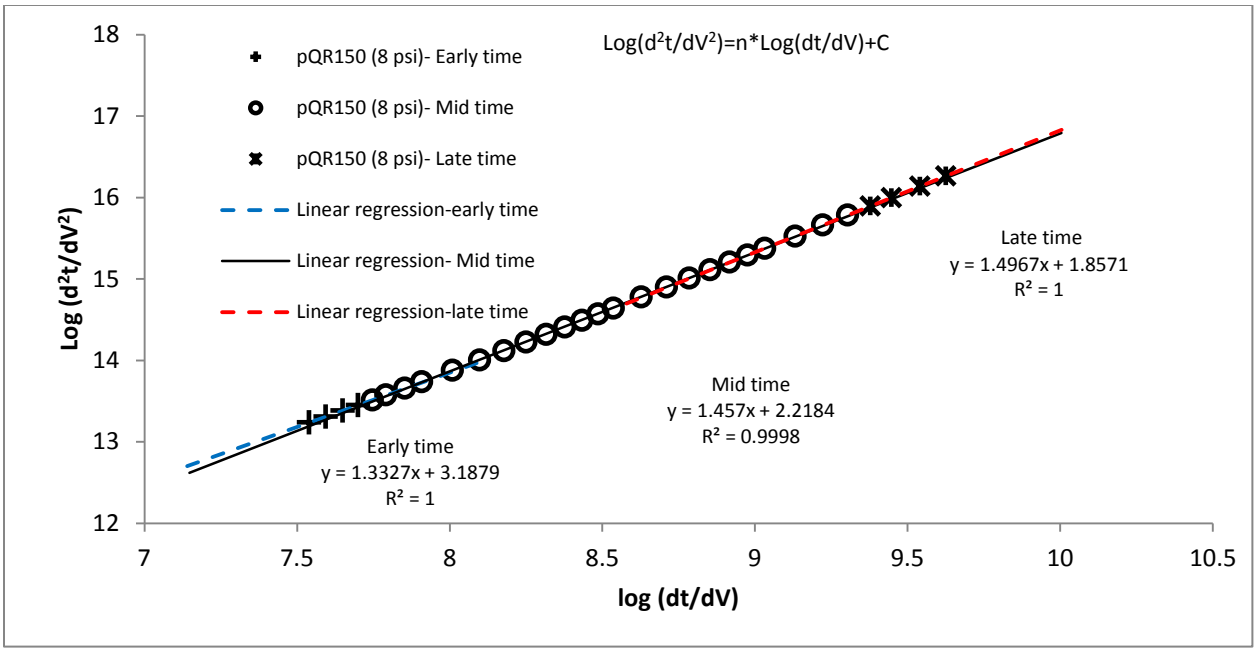

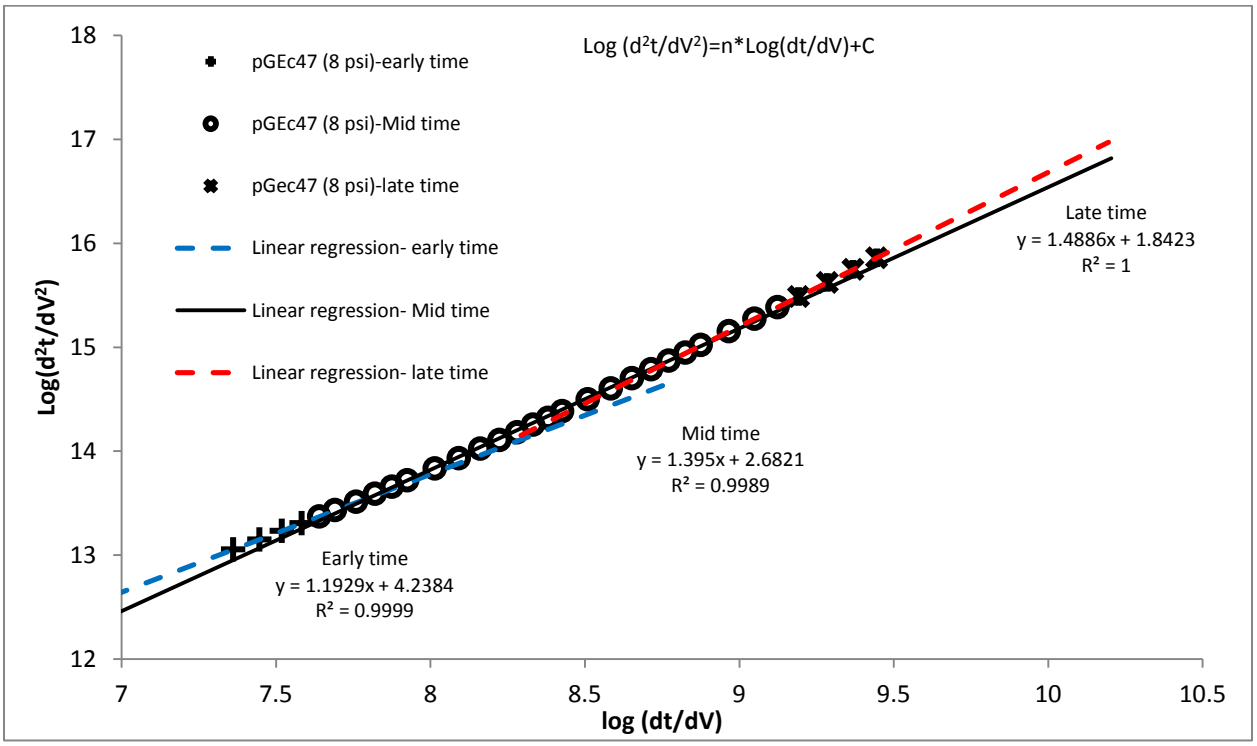

Figure 4.3 - Flux decline analysis of pQR150 (20 kb) (top) and pGEc47 (56 kb) (bottom) filtrations at 8 psi transmembrane pressure

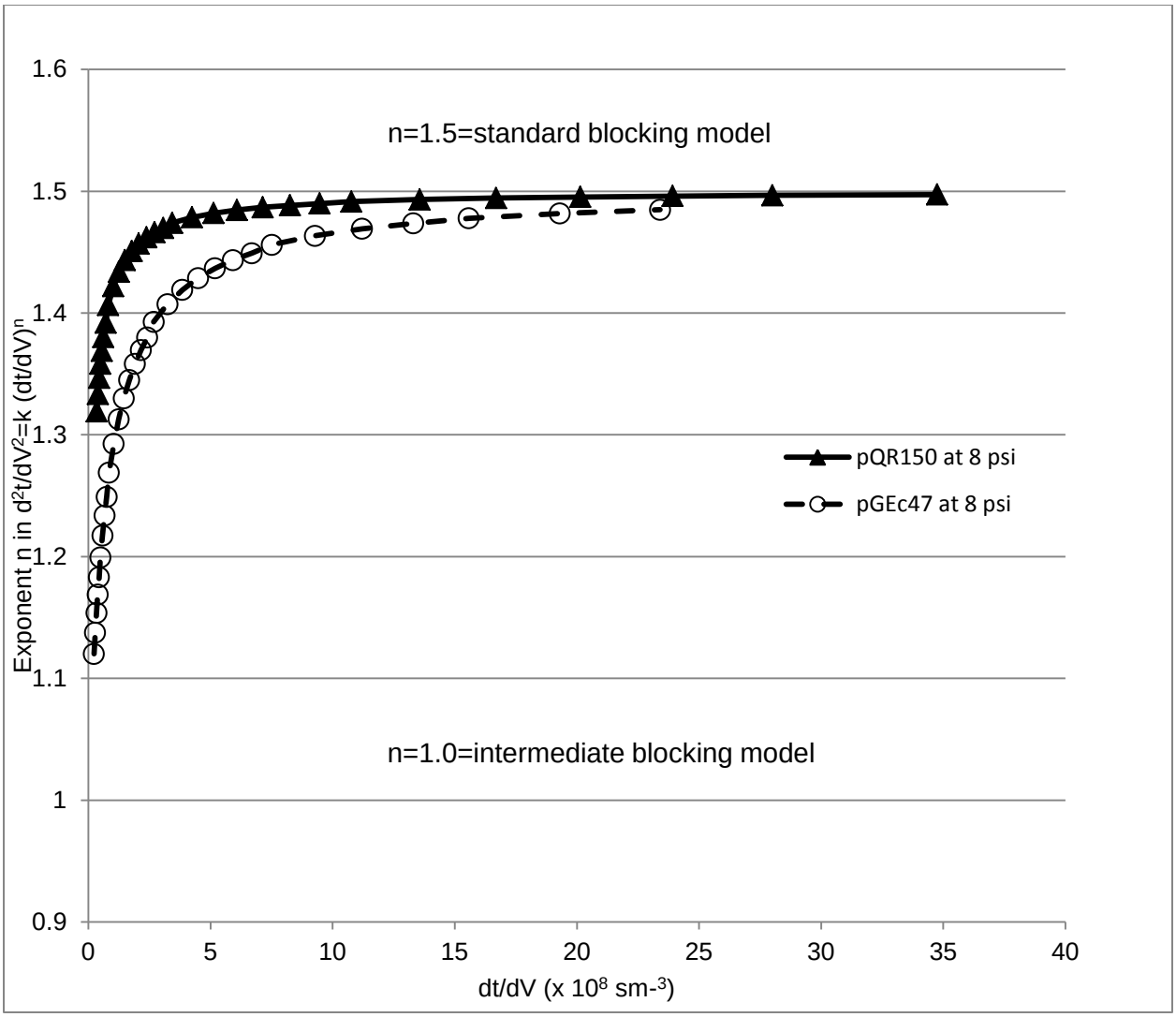

Figure 4.4 - The plot of exponent n (Equation 4.1) vs. *dt/dV* of the filtration of pQR150 (20 kb) and pGEc47 (56 kb) at 8 psi transmembrane pressure.

The filtration behaviour of DNA is different from proteins and other particulates since DNA is a flexible long chain molecule. These characteristics allow DNA to penetrate the pores and elongate during its trajectory throughout the membrane. Furthermore, large DNA molecules with radii of gyration that is larger than the nominal pore size can potentially be retained inside the interstitial pore structure. It is possible that during the trajectory, entrapment occurs at the surface of the pore and at the same time the other parts of a plasmid penetrate along the web of the other pores. In contrast, proteins and particulates are always modelled as rigid and sphere-shape molecule (Kim and Zydney, 2005). These physical properties influence the retention mechanism during filtration and can be assessed by the value of n in log d^2t/dV^2 vs. log dt/dV.

The interesting feature of the present results is the transformation of the values of *n* contrasts with results observed during the microfiltration of particulate suspensions; such as filtration of bovine serum albumin (BSA). BSA is a type of protein with a diameter typically smaller than the nominal size of pores in microfiltration membranes (Tracey and Davis, 1994). Retention of BSA was observed inside the inner wall of the pore and could be characterized using the standard blocking model (Bowen and Gan, 1991). Other work has also shown that the fouling of BSA aggregates occurred on the surface of the membrane (Kelly et al., 1993). Iritani and co-workers (1995) reported during the filtration of BSA through 0.05 µm nitrocellulose membrane, the values of *n* were maximum at the initial stage of filtration (low *dt/dV*) and decreased to 0 as the cake occurred at the end of filtration.

Interestingly, during the filtration of pQR150 (20 kb) and pGEc47 (56 kb) plasmids, the values of *n* increased with the increase of *dt/dV* until it approached an asymptote around 1.5 that represents the standard blocking mechanism. The value of *n* at the early time of filtration is close to 1; indicating the intermediate blocking model dominated the fouling mechanism at this stage. The results suggested that at the beginning of the filtration, plasmids DNA were trapped as its chain-like molecule did not align with the surface of the membrane. It is also thought that the trajectory and orientation of plasmids is initially parallel with the surface of the filter. However, since plasmids are flexible, the molecule can realign its structure to penetrate the pore with the assistance of shear stress originated from flow of the solution inside the membrane (Hirasaki et al., 1995).

4.3.5 ***Impact of fouling on transmission of plasmids DNA***

Figure 4.5 and Figure 4.6 describe the relationship between the dominant fouling mechanisms and the plasmid transmission. The values of exponent *n* in Figure 4.4 were re-plotted in term of accumulated filtrate volume to simplify the analysis of fouling behaviour. This analysis is an attempt to correlate the mathematical analysis; which is applied to calculate the values of *n,* with the plasmid transmission data collected in the laboratory.

The transmission of both plasmids was high; >80 % during the filtration of the first 3.5 and 5.0 ml of filtrates for pQR150 (20 kb) and pGEc47 (56 kb) respectively (Figure 4.5 (top) and Figure 4.6 (top)). However, a significant reduction of plasmid transmission was observed afterwards, with considerable differences for the filtration of pQR150 (20 kb) at 5 psi. The results also suggest that higher pressure filtration (at 8 psi) slightly increased the transmission of plasmids compared with the filtration operated at 5 psi before the significant drop of the transmission occurred. The observation is supported by the analysis by Hirasaki et al (1995) that showed that the increase in transmembrane pressure assisted the penetration of plasmid molecules into the pore.

However, the operation at 8 psi increased the rate of fouling by increasing the flux towards the membrane. This is observed by the rapid decline of filtrate flux during filtration at 8 psi compared with the filtration at 5 psi transmembrane pressure (see Figures 4.5a and 4.6b).

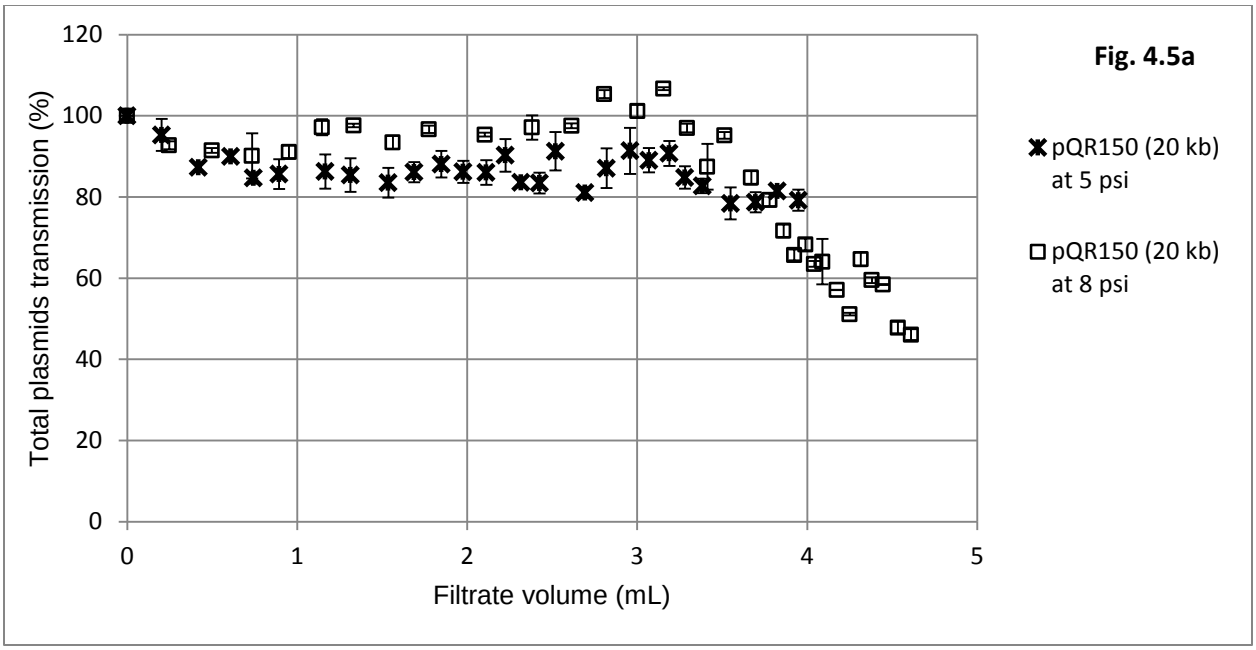

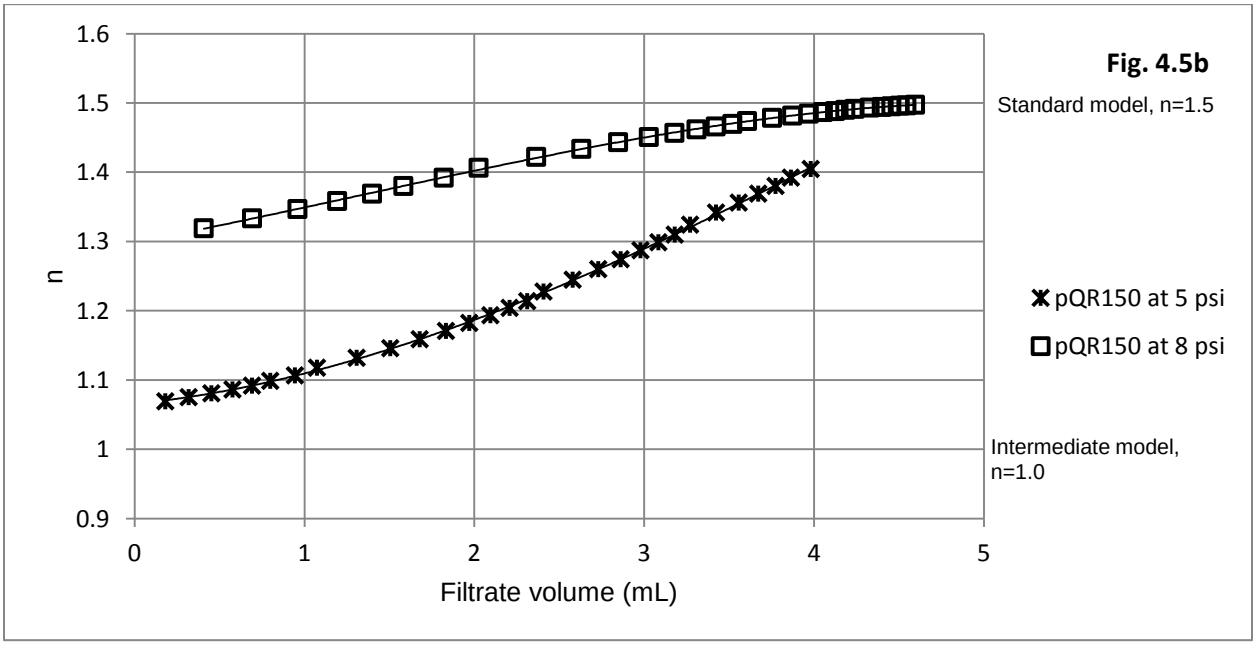

Figure 4.5- The transmission of pQR150 (20 kb) through 0.22 µm PVDF membranes at 5 and 8 psi constant pressure filtration. The plasmid DNA was collected in batches and the total transmission was determined by the ratio of concentration of filtrate to the concentration of feed. Error bars indicate the standard deviation (n=3).

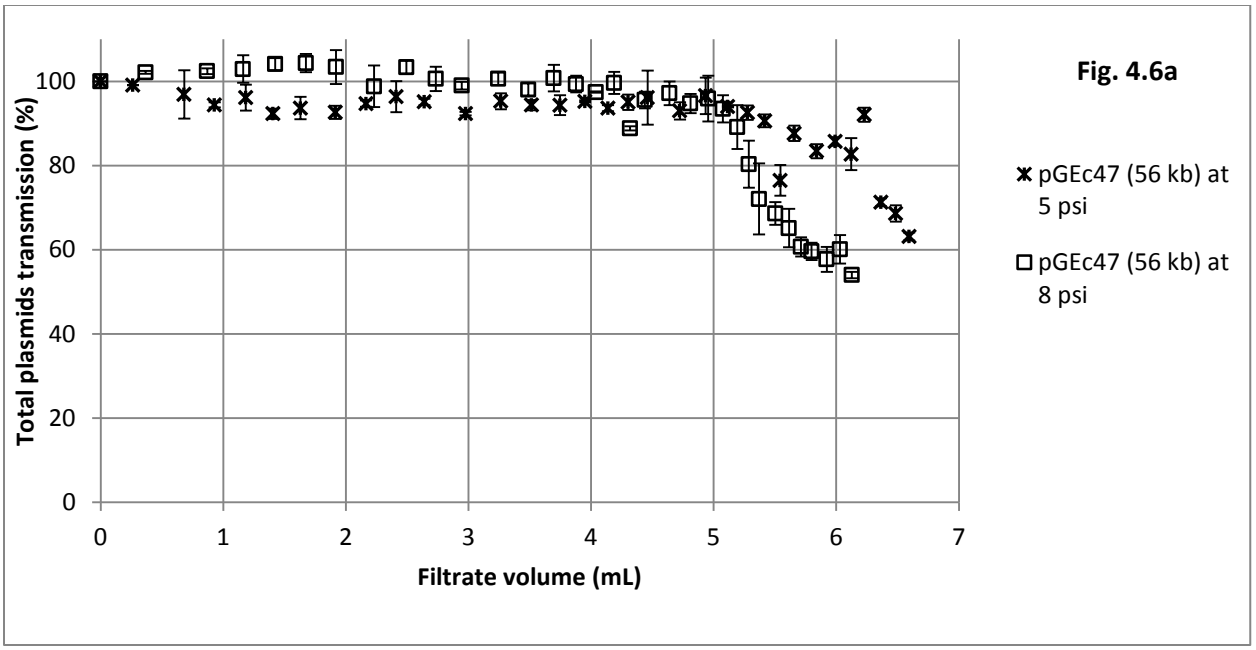

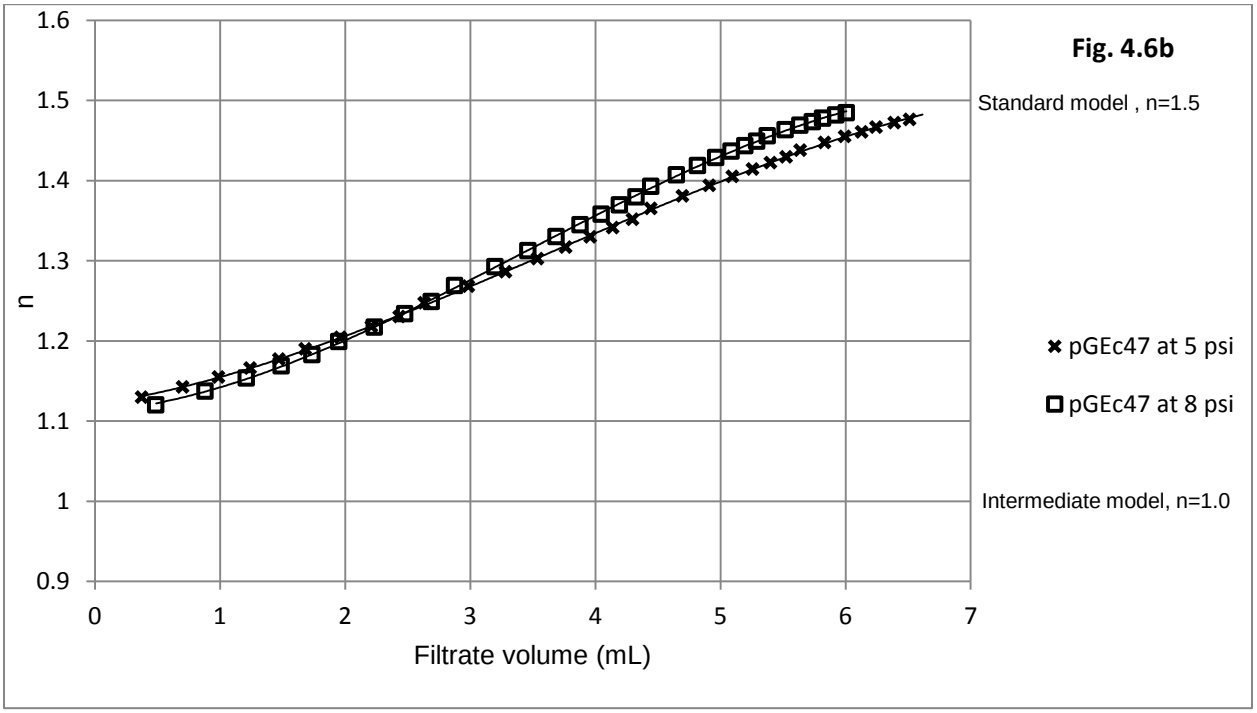

Figure 4.6- The transmission of pGEc47 (56 kb) through 0.22 µm PVDF membranes at 5 and 8 psi constant pressure filtration. The plasmid DNA was collected in batches and the total transmission was determined by the ratio of concentration of filtrate to the concentration of feed. Error bars indicate the standard deviation (n=3).

The significant decrease of plasmid DNA transmission after a specific time correlates with the changes of the value of exponent *n* of d^2t/dV^2 vs. dt/dV plots. During the filtration of pQR150 at 8 psi, the transmission began to drop (after filtering ~3.7 ml filtrates) at the point where the values of n= 1.48 which indicates that the blocking mechanism tends to the standard blocking model (Figure 4.5). The results suggested that at this point, internal fouling started to dominate the filtration and influenced the reduction of internal pore diameters and consequently reduced the transmission of plasmids.

Similar trends were observed during the filtration of pGEc47 at 5 and 8 psi (Figure 4.6). The reduction of plasmid transmission can be correlated with the values of *n* in d^2t/dV^2 vs. dt/dV plot. During the time when the transmission started to drop at 5 and 8 psi filtration, the values of n were detected at ~1.43 and ~1.44 respectively. Again, the significant reduction of plasmids transmission correlated with the values of *n* approaching 1.5.

It is interesting to note that the transmission of plasmid DNA reduced significantly when the pore constriction blocking mechanism (standard model) dominated the fouling of the membrane. During the initial stage of filtration when the fouling was dominated by the intermediate blocking mechanism, the blockage was caused by the superposition of plasmids that are trapped on the surface of membrane. However, the transmission of plasmids began to decrease dramatically when the pore constriction mechanism started to dominate the fouling. At this stage, the reduction of pore size due to the internal fouling influenced the flexibility and ability of plasmids to penetrate the pore.

The constriction of the internal pore structure would reduce the available space for plasmid trajectory. Plasmid is a negatively charge molecule and at high fluid concentration; when the space between plasmid molecules is reduced, electrostatic repulsion between molecules increased. The repulsion increased the rigidity of plasmids and influenced its trajectory through the membrane. During the initial stage of filtration when high transmission of plasmids was observed, high magnitude of the shear and elongational stresses provided by high transmembrane pressure (at 8 psi) overcame the electrostatic repulsion and consequently increased the flexibility of the plasmid. High flexibility of plasmid assists the penetration of this molecule into pores. This hypothesis is in agreement with the transmission data of pQR150 (20 kb) and pGEc47 (56 kb) plasmids where the transmission was higher at 8 psi compared with 5 psi transmembrane pressure during the initial stage of filtration. In contrast, low transmembrane

pressure encouraged the retention of DNA at the surface of the membrane. This is probably due to low velocity magnitude that gives rise to a slower trajectory of plasmids which leading to the entrapment of these molecules inside the membrane.

4.4 **Conclusions**

Interestingly, the combined intermediate-standard model can be applied to describe the flux decline behaviour of the filtration of large plasmids DNA even though the model was originally developed to explain the filtration behaviour of rigid spherical particles. This work has demonstrated that the model can also play a practical role in explaining the fouling behaviour inside a polymeric membrane that contains complex interconnected pores in contrast with the assumption of the model that describes the membrane as parallel arrays of cylindrical pores.

During the filtration of both pQR150 and pGEc47 plasmids at 5 and 8 psi transmembrane pressures, it was found that the intermediate blocking model dominated the fouling during short initial filtration period (except for filtration of pQR150 at 5 psi). The standard blocking mechanism subsequently dominated the fouling for the remainder of the filtration.

A good correlation was observed between the reduction of plasmid transmission and the value of n in Equation 4.1. The transmission of plasmids dropped significantly at the point when n~1.5 during the filtration at higher transmembrane pressure (at 8 psi compared with filtration at 5 psi). It is thought that high transmembrane pressure influenced the retention of plasmid by capturing this molecule inside the membrane. Low transmembrane pressure assisted the penetration of plasmids by allowing the molecule to align and thus penetrate the pores. It is also interesting to note that the decrease of plasmid transmission is due to the internal fouling as suggested in d^2t/dV^2 *vs.* dt/dV plots.

5 Application of computational fluid dynamics (CFD) to characterise fluid flow regimes in normal flow filtration- An analysis of the impact of fluid flow on the loss of plasmid DNA

5.1 Introduction

Fluid stress during membrane filtration causes breakage of the phosphodiester bond between bases in the double-helical structure of DNA (Lengsfeld and Anchordoquy, 2002). The changing of plasmid DNA topology from supercoiled (SC) to open circular (OC) and linear DNA, due to the breakage of this chemical bond is undesirable since it causes the loss of encoded genetic information accordingly reducing the optimum biological activity of the DNA employed in gene therapy and DNA vaccination. The degraded isoforms (OC and linear) are structurally less compact in term of its conformation which affects the delivery of a DNA vaccine into the targeted cells. In addition, the requirement set up by regulatory bodies demanded the plasmid DNA to be in a characterised and single isoform. Therefore, it is a priority to preserve the SC plasmid integrity.

During sterilising filtration of SC plasmid DNA, it is suspected that the sources of DNA loss are from 1) the retention of plasmids on the surface and inside the membrane 2) the degradation of SC plasmid topology to open circular (OC) and linear forms (Kong et al., 2010). Previous chapters discuss the loss of plasmid through retention and fouling. In this chapter, the investigation is focused on the impact of fluid stresses to the degradation of the supercoiled plasmid molecule.

Plasmid DNA, especially > 20 kb plasmids is susceptible to fluid stresses. The degradation of plasmid has been observed in unit operations such as in cell lysis (Levy et al., 1999a), membrane filtration (Kong et al., 2006), centrifugation (Levy et al., 1999b) and nebulisation (Arulmuthu et al., 2007). These studies and clinical trials that involved DNA vaccination and gene therapy employed small plasmid DNA (less than 20 kb).

The effect of fluid stresses to the 20 kb plasmid is investigated. The primary concern is whether this molecule degrades due to fluid stress during the filtration. The main objective of this study is to develop methods and approaches to characterise the fluid flow regimes throughout the progression of fouling during normal flow filtration. Secondly, the correlation of these parameters with plasmid DNA degradation is attempted. Computational fluid dynamics (CFD) is applied to characterise the fluid flows inside the membrane.

The Brinkman equation was applied to estimate the velocity magnitude and strain rate inside the membrane. The simulation was implemented using the finite element analysis package (Comsol Multiphysics) for the simplified geometry of a commercial syringe filter unit. This provides the macro-scale flow distribution and average values of fluid velocity and strain rates that are hypothesized to affect the quality of SC plasmid DNA.

However, at micro-scale, the tortuosity of the pore network inside the membrane contributes to a very complex local distribution of velocity and strain rates. Observations using transmission electron microscopy suggests that a polymeric membrane contains a broad range of pore diameters. This factor contributes to the range of strain rate magnitudes since the strain rate depends on the diameter of the pore. The simulation of fluid flow inside the actual pore structure was obtained by developing an ‘image to simulation workflow’. The membrane geometry was acquired by transmission electron microscopy (TEM). The geometry was then used as a template for a computational fluid dynamics simulation. Furthermore, the correlation between shear and elongation strain rates obtained from the computational fluid dynamics simulation and the SC content throughout the filtration is analysed. The overall objective is to understand the magnitude of strain rates inside the membrane that is responsible for the degradation of 20 kb plasmid DNA.

Figure 5.1 indicated the workflow of the fluid flow simulations in this chapter:

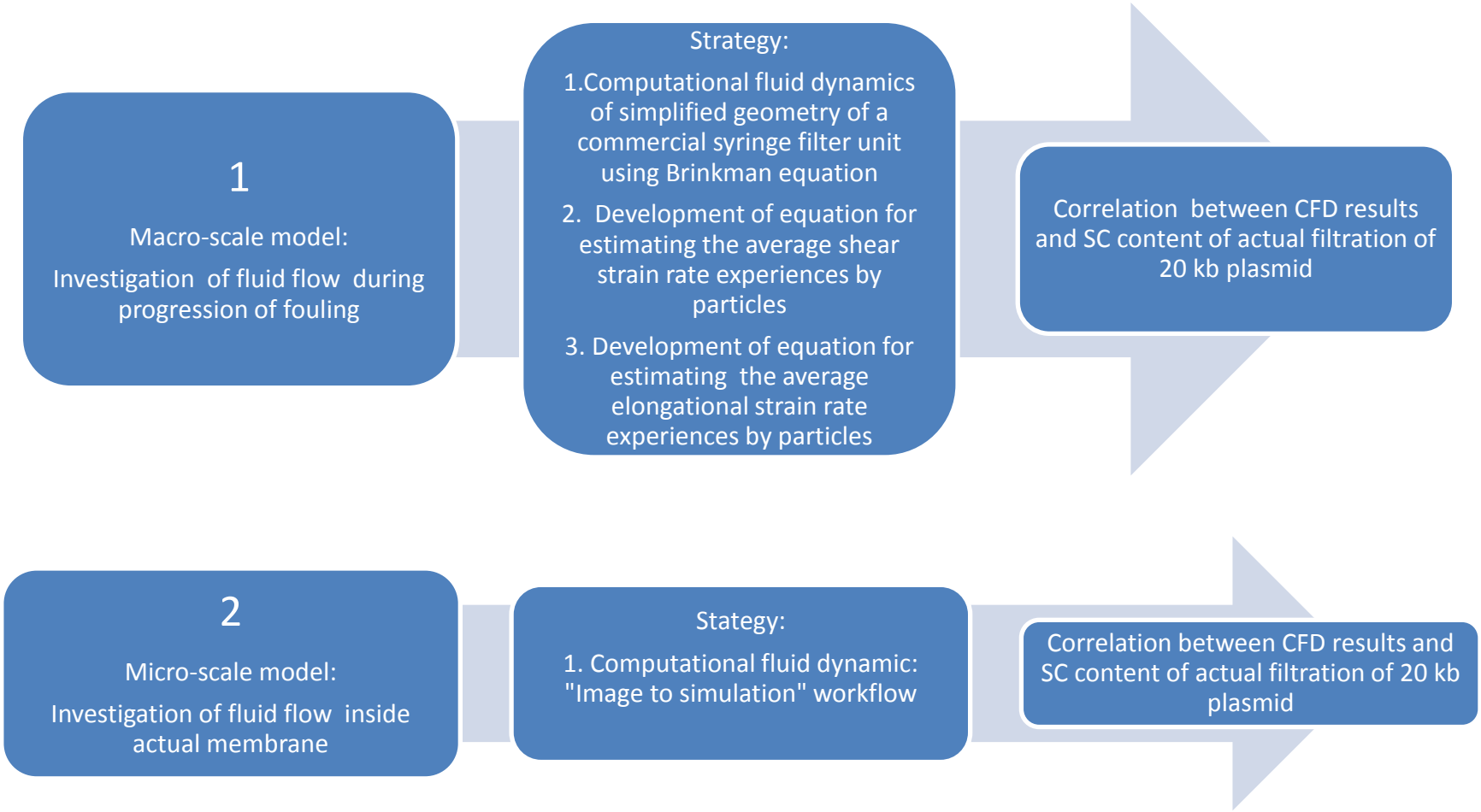

Figure 5.1-The approaches to investigate the fluid flow regimes inside sterile filtration membrane and how it impact on the degradation of SC plasmid DNA

5.2 **Theoretical development**

5.2.1 ***Numerical simulation to estimate the average elongation strain rate during progression of fouling***

The simulation was based on the filtration of pQR150 (20 kb) plasmid DNA at 5 and 8 psi transmembrane pressures. The model geometry was a simplified form of a commercial syringe filter unit; sterilising grade 13-mm Millex^{TM} 0.22 µm Durapore® polyvinylidene difluoride (PVDF) capsule (Figure 5.2). The filter unit was divided into three regions (a. b and c). The 'a' and 'c' regions represent the fluid domain and the 'b' region represents the membrane/porous domain (Figure 5.3).

Figure 5.2- The commercial syringe filter unit (13 mm diameter) was used as the basis for the simplified geometry model in Figure 5.3.

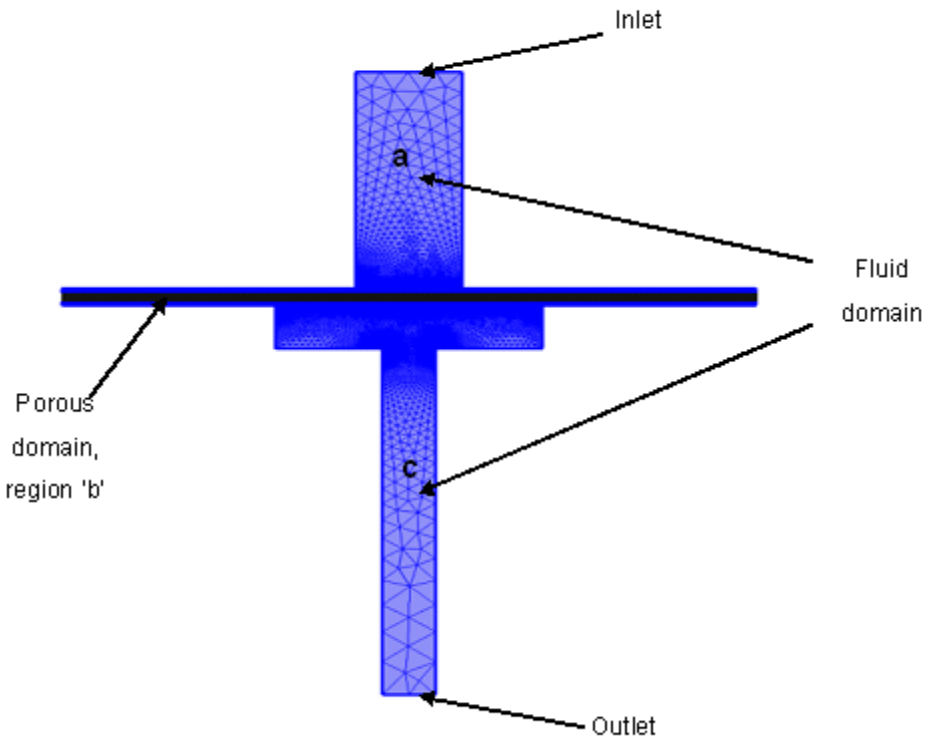

Figure 5.3- A simplified meshed geometry of Figure 5.2. This geometry was used as the model geometry for the computational fluid dynamic simulation.

Note that the simplification has been made in term of the housing of the filter. The actual syringe filter unit might contain additional features such as porous support screen and under-drain structure. It is assumed that the support screen has minimal interference effect in terms of pressure drop and resistance to flow. In this simulation, this effect is ignored. The optimised under-drain structure resulted in the minimal energy dissipation rate at the under-drain structure and enables the uniform pressure distribution inside the syringe filter. However, in this experiment, it is assumed that the pressure drop throughout the membrane is similar with the pressure drop of the syringe filter unit.

The flow inside the fluid and porous domains (Figure 5.3) is governed by the Navier-Stokes and the Brinkman equations respectively. By assuming the fluid's density to be constant, the incompressible Navier-Stokes equation can be applied for simulation of flow inside the fluid domain:

$$\rho\left(\frac{\partial u}{\partial t}+u.\nabla u\right)=-\nabla p+\mu\nabla^2 u$$

$$\nabla.u=0$$

Equation 5.1

Where ρ represents fluid density (kg/m^3), p is pressure (Pa), μ is the fluid viscosity (Pa.s) and u is the velocity magnitude (m/s).

The Brinkman equation describes the momentum transport of fluid in a porous media. The equation is the extension of Darcy's law that includes the impact of shear stress to the momentum transport of fluid. However, in this equation, the flow variables and fluid properties at any point in the control volume are the average of actual variables and properties inside the actual membrane. The flow velocity given by the simulation is defined as the superficial velocity, corresponding to the volume of flow rate per unit cross section of the membrane. The equation below describes the Brinkman equation:

$$\frac{\rho}{\phi}\left(\frac{\partial u}{\partial t}+(u..\nabla)\frac{u}{\phi}\right)=-\nabla p+\nabla\left(\frac{1}{\phi}\left\{\mu(\nabla u+(\nabla u)^T)-\frac{2}{3}\mu(\nabla u)I\right\}\right)-(\frac{\mu}{k}+Q_{Br})u$$

$$\rho\nabla.u=Q_{Br}$$

Equation 5.2

Where k represents membrane permeability (m^2) and Φ is the porosity of membrane. Q_{Br} is the other force. Since the Brinkman equation includes the porosity and permeability as the independent variables, the equation can be manipulated to characterise the magnitude of the flow profiles during the progression of fouling. In this simulation, it is assumed that the porosity is uniform throughout the membrane on the basis that the membrane is symmetric.

The inlet boundary of the model was set to 5 and 8 psi, respectively, and the outlet boundary was set to zero corresponding to the two values of transmembrane pressures used during the constant pressure filtration experiments. Other boundaries; such as the wall of the filter housing was set as no slip condition where the fluid's velocity equals that of the boundary which is, u=0.

A free triangular mesh was then inserted into the geometry. The maximum size of $1e^{-5}$ m and $9.65e^{-4}$ m meshes were inserted in porous media and fluid domain respectively. The simulation was then solved using a stationary step solver.

The transmembrane pressure, permeability and porosity were the input values of the simulation. The permeability, *k* and porosity, Φ of membrane was determined from the experimental filtrate flux data using Equation 5.3 and Equation 5.4:

$$k = \frac{J_v \mu \ell}{\Delta P} \qquad \text{Equation 5.3}$$

$$\phi = \frac{8 J_v \mu \ell \tau}{\Delta p r^2} \qquad \text{Equation 5.4}$$

Equation 5.3 and Equation 5.4 are the Darcy's law and Hagen-Poiseuille equations respectively. J_v represents the filtrate flux (m/s), *r* is the radius of the pore (m), ℓ is the thickness of the membrane (m) and τ is the tortuosity factor.

The CFD simulation using the Brinkman equation provides the superficial velocity, *u* and to calculate the average velocity inside a pore, v_{pore} the continuity equation was applied where;

$$\begin{aligned} u.A_{total} &= v_{pore} A_{fluid} \\ v_{pore} &= u.\left(\frac{A_{total}}{A_{fluid}}\right) \\ v_{pore} &= \frac{u}{\phi} \end{aligned} \qquad \text{Equation 5.5}$$

5.2.2 ***Estimation of the average elongation strain rate experienced by plasmids particles***

To assess the impact of the strain rate on the degradation of supercoiled plasmid DNA, the elongational strain rate, ε inside the membrane was calculated using equation;

$$\varepsilon = \frac{V_{pore}}{d}.C \qquad \text{Equation 5.6}$$

Where V_{pore} is the average pore's velocity (m/s), d is the diameter of the pore (m) and C is a constant. During filtration, the fouling of the membrane occurs and it decreases the diameter of the pore (d). The decrease of the pore size is estimated by the other form of the Hagen-Poiseuille equation;

$$r_p = \sqrt[4]{\frac{8J_v\mu\ell}{\pi.\Delta p\ n_p}} \qquad \text{Equation 5.7}$$

Where Δp is the transmembrane pressure (Pa), μ is the viscosity of the solution (Pa.s), ℓ is the depth of the filter (m) and n_p is the number of pores per unit area ($1/m^2$). Since the pore structure in the membrane was not the ideal straight tube-like pore, the length of the pore was multiplied with a tortuosity factor. The tortuosity factor, τ_f was calculated by;

$$\tau_f = \Delta p_{actual} / \Delta p_{hp} \qquad \text{Equation 5.8}$$

The transmembrane pressure of the actual membrane, Δp_{actual} was the pressure drop during the actual experiment and the Δp_{hp} is the pressure drop calculated using the Hagen-Poiseuille equation based on the filtrate flux and the pore size of a clean membrane. The pore size was estimated based on manufacturer's data.

The estimation of the decrease of the pore diameter can be estimated by adding the tortuosity factor in Equation 5.7;

$$r_p = \sqrt[4]{\frac{8J_v \mu \ell \tau_f}{\pi . \Delta p n_p}} \qquad \text{Equation 5.9}$$

In order to estimate the value for the average elongation strain rate experienced by the plasmid (using Equation 5.6), the approximation of the constant *C* in the equation need to be determined. The constant is the function of the flow path inside the pore geometry taken by the plasmid molecules. The value of *C* is ~8 for the elongation strain rate detected very close to the pore wall. On the other hand C = 0 on the centre line, where the elongational strain rate equals zero. The average of these two values (C = 4) suggests itself as an approximate value. However, there is proportionately more area near the pore wall than around the centre line of pore.

The radius increment, *dr* at radius, *r* of a pore is associated with the elemental area $dA = 2\pi r.dr$. So for a given *dr*, the elemental area increases linearly with radius *r* due to the factor $2\pi r$. Since there is proportionately more area near the pore wall, the factor *C* should be weighted more towards the elongation strain rate that is experienced in fluid near the pore wall, i.e. *C* should be closer to 8. Furthermore, we should also take into account that the no-slip condition slows down fluid near the wall hence more of the particles will have passed through the region near the centre line of the pore, due to relatively higher velocity magnitude. If the particles were uniformly distributed across the pore, more particles would pass through the region near the centre line of the pore hence *C* should be closer to zero as a consequence of this effect.

An appropriate value of *C* is now estimated by finding the number-weighted average elongation strain rate during plasmid particle trajectories through a cylindrical pore assuming that the laminar Hagen-Poiseuille flow prevails. For analysis, the pore's cross section is sub-divided in i=N number of regions each with a constant equal shear strain rate, γ_i. The average shear strain rate that is experienced by the particles, n_i that pass through each region, i is given by:

$$\bar{\gamma} = \frac{\sum_{i=1}^{N} n_i \gamma_i}{\sum_{i=1}^{N} n_i}$$ Equation 5.10

The product of the number of particles per second that pass through an infinitesimal area of *dA* is equal to the product of number density ρ_n (particles/m^3) and the elemental flow rate (*dQ*):

$$\rho_n . dQ = \rho_n . v . dA$$ Equation 5.11

Since the particles are uniformly distributed throughout the entrance of the pore, the value of ρ_n does not change for different elemental areas (i.e. ρ_n is not a function of the radius of pore), so the total number of particles collected per second, *P* (particles/s) in the filtrate is equal to the product of number density of ρ_n multiplied by *Q*:

$$P = \rho_n . \int_A dQ = \rho_n . Q = \rho_n . \pi R^2 V$$ Equation 5.12

Where *R* is the radius of pore (m) and *V* is the average velocity (m/s).

The numerator in Equation 5.10 is the shear strain rate weighted by the number of particles and is obtained by multiplying the local strain rate with the number of particles in a given elemental area and summing the resulting product over all cross-sectional area elements of the pore. The integration of the infinitesimal area elements can be expressed in the equation below and represented by Γ:

$$\Gamma = \int_A \gamma \rho_n dQ$$ Equation 5.13

The local shear strain rate γ (1/s) at radius *r* for Hagen-Poiseuille flow through a cylindrical pore is given by:

$$\gamma = \gamma_w \frac{r}{R} = \left(8 \frac{V}{D}\right) \frac{r}{R}$$ Equation 5.14

where γ_w is the wall shear rate. The expression evaluates the sum of strain rates γ weighted by the number of particles in the filtrate that experienced the strain rate.

The volume flow rate, *Q* can be calculated by integrating the velocity distribution:

$$Q = \int_A dQ = \int_A v dA \qquad \text{Equation 5.15}$$

The elemental volume flow rate is given by;

$$dQ = v.2\pi r.dr \qquad \text{Equation 5.16}$$

and the local velocity expression, *v* is given by the equation of parabolic velocity profile in Hagen-Poiseuille flow:

$$v = v(r) = 2V\left(1 - \frac{r^2}{R^2}\right) \qquad \text{Equation 5.17}$$

By inserting the Equation 5.11 Equation 5.14 into expression in Equation 5.12, and also by replacing the local velocity by expression Equation 5.17, the expression of Γ can be evaluated as:

$$\Gamma = \int_A \gamma \rho_n dQ = \rho_n \int_A \gamma dQ = \rho_n \int_{r=0}^{r=R} 8\frac{V}{D}\left(\frac{r}{R}\right).2V\left[1-\left(\frac{r}{R}\right)^2\right].2\pi r dr = \rho_n 32\pi R^2 \frac{V^2}{D}\int_{r=0}^{r=R}\left(\frac{r}{R}\right).\left[1-\left(\frac{r}{R}\right)^2\right]\left(\frac{r}{R}\right).d\left(\frac{r}{R}\right)$$

Equation 5.18

$$\Gamma = \rho_n 32\pi R^2 \frac{V^2}{D}\int_{t=0}^{t=1}.\left(t^2 - t^4\right).dt = \rho_n 32\pi R^2 \frac{V^2}{D}\left(\frac{t^3}{3}-\frac{t^5}{5}\right)\Bigg|_{t=0}^{t=1} = \rho_n 32\pi R^2 \frac{V^2}{D}\left(\frac{1}{3}-\frac{1}{5}\right) = \frac{64}{15}\rho_n \pi R^2 \frac{V^2}{D}$$

To obtain the average shear strain rate experienced by the particles in the filtrate, Equation 5.18 and Equation 5.12 are evaluated together:

$$\bar{\gamma} = \frac{\sum_{i=1}^{N} n_i \gamma_i}{\sum_{i=1}^{N} n_i} = \frac{\Gamma}{P} = \frac{\frac{64}{15}\rho_n \pi R^2 V^2 / D}{\rho_n \pi R^2 V} = \frac{64}{15}\frac{V}{D} = 4.27\frac{V}{D}$$

Equation 5.19

As described earlier, the force that significantly contributes to the degradation of plasmid molecules is due to the elongational strain rate (Bustamante et al., 2000). In the next section, the relation between the shear and elongational strain rate has been established.

As a starting point for analysis, the plasmid particle is assumed as a rigid rod shape particle in contrast with the flexible, worm-like chain molecule of a plasmid. The assumption that a plasmid is a rigid and non-deformable particle was made to reduce the complexity of the analysis.

In this analysis, the particle is immersed in a Hagen-Poiseuille flow and its centre of gravity of the particle travels at the unperturbed local fluid speed.

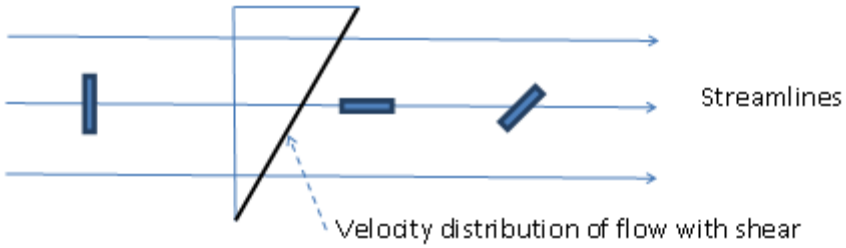

Figure 5.4- Possible trajectories of a rod-shaped particle in fluid flow.

The diagram in Figure 5.4 shows three rod-shaped particles immersed in a sheared flow at different orientation angles, θ = 90, 0 and 45 degrees relative to the streamlines. For the orientation angle θ = 0 (particle aligned with the streamline) all the 'parts' of the particle move at the same speed, so there is no net force or torque on this particle. The particle is in equilibrium with its environment and remains aligned with the flow in the same orientation.

The top of the particle at orientation angle θ = 90 degrees will be surrounded by fluid travelling at a speed that is larger than the speed at the centre of gravity of the rigid particle. At the bottom of the particle the speed will be lower. Therefore, the top of the particle experiences fluid with a positive relative velocity and the bottom experiences fluid with a negative relative velocity. The relative velocity due to the shear flow is everywhere perpendicular to the particle, so there are no elongation forces. However, the sheared flow causes a torque on the particle that will make the particle rotate in the clockwise direction.

At intermediate angle θ, the particle will experience a torque in conjunction with elongational strain.

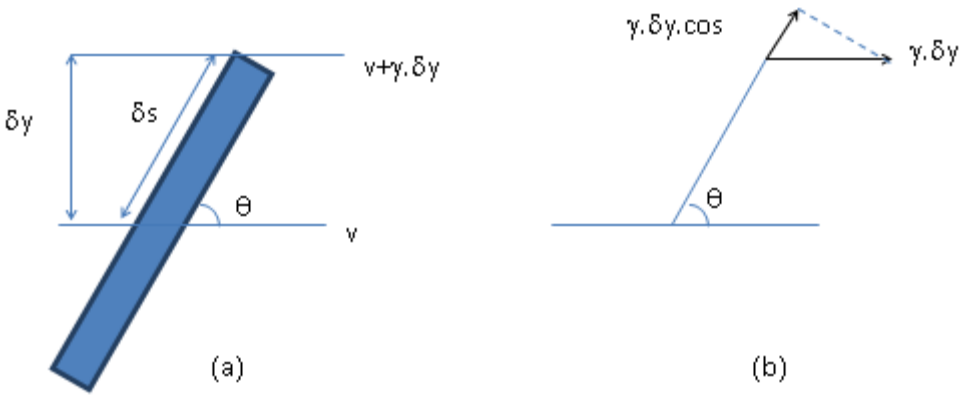

Figure 5.5- Orientation a particle at an angle, θ.

Consider the particle shown in Figure 5.5a with half-length δs at orientation angle θ. The top of this particle is at a vertical distance δy from its centre-of-gravity. At this location the relative fluid velocity $\delta v = \gamma.\delta y$. It is also easy to see in this diagram that $\delta y/\delta s = \sin(\theta)$, so $\delta v = \gamma.\delta s.\sin(\theta)$.

The diagram in Figure 5.5a shows that the component of the relative velocity that is responsible for elongation of the particle is equal to $\delta v.\cos(\theta) = \gamma.\delta s.\sin(\theta).\cos(\theta) = [\gamma.\delta s.\sin(2\theta)]/2$. The elongational strain rate associated with a particle at orientation θ in a sheared flow with local shear strain rate γ is just the ratio of this component of the relative velocity and the distance:

$$\varepsilon = \frac{\delta v}{\delta s} = \frac{\gamma.\delta s.\sin(2\theta)/2}{\delta s} = \frac{\gamma.\sin(2\theta)}{2} \qquad \text{Equation 5.20}$$

The maximum of the elongational strain rate will occur when $\sin(2\theta) = 1$, hence when $2\theta = 90^o$, so at orientation angle $\theta = 45^o$.

$$\varepsilon_{max} = \frac{\gamma}{2} \qquad \text{Equation 5.21}$$

It should be noted that the other component of the relative velocity is perpendicular to the particle, so it will cause a torque to make the particle rotate (as for a particle at 90 degrees).

Hence, particles are only in equilibrium with their flow environment at orientation angle $\theta = 0$. At all other angles the particle will experience a torque to make it rotate towards $\theta = 0$, so, the planar analysis shows that all these rigid and rod-shaped particles should eventually end up aligned with the flow direction.

Particles that are exactly aligned with the flow upon entry to the cylindrical pore, i.e. $\theta = 0$, will remain in this orientation and will not experience any elongation. Particles that enter in this fashion along the centre line will not distort the answer, because along the centre line r = 0 the value of γ is zero anyway. However, at a different particle entry radius $r = r_e \neq 0$ the relevant shear strain rate contributes to the average according to Equation 5.19.

Particles that are oriented at $\theta = 90^o$ upon entry to the pore will experience a torque that rotates the particle until it reaches the equilibrium position. In the course of this rotation, the particle will experience a sinusoidal varying elongation force, increasing to a maximum value as the particle rotates to 45^o and subsequently decreasing again as the particle approaches its final equilibrium position, $\theta=0$. If the length of the pore is such that a complete rotation is accomplished, the particle will experience all possible elongation strain rates starting at zero up to the local maximum and down to zero again.

Since the particle experiences variable elongation strain rates depending on its orientation, this phenomenon should be taken into account in formulating the equation for the elongation strain rate. However, in using this theory, the particles have a tendency to end up aligned with the flow and portions of their trajectory should be excluded from the count (for example if a pore is extremely long, the particles are eventually all lined up with the axis of the pore and the longer the pore, the smaller would be the elongation stain rate if these portions of the trajectory were counted).

So the conditional average elongation strain rate is proposed as a metric to measure the degradation of a particle when it travels into the pore. The word conditional implies that only particles that experience elongational strain are counted during their trajectory and exclude from the count those parts of the trajectory where the particle is aligned with the flow and is not experiencing any elongation strain (i.e. particles entering the pore at initial orientation $\theta = 0$ would not contribute at all and for particles with initial orientation angle $\theta \neq 0$, the final part of the particles trajectory through the pore when it is aligned with the flow and does not experience

any elongation strain rate is also excluded). For a particle with initial orientation angle $\theta = 90^o$ this conditional average elongational strain rate and upon its passage through the pore would be given by Equation 5.21 multiplied by the average of sin (2θ) between $\theta = 90^o$ and $\theta = 0$, which is equal to $2/\pi \approx 0.64$.

For a general initial orientation angle θ_i (radians) the average elongational strain rate should be constructed by pre-multiplying with the following factor to take into account the effect of changing orientation:

$$\frac{1}{\theta_i}\int_{\theta=0}^{\theta=\theta_i}\sin(2\theta)d\theta = \frac{1}{2\theta_i}\int_{t=0}^{t=2\theta_i}\sin(t)dt = -\frac{1}{2\theta_i}\cos(t)\Big|_{t=0}^{t=2\theta_i} = \frac{1}{2\theta_i}\left(1-\cos(2\theta_i)\right) \qquad \text{Equation 5.22}$$

Without prior knowledge of the entry process, it seems reasonable to consider that particles may enter the pore at any initial orientation angle. On that basis, the correct initial angle factor F_θ should be:

$$F_\theta = \frac{1}{\pi/2}\int_{\theta_i=0}^{\theta_i=\pi/2}\frac{1}{2\theta_i}\left(1-\cos(2\theta_i)\right)d\theta_i = \frac{1}{\pi}\int_{t=0}^{t=\pi}\left(\frac{1-\cos(t)}{t}\right)dt \qquad \text{Equation 5.23}$$

Using Excel and trapezoidal rule integration, the calculated factor of F_θ is 0.525. However, the plot of the function in Equation 5.22 shows that the maximum of this pre-multiplier is not 0.64 (located at 45°), but is higher at 0.725 (around 66.7°). This suggests that particles entering at orientation angle greater than 45° will experience near-maximum elongation strain rates over a considerable part of their trajectory. These particles will deliver a higher contribution to the average than particles that enter at 45°, which just experience the maximum elongation strain rate at the start of their trajectory in the pore, but quickly turn to lower angles with smaller elongation strain rates.

To summarize, on this basis, the conditional average elongational strain rate associated with shear experienced by particles in Hagen-Poiseuille flow assuming uniformly distributed particles with random orientation angle at entry to the pores is given by:

$$\bar{\varepsilon} = \frac{32}{15}\frac{V}{D}F_{\theta} \qquad \text{Equation 5.24}$$

where F_{θ} is given by Equation 5.23.

Inserting the approximate value of F_{θ} = 0.525, the following final expression for the conditional average elongational strain rate is:

$$\bar{\varepsilon} = 1.12\frac{V}{D} \qquad \text{Equation 5.25}$$

5.2.3 ***Development of method to calculate the local elongational strain rate using 'image to simulation' workflow***

The simulation methods described in previous subsections (5.2.1 and 5.2.2) are limited for estimating the average velocity and strain rate in cylindrical pores. However, the local velocity and strain rate inside a membrane might vary depending on the size and shape of the interconnected pores. Visual analysis of the polymeric membrane used in this work show that a broad range of pore diameter is detected; between ~0.05 to 2 µm. It is a possibility for plasmid molecules to follow the path of high strain rate present in certain regions inside the membrane. Therefore, estimation of the magnitude of the strain rate inside the membrane is critical to evaluate the correlation between DNA degradation and the operations of the filtration. In this section, the magnitude of the strain rates is estimated using the actual geometry of the membrane as a template for finite element analysis.

The geometry was obtained by images that were acquired by transmission electron microscopy (TEM). The TEM allows us to determine the depth of the membrane matrix which is one of a critical input parameters during the simulation. Approximately 70 nm of membrane layers were

sliced and prepared. In contrast with scanning electron microscopy (SEM), the segmentation of images using image processing technique is needed in order to estimate the depth of the geometry.

However, by using current commercial CFD codes and computer capacity, it is computationally expensive to insert mesh and solve fluid flow simulation (using finite element analysis) of a large membrane's geometry. By sub-sampling the geometry, it is possible to employ a smaller portion of the membrane as a representative of the complete geometry. In this simulation, only a small portion of the membrane's cross sectional area was considered. Five images of the membrane were processed to provide statistically reliable data for a set of membrane simulations.

During image processing, the images (acquired in *tagged image file format*; *TIFF*) were first transformed into matrices and binary image formats using *Matlab*. The images were then converted to a 2D curve object using the 'flim2curve' command available in the *Matlab-Comsol Multiphysics* interface. The 'flim2curve' command detects the contour line based on the image data. The images were then exported to the *Comsol Multiphysics* software for numerical simulations.

In order to perform a 3D simulation, the height was added to the imported image using the 'extrude' option in *Comsol*. The geometry was extruded along the z-axis of the plane at 70 nm; corresponding to the depth of the layer that was sliced in the TEM protocol. The fluid domain was obtained by Boolean operation of the object by subtracting the image imported from *Matlab* from a cube (7.6 µm x 6.8 µm x 0.08 µm) created using the CFD software.

The inlet pressures were imposed at the inlet boundary conditions of the representative geometries, corresponding to the transmembrane pressures of the actual filtration at 5 and 8 psi. The depth of the representative geometry is ~4 % of the actual geometry; where the thickness of the membrane was measured using Talysurf CLI 200 (Taylor Hobson, Leicester, UK) by employing chromatic length aberration gauges. Based on the symmetrical structure of the membrane (as confirmed by the SEM image), the pressure profile inside the membrane is assumed to distribute uniformly with the depth of the membrane, the transmembrane pressures of the representative geometry were estimated at 4% of the actual pressure drop of the actual filtration system. The fluid domain was treated as incompressible with a density, ρ=1000 kg/m^3

and dynamic viscosity of 1 cP. The membrane matrix is treated as closed wall with no slip condition.

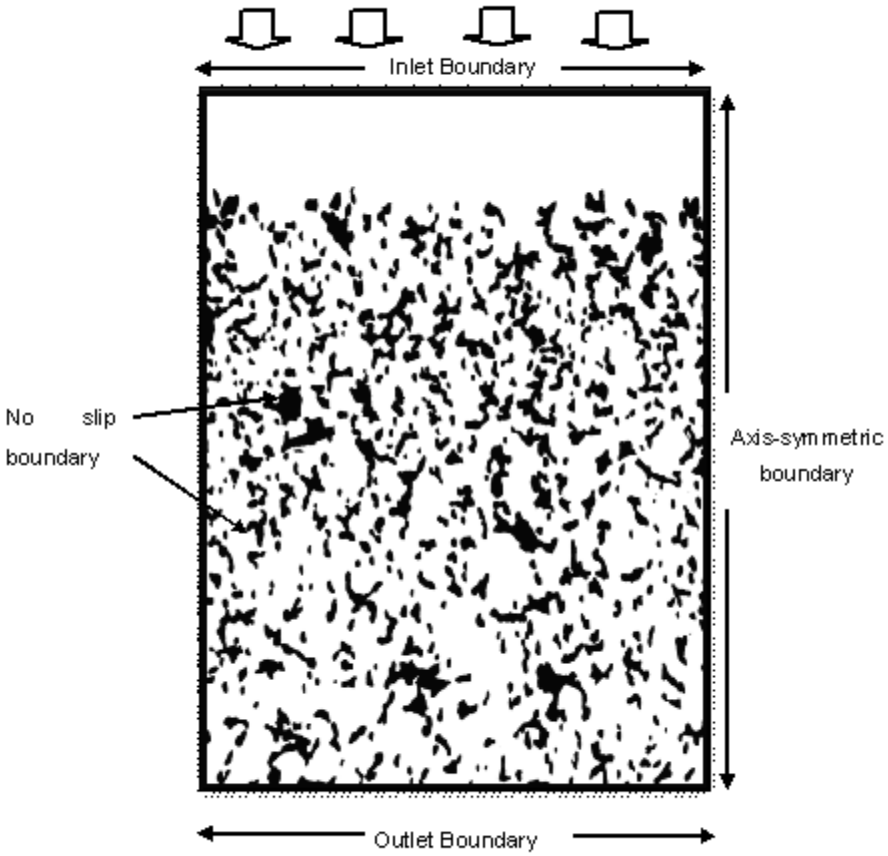

Figure 5.6- The boundary conditions of the CFD simulation

5.3 **Experimental approaches**

A solution of 50 µg/ml pQR150 (20 kb) plasmid DNA was filtered through 0.22 µm polyvinylidene fluoride (PVDF), 13 mm membrane (Millipore Corporation, MA, USA) at 5 and 8 psi under constant transmembrane pressure filtration. The set up of the filtration is described in Materials and Methods (section 2.7).

The filtrates were then analysed using agarose gel electrophoresis to determine the loss of plasmid topologies during filtration. Based on the densitometry analysis of gel electrophoresis, the relative supercoiled and open circular plasmids DNA content in the filtrates were measured using equation below:

$$\%SC,OC_{filtrate} = (I_{Filtrate_{SC,OC}} / I_{Feed_{SC,OC}}) * 100$$

Where $I_{Filtrate\ SC,OC}$ is the trace intensity (intensity of SC and OC's bands multiplied by pixel area occupied by the band) of plasmids in the filtrate and $I_{Feed\ SC,OC}$ is the trace intensity of plasmids in the feed.

The degree of plasmid loss was correlated with the magnitude of the elongational strain rate estimated using the CFD methodology. Two methods of simulation had been developed, first the estimation of the average elongational strain rate using the Brinkman equation and second; the estimation of local strain rate using 'image to simulation workflow'. The simulation results were also compared with the theoretical calculation of the critical elongational strain rate (the strain rate that theoretically caused breakage of a plasmid DNA chain) and data reported in the literature.

5.4 Results and discussion

5.4.1 *Estimation of the average elongational strain rate during the progression of fouling and its correlation to plasmid DNA loss from macro-scale CFD model*

5.4.1.1 The impact of the elongational strain rate to plasmid loss

The simulation (in Figure 5.7) provides the average velocity magnitude at a specific permeability and porosity of the membrane which represents the degree of fouling throughout the entire course of filtration. The velocity magnitude and the average size of the pore (calculated using Equation 5.9) were then used as a basis for calculating the elongational strain rate (Equation 5.6). Figure 5.8 indicates the trend of the average elongational strain rates during the filtration of pQR150 (20 kb) plasmid at 5 and 8 psi transmembrane pressures.

As expected, the elongational strain rate increased as the filtration progressed. During filtration, the retention of plasmids on the surface and inside the membrane caused fouling and reduction of the available pore area for plasmid trajectory (chapters 3 and 4). The magnitudes of the elongational strain rate of both 5 and 8 psi filtrations were identical for the first 5 minutes of filtration. Afterwards, both plots deviate with the elongational strain rates at 8 psi increased more than that at 5 psi. At 20 minutes, the average elongational strain rates reached 7.42×10^3 and 9.54×10^3 s^{-1} for 5 and 8 psi transmembrane pressure filtrations respectively. These results suggest that higher transmembrane pressure contributes to increase of strain rate during filtration.

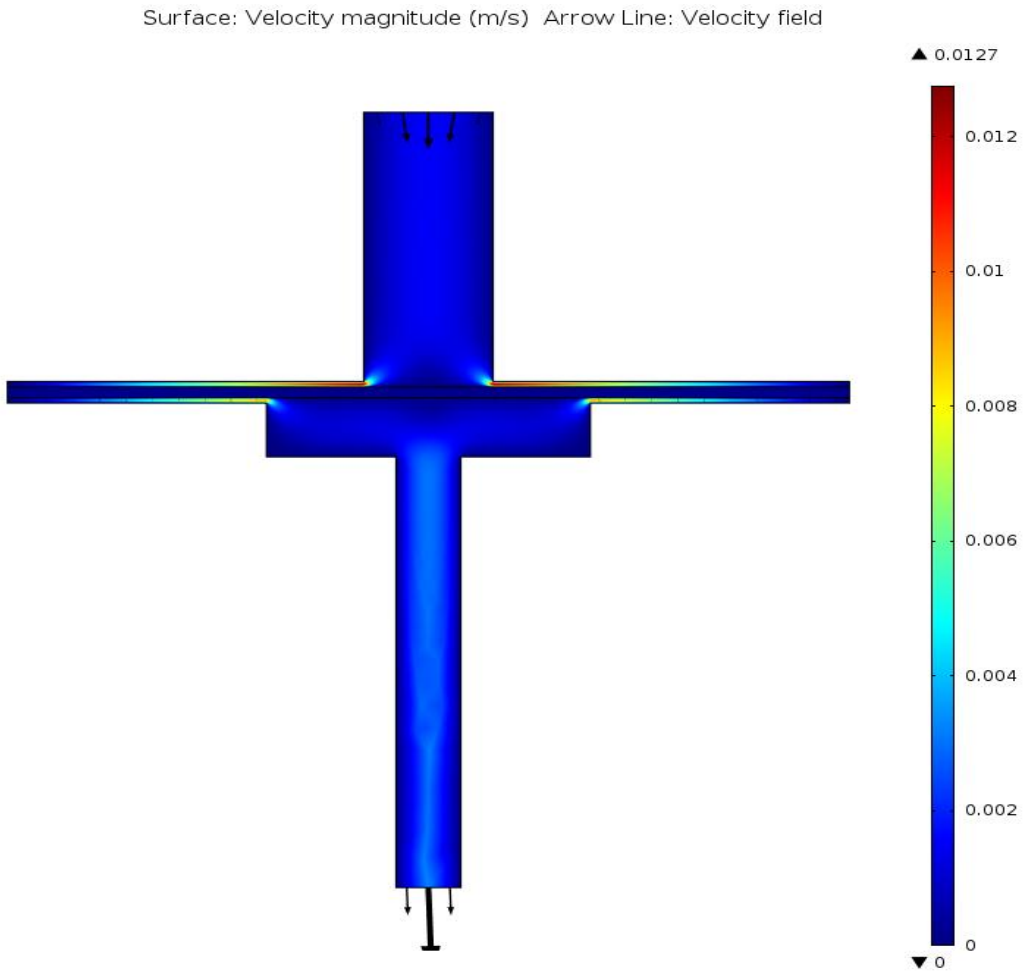

Figure 5.7- Postprocessing result of the simulation of the local velocity in a syringe filter unit. The arrows indicate the direction of the flow. The size of the arrows represents the magnitude of the velocity field. The velocity magnitude is represented in the colour bar. The fluid flows in fluid and porous domains were governed by the Navier Stokes and Brinkman equations respectively.

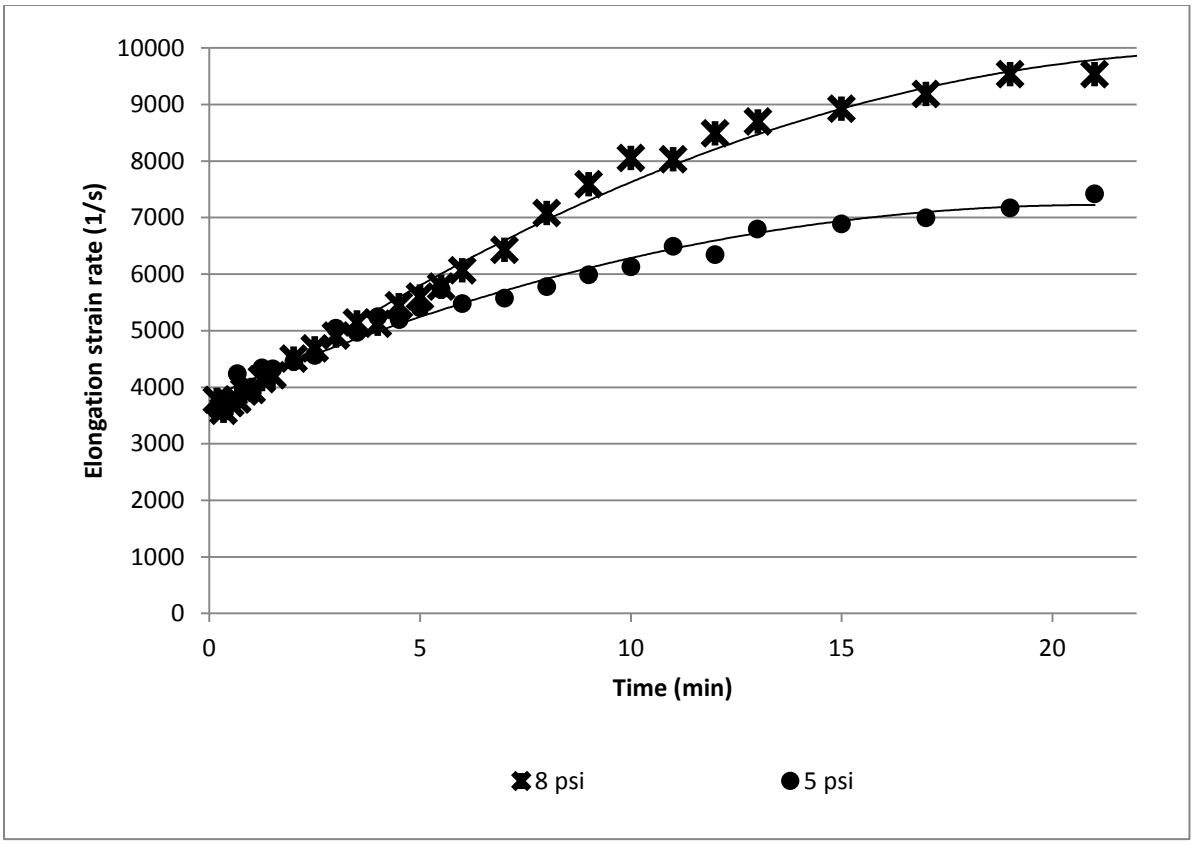

Figure 5.8- The average elongational strain rates during the filtrations at 5 and 8 psi transmembrane pressures. The magnitude of strain rate inside the membrane is calculated based on the flow field calculations using the Brinkman equation of Figure 5.7.

Previous studies have shown that high strain rate contributes to the degradation of valuable supercoiled plasmid topology during downstream processing (Levy et al., 1999a, Levy et al., 1999b, Kong et al., 2010, Arulmuthu et al., 2007) by scission of the phosphodiester bonds between the DNA bases (Bustamante et al., 2000). The breakage of this covalent bond contributes to the degradation of supercoiled plasmid DNA to other unwanted topologies such as open circular and linear DNA. To investigate whether this factor (the strain rate) affected the degradation of the 20 kb plasmid, the changes of plasmid topology were monitored (Figure 5.9 and Figure 5.10).

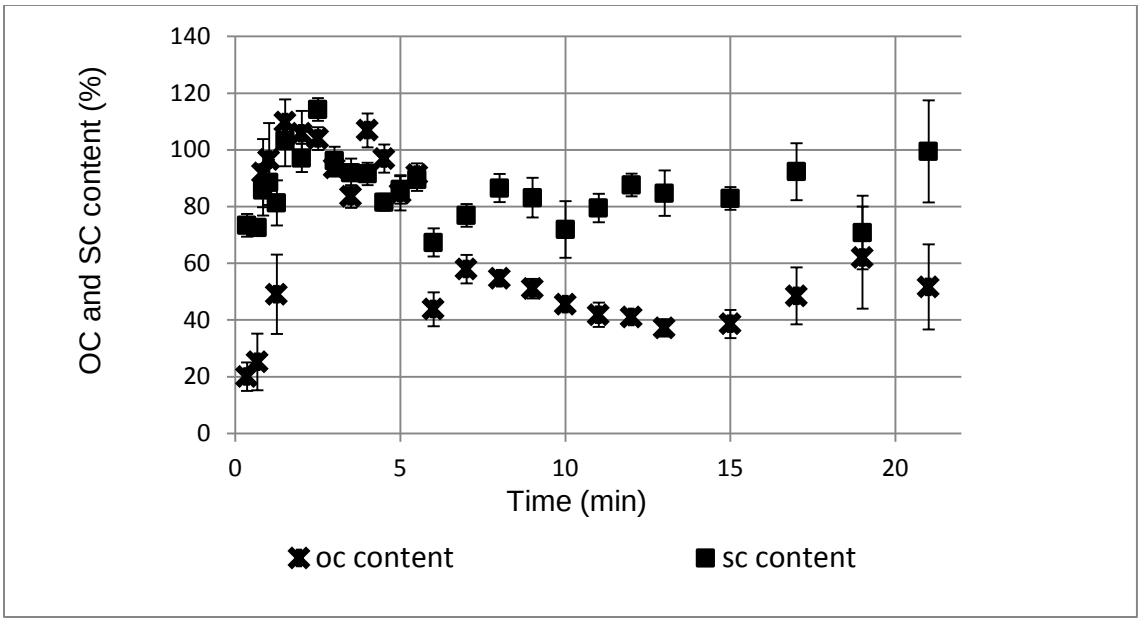

Figure 5.9- The relative supercoiled and open circular plasmids DNA content of pQR150 (20kb) after filtration through a 0.22-µm pore rated membrane at 5 psi transmembrane pressure. The analysis was done using densitometry and gel analysis software of agarose gel electrophoresis. The error bars indicate the standard deviation of the agarose gel electrophoresis method (n=3).

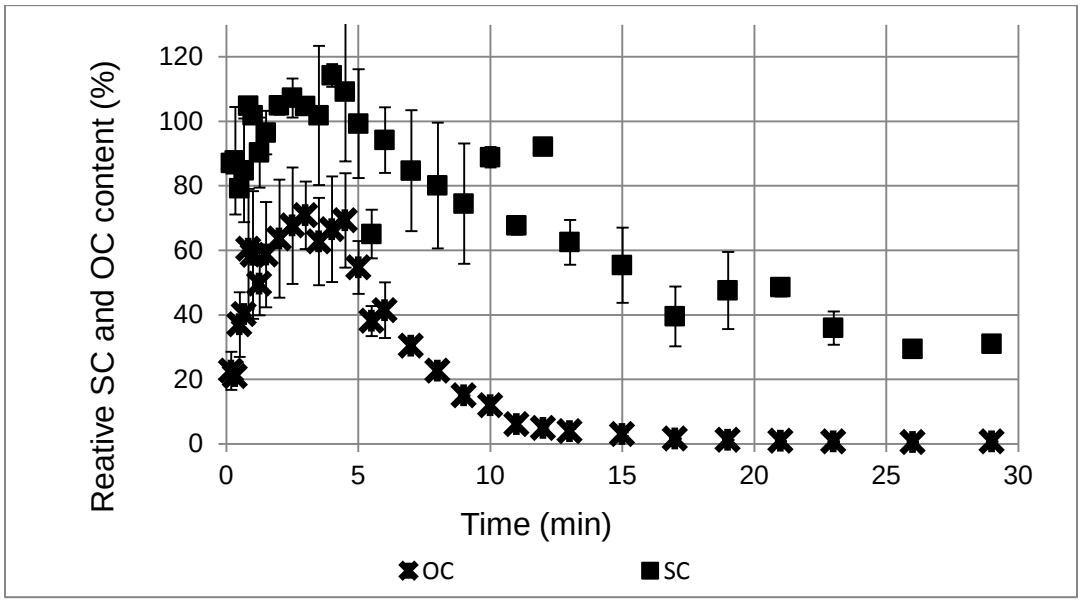

Figure 5.10- The relative supercoiled and open circular plasmids DNA content of pQR150 (20kb) after filtration through a 0.22-µm pore rated membrane at 8 psi transmembrane pressure. The analysis was done using densitometry and gel analysis software of agarose gel electrophoresis. The error bars indicate the standard deviation of the agarose gel electrophoresis method (n=3).

During filtration at both transmembrane pressures, the loss of OC plasmid is worse than the loss of SC. This suggests that the molecular size of OC is larger than the SC plasmid. The result is in agreement with the particle size distribution analysis of plasmid topologies (Chapter 4).

The loss of OC plasmid is due to the retention of this topology during filtration. However, the loss of SC plasmid is due to the retention of this molecule and the degradation to OC plasmid topology. The degradation of SC plasmid during filtration in a clean filter (when no fouling is suspected to occur) may result in the decrease of SC and the increase of OC plasmids in filtrates. However, during the filtration where fouling is the function of filtrate volume, the degradation of SC to OC is hard to detect since the degraded SC plasmid (the degraded isoform of SC that degrade to OC due to fluid stresses) may also be trapped inside the membrane.

8 psi transmembrane pressure, the SC contentdecreased after 5 minutes of the filtration and this contrasts with the filtration at 5 psi where no significant decrease was observed. However, during the 5 and 8 psi transmembrane pressures filtration, the degradation of SC plasmid is very minimal since the trend of OC and SC contents of both transmembrane pressures is similar.

5.4.1.2 Comparison with literature

Levy et al (1999) reported that approximately 10% of the initial SC DNA content of a 20 kb plasmid was degraded in shear studies using a capillary rheometer with shear rate of 1.4×10^5 s^{-1} and residence time of 0.07 s (Levy et al., 1999b). Reese et al (1990) observed that the degradation of a 38 kb T7 DNA occurred when the molecule experienced strain rates above 10,000 s^{-1} in a steady sink flow (Reese and Zimm, 1990) . Using larger DNA, Atkins and Taylor (1992) reported that the breakage of 50 kb λ-DNA in an opposed jet occurred above 6000 s^{-1} (Atkins and Taylor, 1992). It should be noted that these reports suggest that the sensitivity of DNA molecules to strain rate increased with the molecular weight.

The finding by Levy et al (1999b) is critical since they used the same size of plasmid as this work. However, the difference lies in the residence time of the plasmid at high strain rate regions during the processing; where the molecule experienced such forces. Obviously, the trajectory of DNA inside the experimental rigs in previous reports differs with the trajectory inside the membrane. Consideration is needed as these reports involved experiments that were

performed in idealised flows that contrast with the more complex flow fields inside the membrane.

Ryskin (1987) suggests an equation that describes the rupture at the midpoint of a polymer chain caused by a stretching force that is comparable to the bond strength(Ryskin, 1987);

$$F_{\max} = k_1 \mu \varepsilon l^2 \qquad \text{Equation 5.26}$$

Where F_{max} is the maximum hydrodynamic force to break the polymer chain (N), k_1 is dimensionless constant, ε is the elongational strain rate (s^{-1}) and l is the plasmid's contour length (m). The contour length of a 20 kb plasmid is estimated ~ 6.8 µm (estimated by number of DNA base pairs multiplied by axial rise between base pair ~ 0.34 nm). The value of k_1 is given by;

$$k_1 = \frac{1}{2}\pi \frac{1}{\ln(5\pi / 2c[\eta])} \qquad \text{Equation 5.27}$$

Where c is DNA concentration (g/ml) and ŋ is intrinsic viscosity (ml/g). For a DNA concentration of ~ 50 µg/ml and an intrinsic viscosity ~2,500 ml/g, the value of k_1 is 0.228.

The force that is necessary to break the double stranded DNA, F_{max} varies as reported in the literature. The magnitude of force that is needed to break a DNA molecule is between 480 to 5,000 pN (Bensimon et al., 1995, Noy et al., 1997, Bustamante et al., 2000, Lavery et al., 2002, Lebrun and Lavery, 1996). By taking F_{max} ~500 pN, the estimated elongational strain rate that caused breakage of a 20 kb plasmid is ~47,000 s^{-1}.

If the analysis of plasmid DNA degradation is based on the above theoretical calculations, the magnitude of the average elongational strain rate obtained from the macro-scale CFD simulation is insufficient to break the plasmid DNA molecule. These values are 4-5 orders of magnitude lower than the critical strain rate for plasmid breakage. However, as described before, the average elongational strain rate obtained using the Brinkman equation is the

magnitude inside a control volume that do not count for the local strain rate. The detection of the local strain rate inside the membrane will be discussed in the next section.

5.4.2 ***Micro-scale simulation of the local elongational strain rate using the 'image to simulation workflow'***

Figure 5.11 shows a segment of the cross section of the PVDF membrane after it was processed and exported to the *Comsol Multiphysics* software. The exported image (Figure 5.11) suggests an exact translation of the image acquired from the electron microscopy to a contour image that defines the boundary of the membrane domain (Figure 5.6). The methods applied successfully overcame the main challenge of converting a RGB (Red, Blue, Green) image to a vector polyline format, namely, the possibility of loss of some details of the original image. The command 'flim2curve' successfully creates a 2D curve objects from the image data for detection and creation of the contour of the membrane matrix.

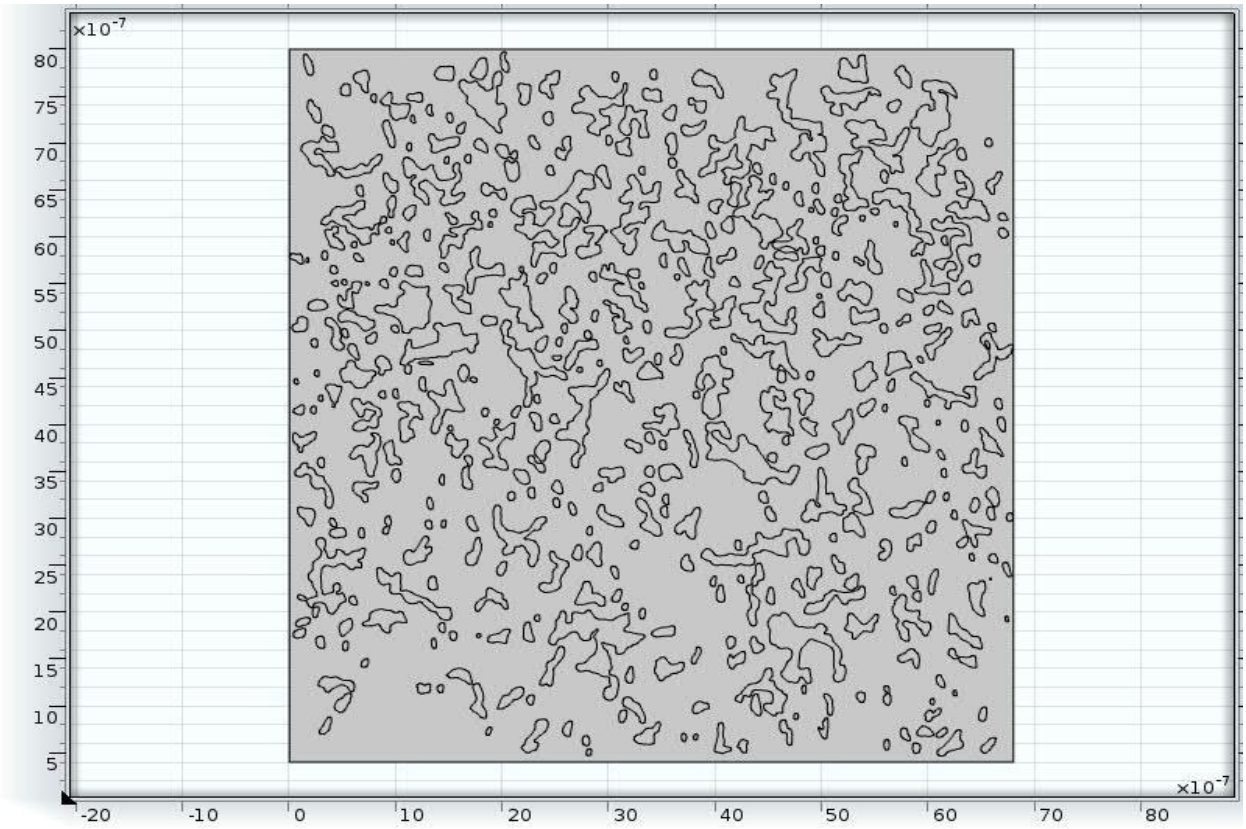

Figure 5.11 - The contour image of the membrane after being processed using Matlab and Comsol Multiphysics software. The processes include the conversion of a RGB image to a vector polyline format, detection and creation of contour of membrane matrix, creation of fluid domain by Boolean operations and extruding a 2D object to a 3D geometry.

Figure 5.12 shows the computational mesh inside the representative geometry of the membrane. The postprocessing results of the simulation are presented in Figure 5.13 and Figure 5.14 which represent the elongational strain rates at 5 and 8 psi transmembrane pressure filtrations respectively.

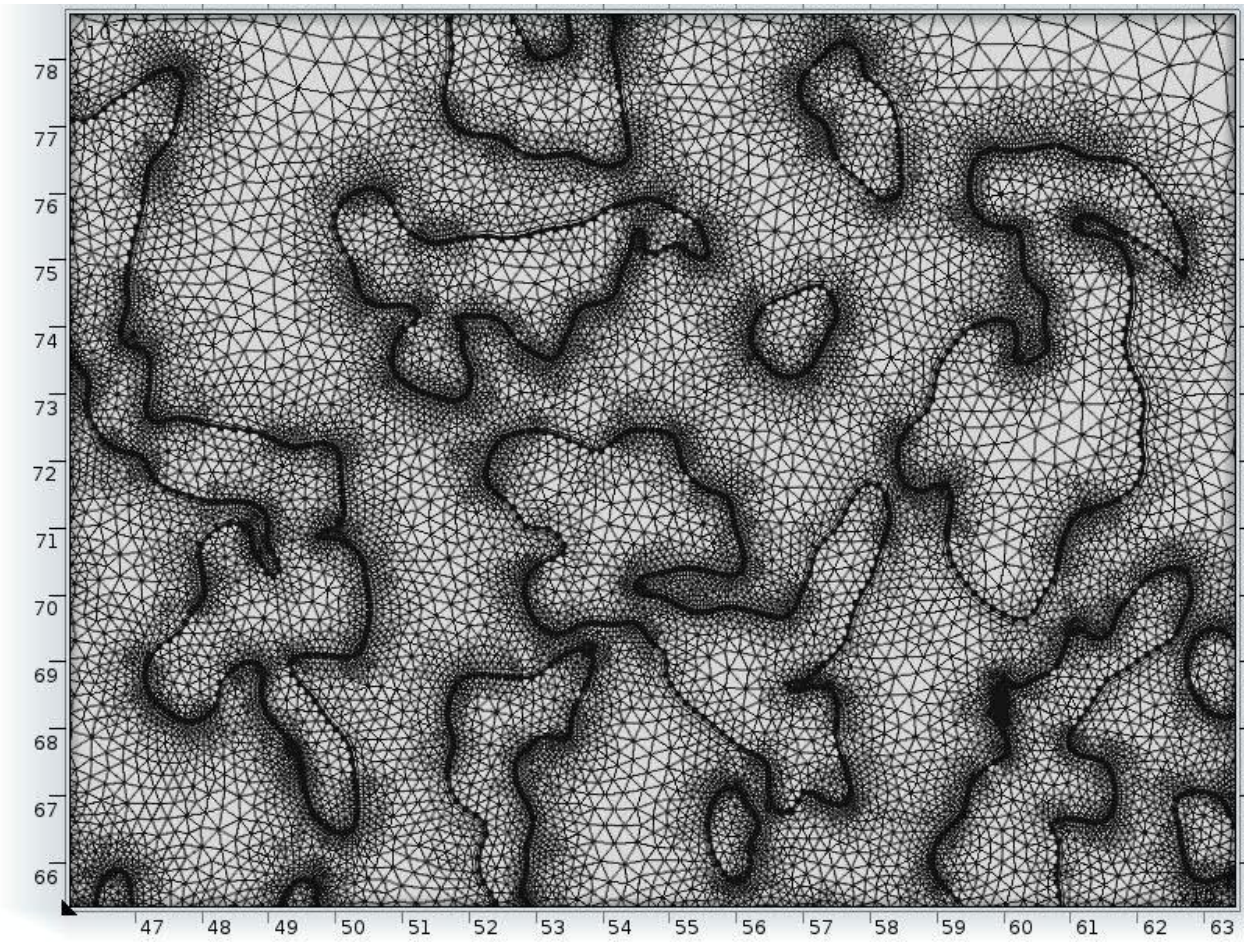

Figure 5.12 - The computational meshes of the imported image. This image is the sub-portion of the image of the membrane in Figure 5.11.

The flow pattern in Figure 5.13 and Figure 5.14 is visualised with colour-coded graphical representation that characterize the magnitude of the elongational strain rate. The strain rate plots (Figure 5.16 and Figure 5.17) were then obtained by plotting the strain rate magnitudes along an arbitrary line along the cross section of the image (Figure 5.15).

High elongational strain rates were detected at the centre and near the pore wall. The ‘gap’ in the plots (Figure 5.16 and Figure 5.17) indicates that the arbitrary line in Figure 5.15 impose on the non-fluid domain.

As suggested in Figure 5.16 and Figure 5.17, fluctuation of strain rates is observed. Practically, the magnitude of the local elongational strain rate estimated by the ‘image to simulation’ workflow distributed below ~5,000 s^{-1} which is consistent with the average value of the elongational strain rate obtained by the simulation using the Brinkman equation at time 0 (clean membrane) (sub chapter 5.4.1.1); which is approximately ~ 4000 s^{-1}. However, the magnitude of strain rate increased dramatically at certain regions inside the membrane. The highest elongational strain rates magnitudes were detected near the pore’s wall at 60,000 s^{-1} and 100,000 s^{-1} for 5 and 8 psi respectively.

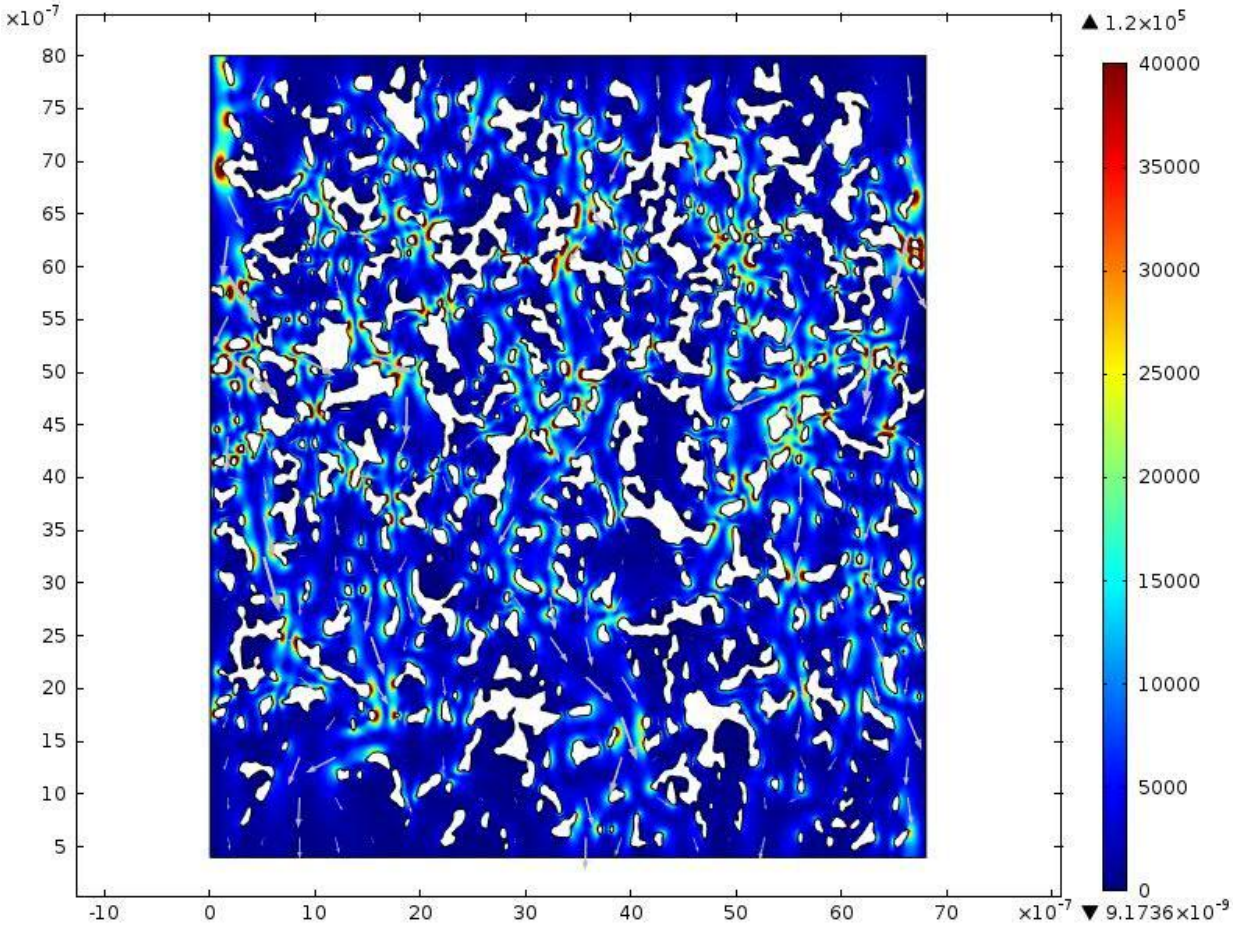

Figure 5.13 - The elongational strain rate inside the membrane during the filtration at 5 psi transmembrane pressure. The colour coded scale represents the magnitude of the elongational strain rate. The arrows represent the direction of the fluid flow.

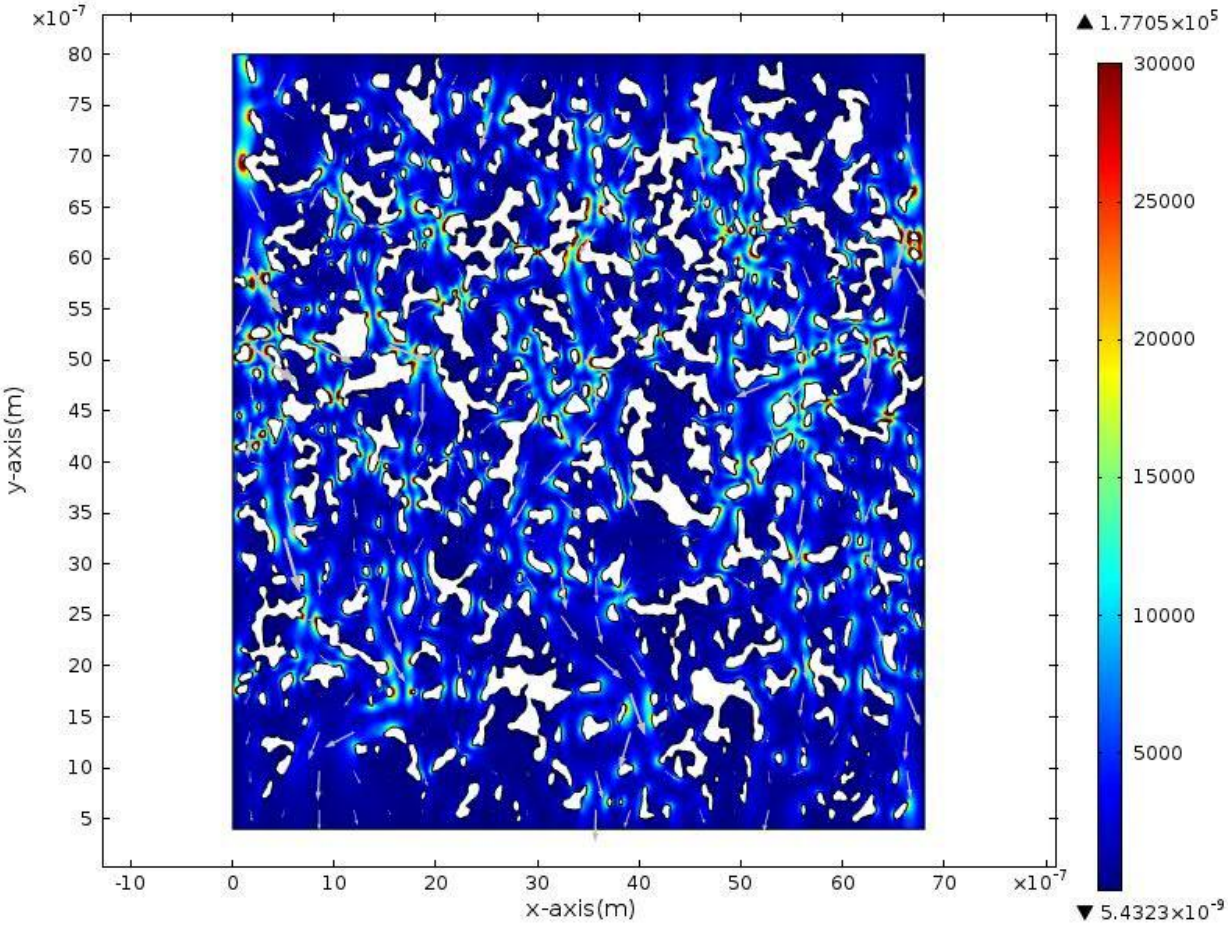

Figure 5.14 - The elongational strain rate inside the membrane during the filtration at 8 psi transmembrane pressure. The colour coded scale represents the magnitude of the elongational strain rate. The arrows represent the direction of the fluid flow.

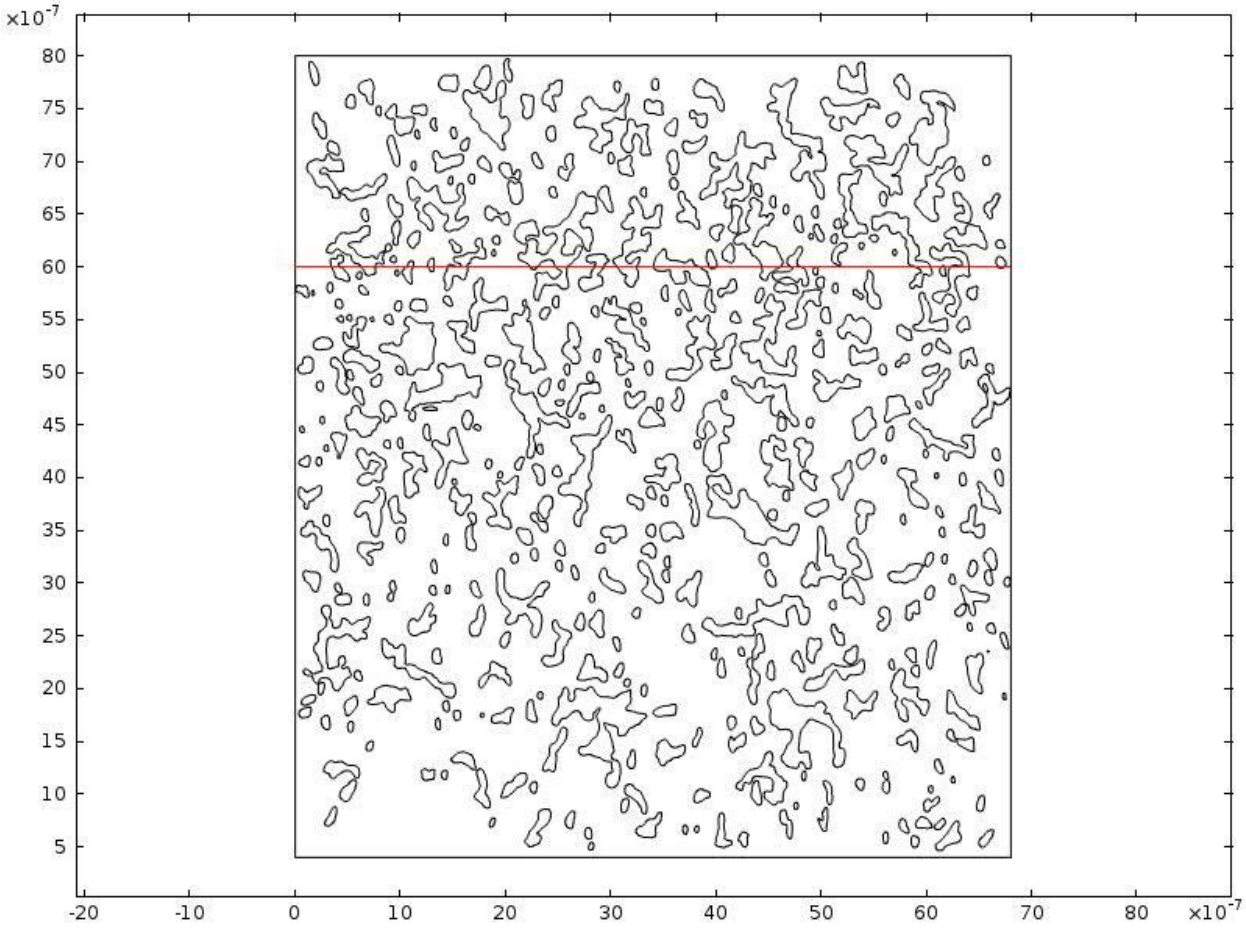

Figure 5.15 - The horizontal line across the image of the membrane is an arbitrary line used to determine the magnitude of the local elongational strain rates.

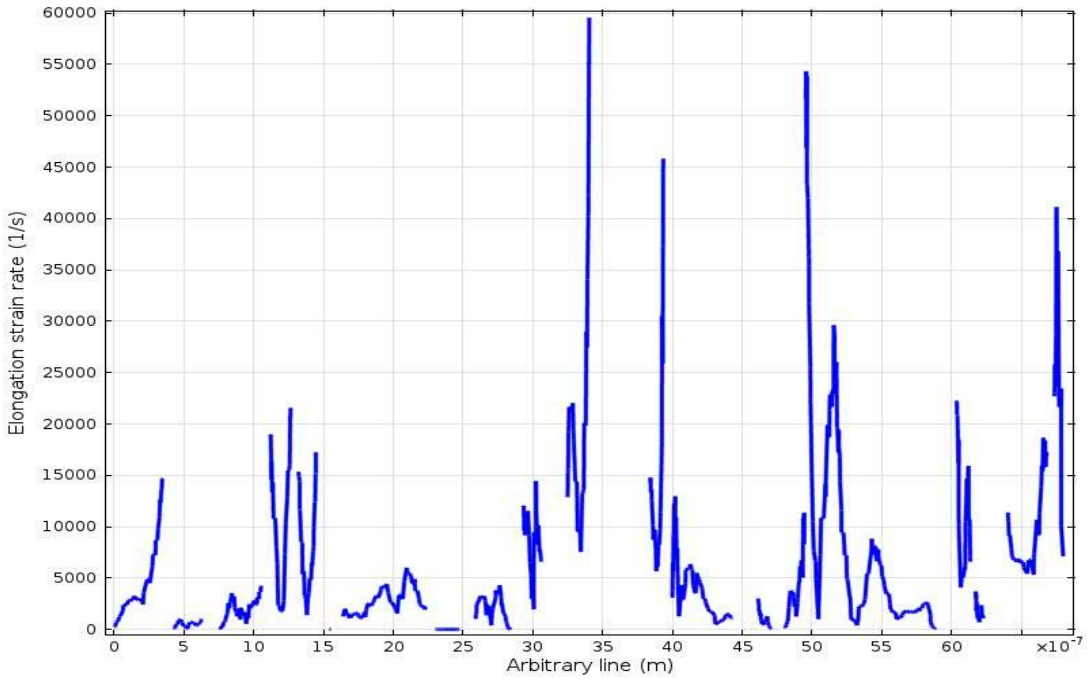

Figure 5.16 - The magnitude of the elongational strain rate as detected along an arbitrary line in Figure 5.15.

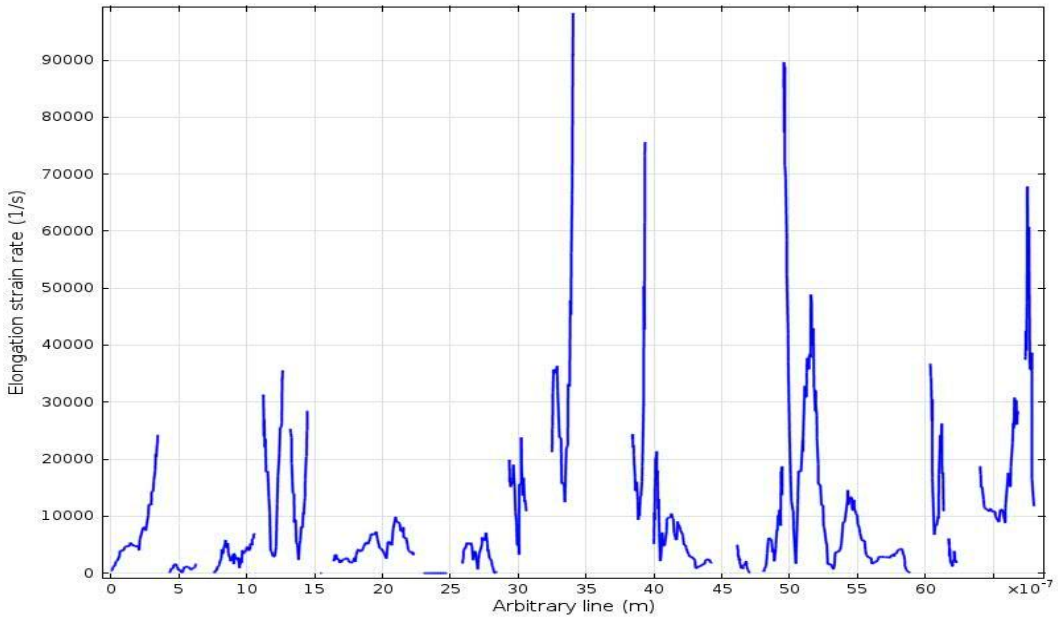

Figure 5.17 - The magnitude of the elongational strain rate as detected along an arbitrary line in Figure 5.15.

In most practical flows; such as flows inside a membrane, they consist of a mixture of rotational and elongational components. In the case of the dynamics of flexible polymer molecules (plasmid DNA can be considered as a polymer), the rotational flow (vorticity) caused the rotation whilst the elongational flow deformed the polymer (Smith et al., 1999). During filtration, plasmid DNA experienced a mixture of flow components that caused rotation and straining motions. The straining motion experienced by DNA due to high elongational strain rate causes structural damage to the plasmids if the strain rate exceeds a certain critical value.

In the simulation, the elongation strain rate, ε is calculated through this equation:

$$\varepsilon = \sqrt{\left(\frac{du}{dx}\right)^2 + \left(\frac{dv}{dy}\right)^2} \qquad \text{Equation 5.28}$$

Where u is velocity in x direction (m/s) and v is the velocity in y direction (m/s).

The elongational strain rate detected using this method is capable of identifying a high magnitude of strain rate that potentially causes breakage of plasmid DNA molecule. In comparison, the maximum values detected using these simulations; which is up to 60,000 and 100,000 s^{-1} for 5 and 8 psi transmembrane pressures respectively, potentially degrade the plasmid DNA as the elongational strain rate above > 40,000 s^{-1} is needed to break the 20 kb plasmid chain (calculated using Equation 5.27). However, the degradation of this molecule depends on its trajectory and the residence time of the plasmid in the high strain rate regions. The breakage of plasmid is a function of the location of the plasmid in the flow field. Degradation occurs if the plasmid molecule follows the flow path that contains high elongational strain rates and experiences the stretching force longer than its relaxation time. The relaxation time is the longest time required to bring the plasmid back to its natural equilibrium state after experiencing elongation of its chain (Latulippe et al., 2008).

Since the trajectory of a plasmid molecule depends on the flow fields, it is possible that the molecule experienced the fluctuation of high and low strain rates during its trajectory. Due to high elongational strain rates near the wall of the pore (as observed in Figure 5.17), it is suspected that the breakage of plasmids occurred at these locations. The flow accelerates in

the axial direction and as a consequence the end of a molecule that is closest to the pore entry will experience relative flow that tries to elongate it whilst pulling it into the pore. The rear end of the plasmid will experience relative flow in the opposite direction trying to hold it back.

In addition, the size of plasmid DNA (in terms of the hydrodynamics and radius of gyration) is larger than the nominal pore size (see Chapter 4) suggesting that a plasmid molecule might experience a wide range of strain rates along its molecular structure. This increases the possibility of a single plasmid molecule to experience differential migration of its structural components. The plasmid molecules experiences different migration of its components since the membrane consists of regions of high elongational forces and near zero stagnation points (Figure 5.13 and Figure 5.14).

Residence time influences the fate of a plasmid molecule: it is unlikely to break if it experiences a very high strain rate during a short time interval in the region of high strain rate (shorter than its relaxation time). However, retention of a plasmid causes entanglement of this molecule inside the web of interconnected pores (see Chapter 3). If the rear part of a single molecule is trapped with the other parts exposed to the high elongational strain rate, the residence time in the region of high elongational strain rate is long and degradation is possible.

During the trajectory through a membrane, a single plasmid molecule experiences a range of strain rate magnitudes along its chain. This provides both advantage and disadvantage in term of filterability as it causes entrapment and penetration of a plasmid molecule. The wide range of strain rates allowed the plasmid to stretch and deform resulting in the blockage of the membrane through entanglement of this molecule along the complex structure of pores.

However, the plasmids that initially trapped on and inside the filter may infiltrate the membrane as the deformation and stretching of plasmids allow the penetration through the membrane. These phenomena correlate with a sudden increase of SC/OC content at the early stage of the filtrations; before 3 and 5 minutes during 5 and 8 psi transmembrane pressure filtrations respectively (Figure 5.9 and Figure 5.10). This increase followed the low level of SC/OC content at the beginning of the filtration. The results suggest that the plasmids experienced entrapment and entanglement on and inside the membrane during the early time of the filtration as only a small amount of SC/OC content was detected in the filtrates. In addition, the mixed flow regimes inside the membrane caused physical manipulations such as rotation, stretching

and deformation. Even a plasmid initially trapped inside the filter, the nature of this molecule that is flexible and deformable allows it to realign and penetrate the pores. The combination of entrapment and realignment during the trajectory contributed to the differential migration of different parts of the plasmid's molecular structure hence accounting to its degradation. This hypothesis is supported by reports that show DNA can penetrate and realign its structure to penetrate the pores (Latulippe et al., 2008, Hirasaki et al., 1995).

Although a high elongational strain rate was detected during filtration at 5 and 8 psi, the breakage of SC plasmid only occurs when the plasmid is exposed to the high elongational strain rate longer than its polymer relaxation time. Besides, elongational strain rates below ~40 000 s^{-1} were detected in most regions inside the membrane, which is below the critical elongational strain rate for DNA breakage (Sub chapter 5.4.1.2). It is suggested that the strain rate inside the sterilising grade PVDF filter at 5 and 8 psi transmembrane pressures is incapable of breaking the SC plasmid DNA. This is also in agreement with the experimental results as explained in Sub chapter 5.4.1.1.

5.4.3 ***Comparison of models; micro-scale 'image to simulation' workflow vs. the macro-scale simulation using Brinkman equation***

The simulation using the Brinkman equation and the 'image to simulation' method suggested that both offered a comparable result. However, the latter is capable to detect the elongational strain rates that are critical for the degradation of SC plasmid DNA. The simulation using the Brinkman equation offers a simple and less computational costly method for prediction of fluid flows. The simplicity of the geometry of the control volume reduced the computational mesh that is required to solve the simulation.

The simulation using the Brinkman equation provides a fast characterisation of strain rate and velocity magnitude. This is important for the estimation of quality and transmission of the product of interest during filtration trials with different types of membranes. Besides, the method is capable of predicting important fluid flow parameters during the progression of fouling.

5.5 **Conclusions**

The significant loss of SC plasmid DNA was detected during 8 psi transmembrane pressure. However, the loss of this molecule through degradation from SC to OC topology is not significant since similar trend of SC and OC losses were detected.

This chapter provides methods to investigate fluid flow regimes inside sterile filters. The macro- and micro-scale CFD simulations were then used to predict the elongational strain rate that is critical for the breakage of SC plasmid DNA. The macro-scale simulation provides a fast and simple technique to characterise the fluid flow. The mathematical method developed in this chapter estimates that the average elongational strain rate at 8 psi filtration is below 10,000 s^{-1}. This strain rate is 4-5 orders of magnitude lower than the critical strain rate for plasmid degradation. However, the accuracy of the estimation can be improved and it will be discussed in the subsequent chapter.

The micro-scale simulation employs the images from transmission electron microscopy and estimates local strain rate that may critical for SC plasmid degradation. The 3D fluid flow simulation of the membrane provides a novel way to characterise the fluid flow regimes of a sterilising grade filter.

By comparing the simulation results, past literature and theoretical DNA breakage models with the data from experiments, it is concluded that the degradation of 20 kb SC plasmid DNA caused by the strain rates inside the sterilising grade filter is very minimal.

6 Conclusions and future work

6.1 Overall discussion and conclusions

6.1.1 *Key findings of the thesis*

Although the sterilising filtration of DNA has been studied recently (Watson et al., 2006, Kong et al., 2010, Kong et al., 2006), none of these studies explain the mechanism of fouling of large plasmid DNA. The investigation in this thesis provides a more complete and rigorous descriptions of the fouling mechanism of large plasmid DNA.

Based on the direct visualisation of fouling, chapter 3 suggests that the combination of fouling mechanisms occurred during progression of the filtration of pGEc47 (56 kb) plasmid. The blockage of the membrane was first dominated by the creation of meshes of DNA on the surface of the membrane. The build-up of these meshes is similar to the description of fouling as described by the intermediate blocking model. As the filtration progress, the entrapment of plasmids inside the internal structure of the membrane was detected as this can be correlated with the standard blocking model. A methodology (Sub chapter 3.3.1) has also been developed for visualisation of a fouled membrane using scanning electron microscope (SEM). This method successfully captured the image of DNA fouling on the surface and inside the filter.

Chapter 4 explains the mechanism of fouling using membrane blocking models. The results indicated that the blocking models and filtration law can be applied to explain the flux decline of large plasmid DNA filtration. The experimental data of pQR150 (20 kb) and pGEC47 (56 kb) at 5 and 8 psi transmembrane pressures provides the best fit with the intermediate-standard model which was first proposed by Bolton et al. (2006). The model was also able to explain the transition of fouling mechanisms of plasmid DNA using a plot of d^2t/dV^2 *versus* dt/dV. This finding can be a basis for filtration scale-up, since the accurate determination of the blocking model resulting in better approximation of the required membrane area of larger scale filter.

Kong et al. (2006) reported the loss of plasmids in terms of transmission and backbone integrity during the sterile filtration step. However, this study only gives insight into the loss of plasmid in

a practically clean membrane (where the filtrate was collected at the beginning of the filtration in constant flow rate filtration). Comparatively, this thesis provides data on the loss of plasmid DNA during the progress of fouling, which is monitored until the normalised flux decreased to approximately 0.01. The transmission and degradation of plasmids was monitored by comparing the feed and filtrate using UV spectrophotometry analysis and agarose gel electrophoresis respectively.

Finally, this study characterises the elongational strain rates inside a complex polymeric membrane which can have significant impact on breakage of plasmid DNA. The computational fluid dynamics (CFD) was employed to estimate the elongational strain rate using two approaches; macro- and micro-scale model. The macro-scale model estimates the average elongational strain rate using a simplified geometry of a syringe filter unit whereas the micro-scale model estimates the local elongational strain rate by employing the actual membrane structure acquired by transmission electron microscopy. Both models suggested that during the filtration of pQR150 (20 kb), the elongational strain rates detected inside the membrane were below the critical strain rate for DNA degradation. This is supported by the densitometry analysis of the agarose gels which suggests no degradation is detected during the entire course of filtration.

6.1.2 ***Correlation between the fouling mechanisms predicted by blocking models and direct observation using scanning electron microscopy.***

Based on flux decline data of the filtration of pGEc47 (56 kb) plasmid DNA, the fitting of experimental data with the blocking models indicated that the intermediate-standard model best described the fouling mechanism of the plasmid. Based on analysis of the transition of fouling mechanism; using power law analysis of d^2t/dV^2 vs. dt/dV, the intermediate blocking model dominated the fouling at early time of filtration. The fouling mechanism was then transformed to the standard blocking mechanism at higher values of dt/dV (later time of filtration).

The image analysis of the membrane after filtration of 50 µg pGEc47 supercoiled plasmid DNA indicated the existence of DNA meshes on the surface of the membrane. Molecular orientation of plasmid molecules with respect to fluid streamline and the molecule-molecule interactions before the plasmids approached the surface of the membrane is suspected to be the primary contribution to retention of plasmids. The blockage of plasmids on the surface of the membrane

is identical with the intermediate blocking mechanism which described that the blockage of the surface of membrane is caused by superposition of molecules.

The intermediate-standard blocking model also successfully predicted the domination of pore constriction mechanism with the increase of process fluid. The prediction provided by the model is in agreement with the observation by SEM that the accumulation and retention of plasmids occurred inside the membrane.

6.1.3 ***Limitation of the CFD simulations of macro- and micro-scale modelling***

6.1.3.1 Prediction using the Brinkman equation - The macro-scale model

A very sizeable contribution to the elongation forces experienced by the particles can also be associated with the entry of a plasmid molecule into the pore. By assuming the pressure distribution is uniform in fully-developed pipe flows, the entry length can be estimated; L_e /D = 0.06.Re. With the velocities on the order of 1 mm/s and D = 200 nm = $2x10^{-4}$ mm. Together with kinematic viscosity of water 1 mm^2/s this gives Re $\approx 2x10^{-4}$, so $L_e/D = 1.2x10^{-6}$, i.e. the flow adjusts itself to fully developed conditions at a distance that corresponds to a negligibly small fraction of the pore diameter after entry into the pore. Since the 20 kb SC plasmid is a very large molecule with the estimated supercoiled length; ~ $2x10^4$ kb x 0.34 nm x 0.4= 2.72 μm (number of base pair x axial rise between base pairs x 40 %- the supercoiled length is assumed to be 40 % of vector contour length)(Strick et al., 1998), the different parts of a molecule might expand along the length of pores if it is stretched near to its maximum .

The other consequence of the elongation effect during the entry flow is it tends to align particles to be more parallel to the flow when they enter the pore. This calls into question the assumption of randomly distributed initial orientation angles made in subsection 5.2.2. Due to the entry flow effect, angles near $\theta = 0$ during the trajectory of the rod-shape particle will be more probable than angles close to $\theta = 90^o$. Without more detailed consideration of the entry of the particle into the pore, the value of the factor $F_\theta = 0.525$ is likely to have been overestimated due to the earlier assumptions.

Therefore, the entry phenomenon cannot be ignored completely because plasmid molecules might experience an elongation process when it passes through such an entry. However, for the present purpose of estimating the elongational strain rates that are associated with shear in the Hagen-Poiseuille flow the entry effect can be ignored.

In analysing the trajectory of the particles into the pore, the orientation angle effects have only been analysed for particles that are oriented in a radial plane. The analyses of the second orientation angle to define out-of-plane orientations need to be estimated and considered in future work.

The above estimate of elongational strain rate applies to the trajectory of particles without perturbation of flow. In this work, this is neglected to simplify the analysis. The development of theory that involves a perturbation tensor associated with the presence of the particle is also interesting to be considered in the future.

6.1.3.2 Prediction using the 'image to simulation' workflow- The micro-scale model

The method described in subsection 5.2.3 does not consider the fouling of the membrane. The simulation is based on the geometry of an intact membrane. It is challenging to process and analyse a fouled membrane due to damage of the sample during the TEM's sample preparation. The usage of ethanol during the dehydration process is thought to have an impact on the DNA that is retained on and inside the membrane. As a consequence, it provides the images that do not represent the actual trend of fouling. The improvement of the TEM protocol in processing fouled membranes will contribute to the possibility of characterisation of fluid flow throughout the progression of fouling.

Beside the usage of TEM to generate image for the simulation, the application of x-ray tomography such as μ-CT (micro-tomography) or nano-CT (nano-tomography) was also considered. The advantage of this technique is that it can provide a 3D image of membranes using a non-invasive protocol: by scanning the sample under normal conditions without chemical and physical pre-treatments such as coating and vacuum treatment. The image is then reconstructed by volume rendering and image segmentation analysis. By using the 3D image, accurate determination of fluid flow inside the membrane can be determined using finite element analysis. Currently, this technique has limitations since the resolution of images is still insufficient for characterisation of membrane structure (it only has resolution limit down to 150-200 nm). The future development of the x-ray tomography that potentially provides adequate image resolution will make it an important tool for characterisation of fluid flow and fouling during filtration.

6.2 **Recommendations for future research**

6.2.1 ***Impact of pore structure design on the trajectory of plasmids***

The morphology and structure of the microfiltration membrane can have a significant impact on membrane capacity by influencing the rate and extent of fouling. For example, Zydney and Ho (2003) showed that the interconnected pore structure significantly increases the membrane capacity. (Zydney and Ho, 2003). The understanding of the dynamics of plasmid DNA during filtration can give insight into improved design of the membrane pore structure.

The dynamics of DNA in a defined flow has been studied using direct observation (Larson et al., 2006, Perkins et al., 1994, Perkins et al., 1995) and Brownian dynamic simulation (Reese and Zimm, 1990, Larson et al., 1999). The simulation of the protein trajectory during entrance into the membrane's pore was developed by Kim and Zydney (2004, 2005 and 2006).

However, the dynamics of the DNA polymer inside a polymeric membrane is still not well understood. This is due to the complexity of the interconnected pore structure and the design of an appropriate model of the plasmid's geometry.

In this work, a preliminary study of particle trajectory through a defined pore geometry has been developed. However, the simulation of the plasmid trajectory confronts the 'inverted mesh' problem. The description of the simulation can be found in Appendix 3.

6.2.2 ***Improved method to acquire internal structure of membrane***

To better represent the geometry of the filter, the development of the 3D image of the membrane using TEM technique was presented (Sub chapter 5.4.3). However, using this method, the approximation is based on the depth of the layer of membrane which is prepared using TEM technique. The image of the internal structure of the membrane can be improved significantly by using novel microscopy techniques such nano- and macro-computed tomography (nano- or micro-CT). Better representation of the image in 3D provides more accurate CFD simulation.

Furthermore, the possibility to capture the degree of fouling using a non-invasive method can be done through the application of advanced microscopy techniques such as nano/micro-CT. This technique has been tried but due to low resolution of the image, it is unsuitable to be a template

geometry for CFD simulation. Future development, in terms of the increase of image resolution can contribute to better characterisation of fouling during filtration. Development of better image processing software and image reconstruction algorithm can also help to characterise the microporous pore structure of the membrane.

By modelling fluid flow regimes during the progression of fouling, the characterisation of strain rates that are critical to the damage of plasmid DNA can be determined.

6.2.3 ***Estimation of membrane area requirement for larger scale plasmid DNA filtration***

In the development of downstream processing of a biotechnology product, the 47-mm disc filter is always applied in small scale studies to determine larger scale filter area requirement. However, the method of the prediction of larger scale membrane area requirement is still debated by scientists and engineers. A report by the Parenteral Drug Association suggests that the application of a small scale device test may not be accurate to predict the larger scale filterability of a membrane ((PDA), 1998).

An appropriate membrane blocking model can be used to determine the V_{max} of a membrane (Chapter 4). The blocking model that fits with the flux decline data of a specific filtration process can be used as basis to estimate the area requirement of larger scale filtration.

The automated multiwell technique (Kong et al., 2010) can be a potential device to be used as small scale process tool for scaling up the plasmid DNA filtration. The application of this approach may also reduce the consumption of valuable process fluid which is very critical in the development of a filtration process. By applying the membrane blocking model as described in chapter 4, the area requirement of larger-scale filter (such as pleated device) can be estimated with an appropriate safety factor.

6.2.4 ***Real time approach to direct visualisation of the progress of fouling***

The development of direct visualisation method to investigate the stretching of a plasmid has been developed (Perkins et al., 1994,1997, Smith et al., 1999). The fluorescent labelling of DNA can be used as tool to visualise the dynamics of this molecule under fluorescence microscope. This technique can be applied to investigate the fundamental mechanism of plasmid DNA fouling during a filtration process. However, specialised filter housing should be fabricated; such as a transparent small scale filter housing device, in order to directly visualise the fouling in real time.

References

(PDA), P. D. A. 1998. Sterilizing filtration of liquids. *J. Pharm. Sci. Technol.,* Suppl. 52 ,S1 (Technical Report No. 26).

ADAM, R. E. & ZIMM, B. H. 1977. Shear degradation of DNA. *Nucl. Acids Res.,* 4**,** 1513-1538.

ARULMUTHU, E., DAVID, J. W., HELEN, B., HENK, K. V. & MIKE, H. 2007. Studies on aerosol delivery of plasmid DNA using a mesh nebulizer. *Biotechnology and Bioengineering,* 98**,** 939-955.

ATKINS, E. D. T. & TAYLOR, M. A. 1992. Elongational flow studies on DNA in aqueous solution and stress-induced scission of the double helix. *Biopolymers,* 32**,** 911-923.

BAKHSHAYESHI, M., JACKSON, N., KURIYEL, R., MEHTA, A., VAN REIS, R. & ZYDNEY, A. L. 2011. Use of confocal scanning laser microscopy to study virus retention during virus filtration. *Journal of Membrane Science,* 379**,** 260-267.

BELFORT, G., DAVIS, R. H. & ZYDNEY, A. L. 1994. The behavior of suspensions and macromolecular solutions in crossflow microfiltration. *Journal of Membrane Science,* 96**,** 1-58.

BENOIT, H. & DOTY, P. 1953. Light Scattering from Non-Gaussian Chains. *The Journal of Physical Chemistry,* 57**,** 958-963.

BENSIMON, D., SIMON, A. J., CROQUETTE, V. & BENSIMON, A. 1995. Stretching DNA with a Receding Meniscus: Experiments and Models. *Physical Review Letters,* 74**,** 4754.

BOLTON, G., LACASSE, D. & KURIYEL, R. 2006. Combined models of membrane fouling: Development and application to microfiltration and ultrafiltration of biological fluids. *Journal of Membrane Science,* 277**,** 75-84.

BONDY, C. M. & SANTEUFEMIO, C. 2010. Analysis of fouling within microporous membranes in biopharmaceutical applications using latex microsphere suspensions. *Journal of Membrane Science,* 349**,** 12-24.

BOWEN, W. R., CALVO, J. I. & HERNÁNDEZ, A. 1995. Steps of membrane blocking in flux decline during protein microfiltration. *Journal of Membrane Science,* 101**,** 153-165.

BOWEN, W. R. & GAN, Q. 1991. Properties of microfiltration membranes: Flux loss during constant pressure permeation of bovine serum albumin. *Biotechnology and Bioengineering,* 38**,** 688-696.

BOWEN, W. R. & JENNER, F. 1995. Theoretical descriptions of membrane filtration of colloids and fine particles: An assessment and review. *Advances in Colloid and Interface Science,* 56**,** 141-200.

BOYCHYN, M., YIM, S. S. S., BULMER, M., MORE, J., BRACEWELL, D. G. & HOARE, M. 2004. Performance prediction of industrial centrifuges using scale-down models. *Bioprocess and Biosystems Engineering,* 26**,** 385-391.

BUSTAMANTE, C., SMITH, S. B., LIPHARDT, J. & SMITH, D. 2000. Single-molecule studies of DNA mechanics. *Current Opinion in Structural Biology,* 10**,** 279-285.

CARNES, A. E. & WILLIAMS, J. A. 2007. Plasmid DNA Manufacturing Technology. *Recent Patents on Biotechnology,* 1**,** 151-166.

DAVISON, P. F. 1959. The effect of hydrodynamic shear on the deoxyribonucleic acids from T2 and T4 bacteriophages. *Proceedings of the National Academy of Sciences of the United States of America,* 45**,** 1560-1568.

DE GENNES, P. 1974. Coil-stretch transition of dilute flexible polymers under ultrahigh velocity

gradients. *The Journal of Chemical Physics,* 60**,** 5030-5042.

DUCLOS-ORSELLO, C., LI, W. & HO, C.-C. 2006a. A three mechanism model to describe fouling of microfiltration membranes. *Journal of Membrane Science,* 280**,** 856-866.

DUCLOS-ORSELLO, C., LI, W. & HO, C.-C. 2006b. A three mechanism model to describe fouling of microfiltration membranes. *Journal of Membrane Science,* 280**,** 856-866.

FERRANDO, M., RŐŻEK, A., ZATOR, M., LÓPEZ, F. & GÜELL, C. 2005. An approach to membrane fouling characterization by confocal scanning laser microscopy. *Journal of Membrane Science,* 250**,** 283-293.

FISHMAN, D. M. & PATTERSON, G. D. 1996. Light scattering studies of supercoiled and nicked DNA. *Biopolymers,* 38**,** 535-552.

FUJII, M. & YAMAKAWA, H. 1975. Moments and Transport Coefficients of Wormlike Rings. *Macromolecules,* 8**,** 792-799.

HABER, C., SKUPSKY, J., LEE, A. & LANDER, R. 2004. Membrane chromatography of DNA: Conformation-induced capacity and selectivity. *Biotechnology and Bioengineering,* 88**,** 26-34.

HERMIA, J. 1982. Constant pressure blocking filtration laws-application to power law non-Newtonian fluids. *Chemical Engineering Research and Design,* 60a**,** 183-187.

HIRASAKI, T., SATO, T., TSUBOI, T., NAKANO, H., NODA, T., KONO, A., YAMAGUCHI, K., IMADA, K., YAMAMOTO, N., MURAKAMI, H. & MANABE, S.-I. 1995. Permeation

mechanism of DNA molecules in solution through cuprammonium regenerated cellulose hollow fiber (BMMtm). *Journal of Membrane Science,* 106**,** 123-129.

HLAVACEK, M. & BOUCHET, F. 1993. Constant flowrate blocking laws and an example of their application to dead-end microfiltration of protein solutions. *Journal of Membrane Science,* 82**,** 285-295.

HO, C.-C. & ZYDNEY, A. L. 2000. A Combined Pore Blockage and Cake Filtration Model for Protein Fouling during Microfiltration. *Journal of Colloid and Interface Science,* 232**,** 389-399.

IRITANI, E., MUKAI, Y., TANAKA, Y. & MURASE, T. 1995. Flux decline behavior in dead-end microfiltration of protein solutions. *Journal of Membrane Science,* 103**,** 181-191.

KELLY, S. T., SENYO OPONG, W. & ZYDNEY, A. L. 1993. The influence of protein aggregates on the fouling of microfiltration membranes during stirred cell filtration. *Journal of Membrane Science,* 80**,** 175-187.

KIM, M.-M. & ZYDNEY, A. L. 2004. Effect of electrostatic, hydrodynamic, and Brownian forces on particle trajectories and sieving in normal flow filtration. *Journal of Colloid and Interface Science,* 269**,** 425-431.

KIM, M.-M. & ZYDNEY, A. L. 2005. Particle-particle interactions during normal flow filtration: Model simulations. *Chemical Engineering Science,* 60**,** 4073-4082.

KIM, M.-M. & ZYDNEY, A. L. 2006. Theoretical analysis of particle trajectories and sieving in a two-dimensional cross-flow filtration system. *Journal of Membrane Science,* 281**,** 666-675.

KONG, S., AUCAMP, J. & TITCHENER-HOOKER, N. J. 2010. Studies on membrane sterile filtration of plasmid DNA using an automated multiwell technique. *Journal of Membrane Science,* 353**,** 144-150.

KONG, S., TITCHENER-HOOKER, N. & LEVY, M. S. 2006. Plasmid DNA processing for gene therapy and vaccination: Studies on the membrane sterilisation filtration step. *Journal of Membrane Science,* 280**,** 824-831.

LARSON, J. W., YANTZ, G. R., ZHONG, Q. & GILMANSHIN, R. 2006. Single DNA molecule stretching in sudden mixed shear and elongational microflows. *Lab on Chip,* 6**,** 1187.

LARSON, R. G., HUA, H., SMITH, D. E. & CHU, S. 1999. Brownian dynamics simulations of a DNA molecule in an extensional flow field. *Journal of Rheology,* 43**,** 267-304.

LASKA, M. E., BROOKS, R. P., GAYTON, M. & PUJAR, N. S. 2005. Robust scale-up of dead end filtration: Impact of filter fouling mechanisms and flow distribution. *Biotechnology and Bioengineering,* 92**,** 308-320.

LATULIPPE, D. R., MOLEK, J. R. & ZYDNEY, A. L. 2008. Importance of Biopolymer Molecular Flexibility in Ultrafiltration Processes. *Industrial & Engineering Chemistry Research,* 48**,** 2395-2403.

LATULIPPE, D. R. & ZYDNEY, A. L. 2010. Radius of gyration of plasmid DNA isoforms from static light scattering. *Biotechnology and Bioengineering,* 107**,** 134-142.

LAVERY, R., LEBRUN, A., ALLEMAND, J.-F., BENSIMON, D. & CROQUETTE, V. 2002. Structure and mechanics of single biomolecules: experiment and simulation. *Journal of Physics: Condensed Matter,* 14**,** R383.

LEBRUN, A. & LAVERY, R. 1996. Modelling Extreme Stretching of DNA. *Nucleic Acids Research,* 24**,** 2260-2267.

LENGSFELD, C. S. & ANCHORDOQUY, T. J. 2002. Shear-induced degradation of plasmid DNA. *Journal of Pharmaceutical Sciences,* 91**,** 1581-1589.

LEVINTHAL, C. & DAVISON, P. F. 1961. Degradation of deoxyribonucleic acid under hydrodynamic shearing forces. *Journal of Molecular Biology,* 3**,** 674-683.

LEVY, M. S., CICCOLINI, L. A. S., YIM, S. S. S., TSAI, J. T., TITCHENER-HOOKER, N., AYAZI SHAMLOU, P. & DUNNILL, P. 1999a. The effects of material properties and fluid flow intensity on plasmid DNA recovery during cell lysis. *Chemical Engineering Science,* 54**,** 3171-3178.

LEVY, M. S., COLLINS, I. J., YIM, S. S., WARD, J. M., TITCHENER-HOOKER, N., AYAZI SHAMLOU, P. & DUNNILL, P. 1999b. Effect of shear on plasmid DNA in solution. *Bioprocess and Biosystems Engineering,* 20**,** 7-13.

LEVY, M. S., O'KENNEDY, R. D., AYAZI-SHAMLOU, P. & DUNNILL, P. 2000. Biochemical engineering approaches to the challenges of producing pure plasmid DNA. *Trends in Biotechnology,* 18**,** 296-305.

LIU, M. A. 2011. DNA vaccines: an historical perspective and view to the future. *Immunological Reviews,* 239**,** 62-84.

MEACLE, F. J., ZHANG, H., PAPANTONIOU, I., WARD, J. M., TITCHENER-HOOKER, N. J. & HOARE, M. 2007. Degradation of supercoiled plasmid DNA within a capillary device. *Biotechnology and Bioengineering,* 97**,** 1148-1157.

MILLER, J., ROGOWSKI, M. & KELLY, W. 2002. Using a CFD Model To Understand the Fluid Dynamics Promoting E. coli Breakage in a High-Pressure Homogenizer. *Biotechnology Progress,* 18**,** 1060-1067.

NOY, A., VEZENOV, D. V., KAYYEM, J. F., MAADE, T. J. & LIEBER, C. M. 1997. Stretching and breaking duplex DNA by chemical force microscopy. *Chemistry & Biology,* 4**,** 519-527.

PERKINS, T. T., SMITH, D. E. & CHU, S. 1994. Direct Observation of Tube-Like Motion of a Single Polymer Chain. *Science,* 264**,** 819-822.

PERKINS, T. T., SMITH, D. E. & CHU, S. 1997. Single Polymer Dynamics in an Elongational Flow. *Science,* 276**,** 2016-2021.

PERKINS, T. T., SMITH, D. E., LARSON, R. G. & CHU, S. 1995. Stretching of a Single Tethered Polymer in a Uniform Flow. *Science,* 268**,** 83-87.

PRATHER, K. J., SAGAR, S., MURPHY, J. & CHARTRAIN, M. 2003. Industrial scale production of plasmid DNA for vaccine and gene therapy: plasmid design, production, and purification. *Enzyme and Microbial Technology,* 33**,** 865-883.

PRAZERES, D. M. F. & FERREIRA, G. N. M. 2004. Design of flowsheets for the recovery and purification of plasmids for gene therapy and DNA vaccination. *Chemical Engineering and Processing: Process Intensification,* 43**,** 609-624.

RAJNIAK, P., TSINONTIDES, S. C., PHAM, D., HUNKE, W. A., REYNOLDS, S. D. & CHERN, R. T. 2008. Sterilizing filtration--Principles and practice for successful scale-up to manufacturing. *Journal of Membrane Science,* 325**,** 223-237.

REESE, H. R. & ZIMM, B. H. 1990. Fracture of polymer chains in extensional flow: Experiments with DNA, and a molecular-dynamics simulation. *The Journal of Chemical Physics,* 92**,** 2650-2662.

RYSKIN, G. 1987. Calculation of the effect of polymer additive in a converging flow. *Journal of Fluid Mechanics Digital Archive,* 178**,** 423-440.

SCHLEEF, M. & SCHMIDT, T. 2004. Animal-free production of ccc-supercoiled plasmids for research and clinical applications. *The Journal of Gene Medicine,* 6**,** S45-S53.

SHAMLOU, P. A. 2003. Scaleable processes for the manufacture of therapeutic quantities of plasmid DNA. *Biotechnology and Applied Biochemistry,* 37**,** 207-218.

SMITH, D. E., BABCOCK, H. P. & CHU, S. 1999. Single-Polymer Dynamics in Steady Shear Flow. *Science,* 283**,** 1724-1727.

STRICK, T. R., ALLEMAND, J. F., BENSIMON, D. & CROQUETTE, V. 1998. Behavior of Supercoiled DNA. 74**,** 2016-2028.

TITCHENER-HOOKER, N. J., DUNNILL, P. & HOARE, M. 2008. Micro biochemical engineering to accelerate the design of industrial-scale downstream processes for biopharmaceutical proteins. *Biotechnology and Bioengineering,* 100**,** 473-487.

TRACEY, E. M. & DAVIS, R. H. 1994. Protein Fouling of Track-Etched Polycarbonate Microfiltration Membranes. *Journal of Colloid and Interface Science,* 167**,** 104-116.

USFDA 2007. Guidence for Industry; Considerations for Plasmid DNA Vaccines for Infectious Desease Indications. *In:* US FOOD AND DRUG ADMINISTRATION, R., MD, USA (ed.).

VAN REIS, R. & ZYDNEY, A. 2001. Membrane separations in biotechnology. *Current Opinion in Biotechnology,* 12**,** 208-211.

WATSON, M. P., WINTERS, M. A., SAGAR, S. L. & KONZ, J. O. 2006. Sterilizing filtration of plasmid DNA: Effects of plasmid concentration, molecular weight, and conformation. *Biotechnology Progress,* 22**,** 465-470.

WUBBOLTS, M. G., FAVRE-BULLE, O. & WITHOLT, B. 1996. Biosynthesis of synthons in two-liquid-phase media. *Biotechnology and Bioengineering,* 52**,** 301-308.

WYART, Y., GEORGES, G., DEUMIÉ, C., AMRA, C. & MOULIN, P. 2008. Membrane characterization by microscopic methods: Multiscale structure. *Journal of Membrane Science,* 315**,** 82-92.

ZEMAN, L. & DENAULT, L. 1992. Characterization of microfiltration membranes by image analysis of electron micrographs.: Part I. Method development. *Journal of Membrane Science,* 71**,** 221-231.

ZIEL, R., HAUS, A. & TULKE, A. 2008. Quantification of the pore size distribution (porosity profiles) in microfiltration membranes by SEM, TEM and computer image analysis. *Journal of Membrane Science,* 323**,** 241-246.

ZYDNEY, A. L. & HO, C.-C. 2002. Scale-up of microfiltration systems: fouling phenomena and Vmax analysis. *Desalination,* 146**,** 75-81.

ZYDNEY, A. L. & HO, C.-C. 2003. Effect of membrane morphology on system capacity during normal flow microfiltration. *Biotechnology and Bioengineering,* 83**,** 537-543.

Appendices

6.1 **Appendix 1**

Trace element	g/mol
FeSO4.7H2O	245.8
MnSO4.H2O	137
Al2(SO4)3.16H2O	264
CoCl2.6H2O	238
MoO4Na2(H2O)	224
CuCl2.2H2O	170.5
ZnSO4.7H2O	255.4
H3BO4	62

Appendix 1.2- Trace elements used in the fermentation of E.coli DH1

6.2 **Appendix 2**

The typical optical density profile of the *E.coli* fed-batch fermentation to produce plasmid DNA is shown below:

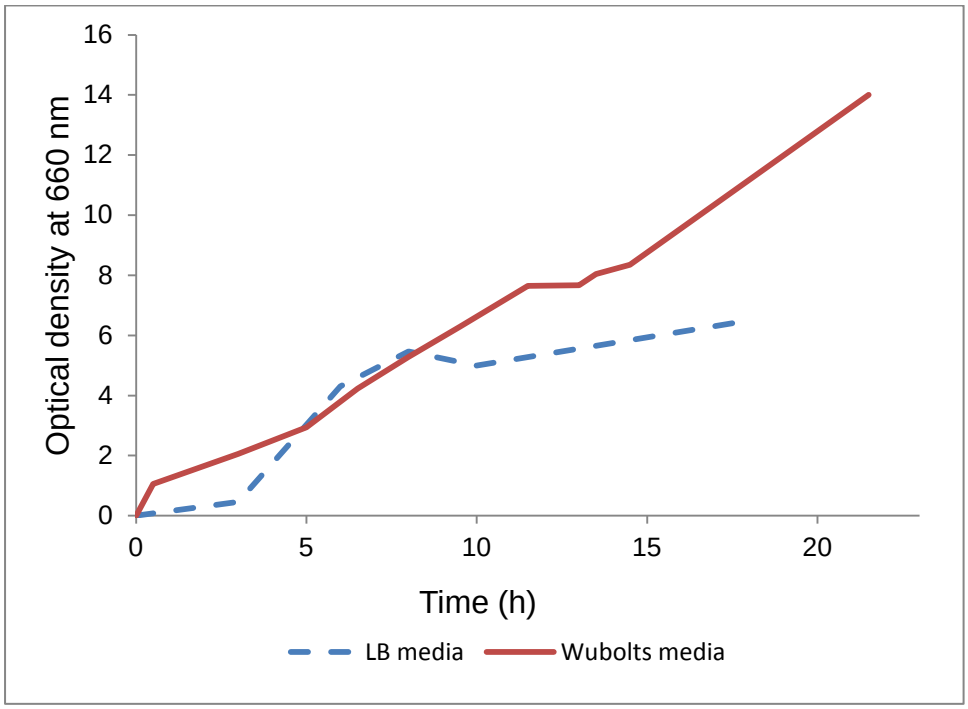

Appendix 1.1- The plot above shows the growth of E-coli DH1 (pGEc47 plasmid) using either LB or Wubbolts media during the fed-batch fermentation. The sample was taken at specific time and the optical density was obtained through spectrophotometry analysis at 660 nm.

6.3 **Appendix 3**

In this work, a preliminary model to investigate the trajectory of a particle into the pore has been developed. However, the simulation confronts the inverted mesh problem that contributes to the inaccuracy of the solution.

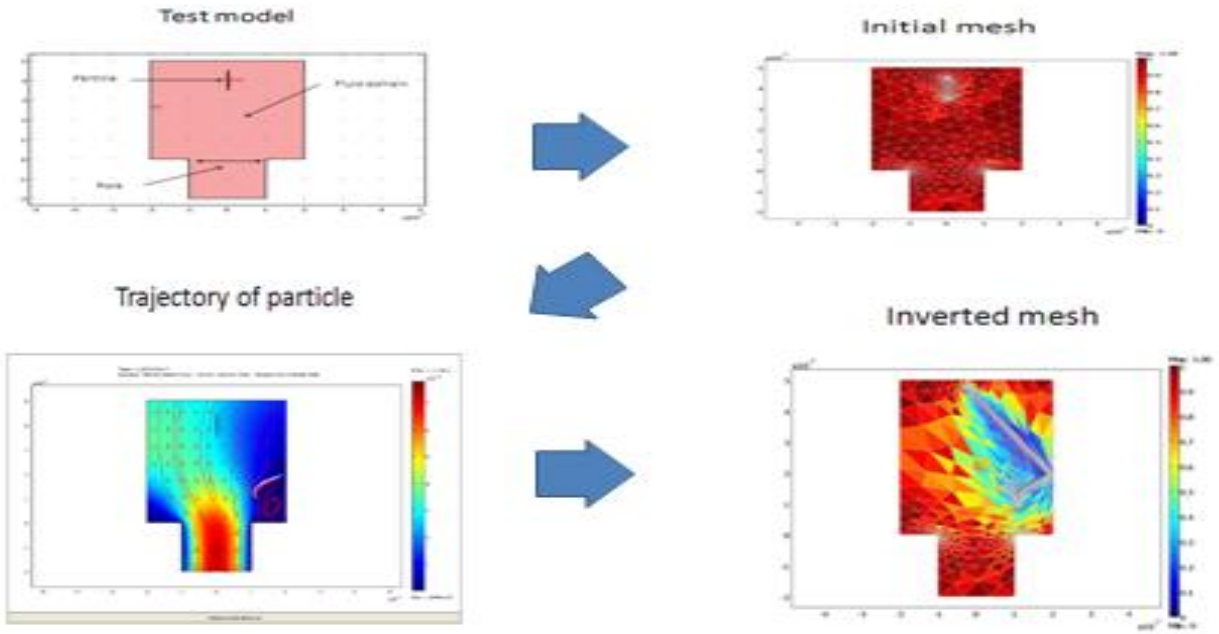

Appendix 1.3- The preliminary simulation of the trajectory of plasmid DNA into a defined pore structure